



LIETUVOS
ENERGETIKOS
INSTITUTAS



Vilnius University
Institute of
Theoretical Physics
and Astronomy

Annual Report of the Association EURATOM / LEI

2010

ISSN 2029-1612

© Lithuanian Energy Institute, 2011

Content

1	Introduction	4
2	Accident analysis and evaluation of consequences for W7-X	5
2.1	Detailed simulation of plasma vessel pressurization in case of LOCA using RELAP5 and COCOSYS codes	6
2.1.1	W7-X facility and model for RELAP5	6
2.1.2	Investigated accident scenario	8
2.1.3	Detailed analysis of processes in plasma vessel	10
2.1.4	Development of plasma vessel nodalisation using COCOSYS code	10
2.1.5	Results of the COCOSYS simulation	12
2.2	Integral analysis of LOCA using ASTEC code	13
2.2.1	Models of cooling system and plasma vessel for ASTEC code	13
2.2.2	Results of integral analysis	16
2.3	Structural analysis concerning Loss of Vacuum Accident. Assessment of critical port/plasma vessel connections	20
2.3.1	Geometrical and finite element models of the port welds	20
2.3.2	Material properties	23
2.3.3	Boundary condition of the model	24
2.3.4	Applied Loading for Structural Integrity Analysis	24
2.3.5	Analysis of stress in the welding between Plasma Vessel and ports with gap 1mm	25
3	Investigation of spectroscopic characteristics of highly charged ions of tungsten	39
3.1	Quasirelativistic treatment of spectral characteristics of W^{37+} , W^{36+} and W^{35+}	39
3.2	Calculation of fluorescence yields, Auger transition probabilities and natural level widths for the states of multiple ions of tungsten with vacancies in the 4l (l = 0-3) shells	45
3.3	Calculations of radiative transition spectra in the regions of 4-7 nm and 12-14 nm for W^{40+} – W^{45+}	46
3.4	Calculation of the electron-impact excitation rates among the levels of $4d^N$ configurations for tungsten ions	49
3.5	Theoretical studies of highly charged tungsten atoms having open f-shells taking into account relativistic and correlation effects	51
4	Mobility program 2010	57
5	Public information	59
6	Publications	60
7	Implementation of QA system	61
8	References	62

1 INTRODUCTION

Today, about 80% of all energy produced comes from the fossil fuel (oil, carbon, and natural gas). European scientists are developing environmentally friendly, safe, and renewable energy technologies. Nuclear fusion is one of them. Nuclear fusion reactors promise high power energy sources, which have low impact on environment, are safe and have virtually unlimited fuel resources. This technology is not limited to heat and electricity generation, it also could be used for hydrogen production, which would lead to further development of the “hydrogen economy”.

European nuclear fusion research program allows using common European research and their development resources in all important research areas. Co-operation is especially important not only in the operation of the Joint European Torus (JET), but also in the execution of the European Fusion Development Agreement (EFDA) technological program, which is devoted to the ITER project, and also encompasses promising DEMO research. European fusion research and development program, based on EURATOM contract, is being coordinated and carried out by the European Commission.

After negotiations took place in the year 2006, Lithuanian Energy Institute (LEI) signed a contract on joining the EFDA agreement. On 2006 November 15, the first meeting of this project with the participation of the European Commission and Lithuanian organizations took place. During this meeting, project execution rules were presented and work programs for the year 2007 were agreed. The signed contract came into force from 1st January 2007 and Lithuania has officially become an EFDA member.

Following signed contract the work program is composed every year and approved by the Steering Committee.

Currently, there are two Lithuanian organisations participating in the EFDA project – Lithuanian Energy Institute and Vilnius University Institute of Theoretical Physics and Astronomy. Information regarding works performed by both these institutions during the year 2010 is presented in this report.

2 ACCIDENT ANALYSIS AND EVALUATION OF CONSEQUENCES FOR W7-X

2.1 Detailed simulation of plasma vessel pressurization in case of LOCA using RELAP5 and COCOSYS codes

W7-X (Figure 2.1) is a stellarator type nuclear fusion experimental device, currently being built at the Max Planck Institute of Plasma Physics (Max-Planck-Institut für Plasmaphysik (IPP), in Greifswald, Germany. The purpose of this facility is to demonstrate that stellarator type devices can be used to sustain stable plasma conditions for half an hour and longer. Plasma diagnostics and control technologies would be tested in this facility. Protective plates and cooled components of first wall used inside the plasma torus are made from the same materials, which will be used for the ITER facility; therefore, W7-X will also contribute to the ITER development.

Co-operation between LEI and IPP started in the year 2007 and were continued during the year 2010. It was planned to update the developed models and perform detailed analysis of 40 mm diameter cooling water pipe rupture. In W7-X design a rupture of one 40 mm diameter pipe, providing water to the divertor target is the most severe accident in terms of vacuum vessel pressurization [1]. In order to avoid negative effects on device equipment absolute pressure inside the torus must not exceed 1.1 bar. To avoid the plasma vessel overpressure, active (safety valves on coolant pipes) and passive safety devices (burst or rupture disk) are used. The burst disk has to be opened at 1.1 bar pressure inside the torus and relief steam into the torus hall, i.e. room in which W7-X is situated. Steam can be released from the torus hall with the means of ventilation or through the safety valves. During one of the LEI and IPP meetings it was decided

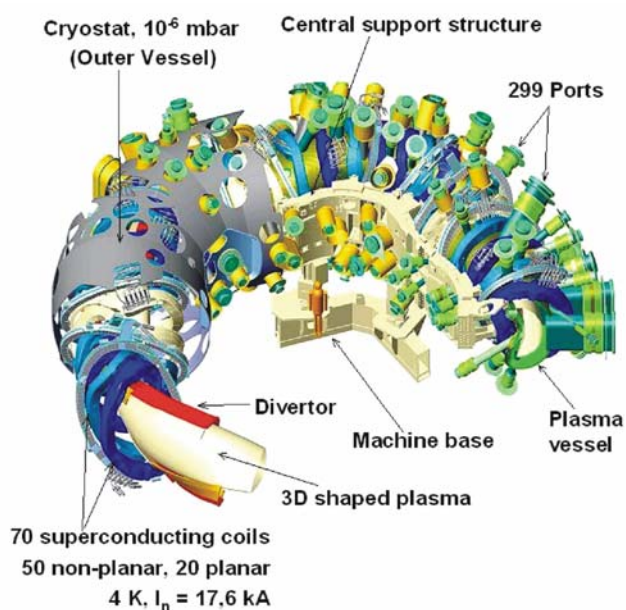


Figure 2.1
The fragment of a CAD model
of the W7-X system

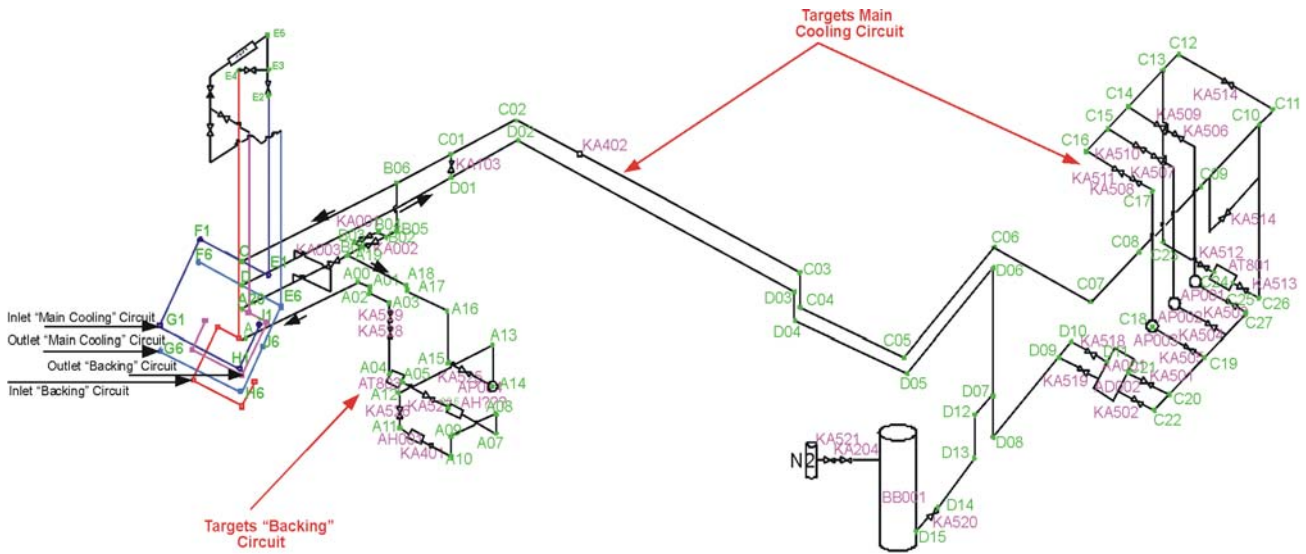


Figure 2.3
RELAP5 nodalisation scheme of the cooling and "baking" circuits

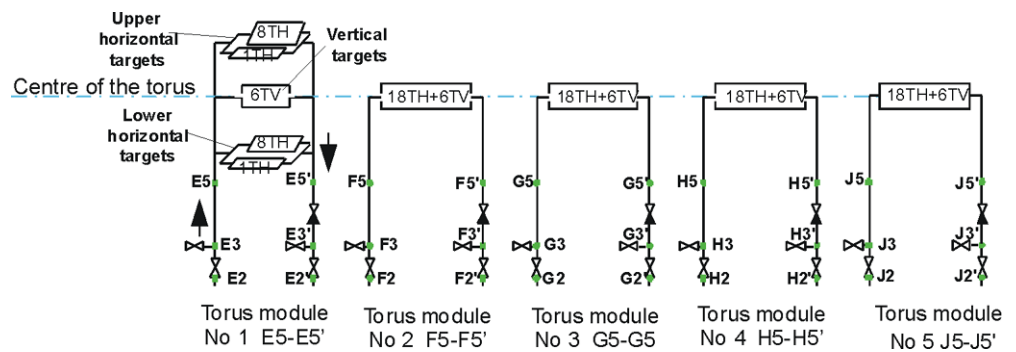


Figure 2.4
Modeling of the target modules (nodalization scheme)

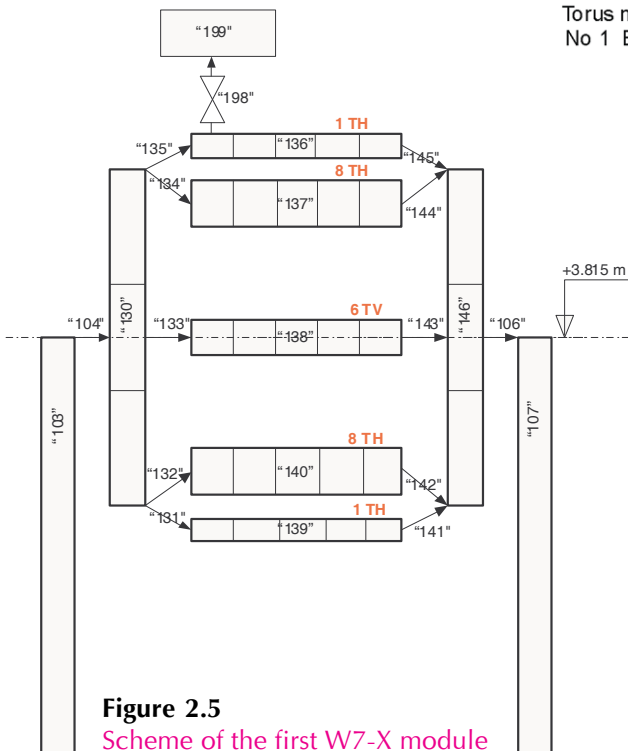


Figure 2.5
Scheme of the first W7-X module

In RELAP5 model the plasma vessel is modeled as horizontal cylinder (see Figure 2.6). In RELAP5 model for simulation of plasma vessel the pipe element "199" is used. The single junction "213" connects the open ends of cylinder, simulating closed circle of torus geometry. The plasma vessel volume is 108.375 m³. It was assumed that equivalent cylinder length is 34 m. According to plasma vessel volume the diameter of cylinder was calculated (2.016 m). In this cylinder the inner surface area is 215.337 m² and average wall thickness is 0.01915 m. The heat transfer between hot surfaces of plasma vessel is evaluated in developed RELAP5 model using model

of heat structures. It was assumed, that initial temperature of the plasma vessel structures (steel walls) is equal to 150 °C.

From the break (valve element “195” the steam-water mixture is discharged into small volume (element “196”) which simulate the inner volume of port and volume behind the target. This small volume (0.03 m²) is connected with main volume of plasma vessel using single junction “198”. The plasma vessel is connected to the Torus hall by pipe with burst disk. This disk is simulated using valve “217”, which is closed at the beginning and opens if pressure difference in plasma vessel and torus hall exceeds 10 kPa . Such safety measure is planned to implement in W7-X to prevent plasma vessel from overpressure. The torus hall is simulated in RELAP5 model using time dependent volume “218” with atmospheric pressure. When the W7-X device is working in the “baking” mode, pressure inside the vacuum vessel it is only 10 Pa – 1 kPa. Due to limitation of RELAP5 code it was assumed that the pressure in plasma vessel is equal to 1000 Pa.

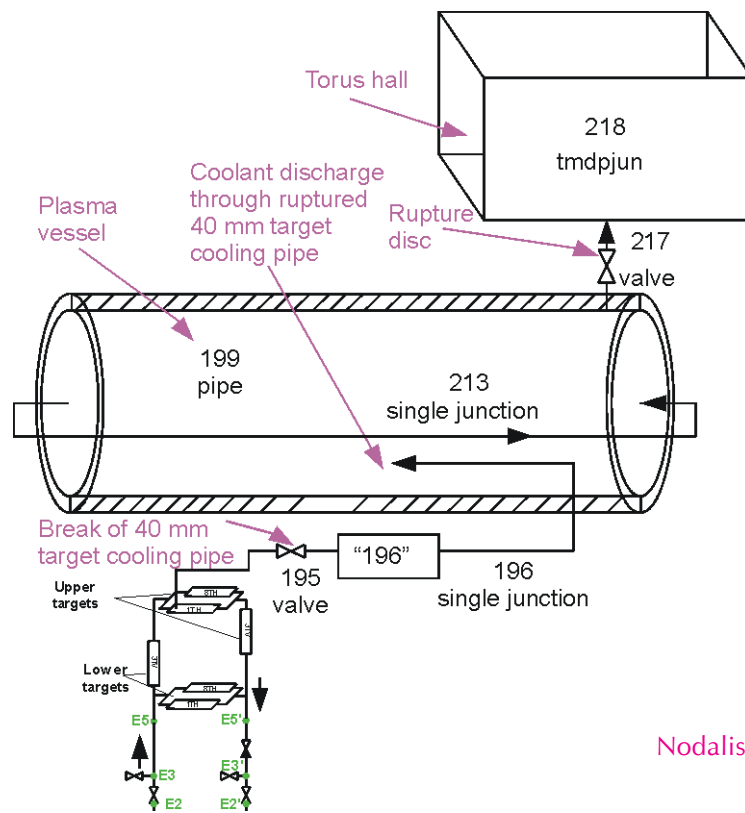


Figure 2.6.
Nodalisation scheme of plasma vessel

2.1.2 Investigated accident scenario

In the model it was assumed, that the break occurs in the torus module E5-E5' (see Figure 2.4). The break occurs in 40 mm diameter feeder pipe, connecting single upper horizontal target module (element “136” in Figure 2.5). The following assumptions are used:

- Double ended guillotine break occurs during the time 0.01 s.
- To reduce the discharge of water from rupture to plasma vessel the automatic valves on targets inlet automatic valves - E3, F3, G3, H3, I3 (Figure 2.4) are closing. Signal for automatic valves actuation is generated when pressure in plasma vessel reaches 2000 Pa. The calculations shows, that pressure reaches 2000 Pa in plasma vessel 0.14s after the break initiating.

- Delay between parameter reaches the set-point and signal generation – 0.5 s. Delay between signal generation and start of valve actuation – 1 s. Thus, 1.64 s after the break, the automatic valve in target module inlet starts to close.
- Full automatic valve on target module inlets closure time – 5 s. Thus, 6.64 s after the break time the target module inlet automatic valve are fully closed.
- Another measure to reduce the discharge of water from rupture to plasma vessel - automatic trip of pump in “baking” circuit. It was assumed, that signal for automatic pump trip is same as for automatic valve trip – when pressure in plasma vessel reaches 2000 Pa (0.14 s). Delay between parameter reaches the set-point and pump trip – 1 s. So trip of pump in “baking” circuit begins 1.14s after the break.

The discharge of coolant through the break is presented in Figure 2.7. As it is presented in the figure, the water flow in the “baking” circuit stops after the closure of automatic valves. After close of the inlet automatic valve the discharge of coolant through the break slightly decreases, but the water from other target modules in this torus module is discharged till pressure in this module decreases down to the pressure in plasma vessel. The pump trip begins about 1.14s after the break, thus leads to pressure decrease in pump outlet (see Figure 2.8). After closure of target module inlets automatic valves, the pressure in “baking” circuit starts to increase (in Figure 2.8 the time moment is marked when the valve is fully closed). This is because inertia of pump impeller – after the pump trip the impeller is still rotating for about 1.5 minutes. The water is supplied into pipelines that cause the pressure increase in system upstream the valve. After the automatic valves in target module inlets are closed, the pressure in pump header is decreasing

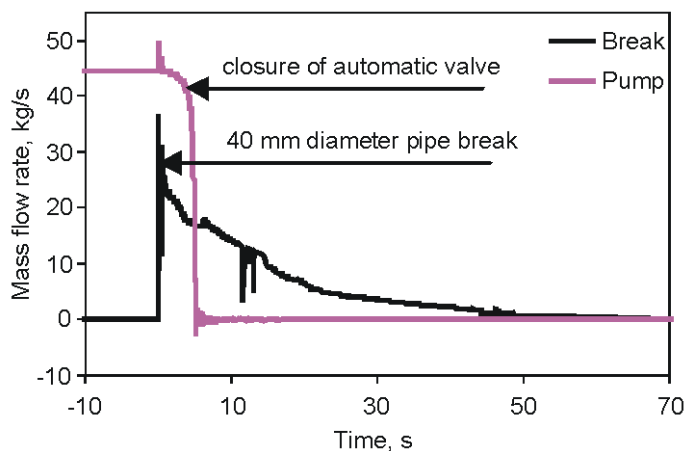


Figure 2.7
Break of upper target module. Water flow rate through the pump and discharge of coolant through the break

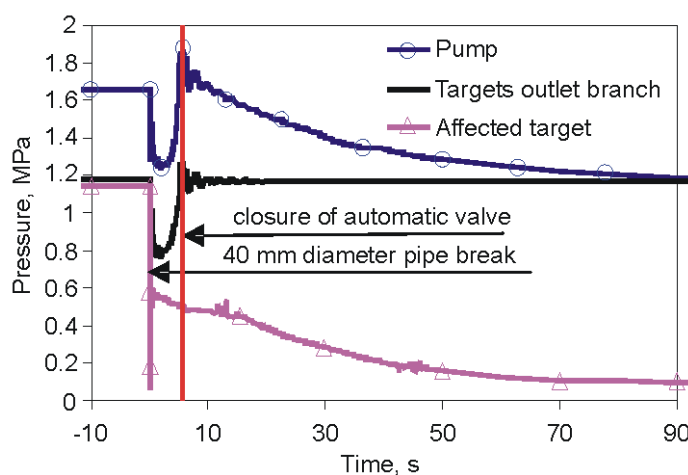


Figure 2.8
Break of upper target module. Pressure in “baking” circuit

slowly. Because the inlet automatic valves are closed, the water is discharged only from the affected torus module. The pressure remains nominal in other modules (see Figure 2.8), because automatic valves isolated them. The discharge of water through the break into plasma vessel leads to the loss of vacuum condition and overpressure in the plasma vessel. As it is presented in Figure 2.9, the pressure in small volume at break area (inner volume of port and volume behind the target) is increasing very sharply just after the break. This is due to small volume and significant resistance for steam-water flow in connection to main volume of plasma vessel. The pressure in plasma vessel is increasing slower. 44 seconds after occurrence of break the pressure in plasma vessel reaches 1100 kPa (absolute pressure). At this moment the burst disk, connecting the plasma vessel with torus hall is opening and pressure inside plasma vessel starts to decrease. After few seconds the pressure in vessel equalizes to atmospheric pressure, which is in the torus hall (Figure 2.9).

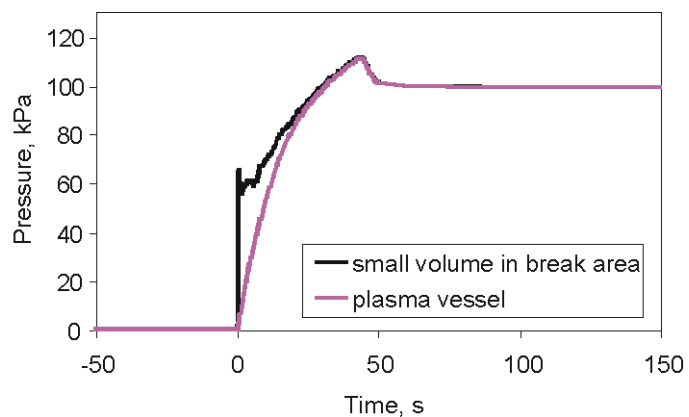


Figure 2.9
Break of upper target module.
Pressure in “baking” circuit

2.1.3 Detailed analysis of processes in plasma vessel

The RELAP5 code is designed for the analysis of processes in heat removal systems filled with water or steam. The modeling of processes in reactor cooling systems using RELAP5 is quite well validated, but for analysis of processes in compartments another specialized computer codes are used. Thus, for more detailed simulation of processes in plasma vessel (water evaporation due to pressure drop between ~ 1 MPa in “baking” circuit and vacuum in plasma vessel, displacement of air, water collection in the bottom part of vessel, heat transfer between water-steam mixture and metal structures of vessel) the code COCOSYS was used.

2.1.4 Development of plasma vessel nodalisation using COCOSYS code

The simulation of the evolution of the thermodynamic parameters in the vacuum vessel of the W7-X stellarator was performed with the lumped-parameter code COCOSYS [4]. COCOSYS is a German containment code system developed by GRS. COCOSYS code is based on mostly mechanistic models and intended for comprehensive simulation of all relevant processes and plant states during severe accidents in the containment of light water reactors. In order to perform accident simulations, nodalisation scheme of the vacuum vessel was developed.

Complicated three-dimensional geometry of the stellarator in the developed model is simplified to the geometry of horizontal cylinder. Ends of the cylinder are open and joined together, simulating closed circle of torus geometry. Whole volume of the vacuum vessel, and surface area and mass of vessels structures in the model correspond to the available design data. Device is composed out of five parts with similar configurations, called modules. Each module of the

vacuum vessel is subdivided into nine virtual control nodes (zones) in the scheme (Figure 2.10): four in the central part of the scheme cross-section (nodes C**), four in the outer part (nodes O**) and one in the bottom part (node BOT), in which released water is collected. Figure 2.10 shows cross-section of one module nodalisation scheme. All five modules are simulated in the analysis. Volumes of the zones are calculated from the geometry of the cylinder assuming volume and length of the cylinder equal to the free volume and circumference of the torus. All adjacent zones of one module are connected by atmospheric junctions. Areas of these junctions and their lengths are calculated from the cylinder geometry. Corresponding zones of the adjacent modules (e.g., CBL zones of the first and second modules) except BOT zones also are connected by atmospheric junctions, properties of which are calculated from the geometry of cylinder.

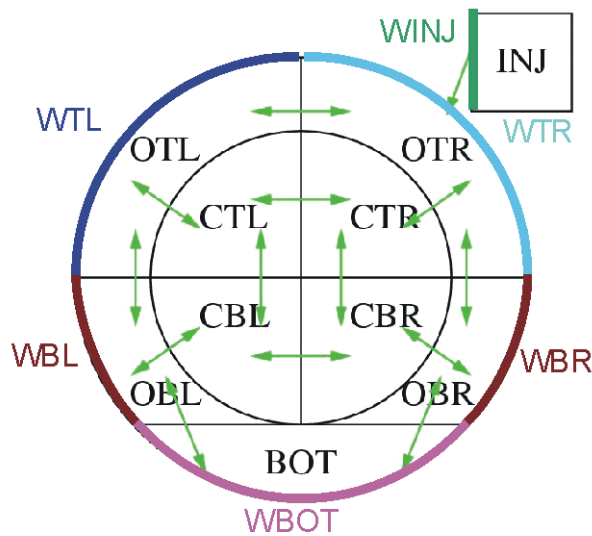


Figure 2.10
Cross-section of the developed nodalisation scheme of the vacuum vessel for one module (black – nodalisation nodes, green – atmospheric junctions, heat transfer structures – in different colors)

INJ zone is the zone into which the water release from the ruptured pipe is simulated. It is defined for the aims of simulation – it helps to more realistically model the water flowing from the ruptured pipe to the wall of the vacuum vessel. INJ zone is present only in one module. Geometric parameters of this zone were selected according to port data and the initial thermodynamic parameters are the same as in the whole vacuum vessel. Two zones not presented in the Figure 2.10 were also simulated – torus hall and environment. The former is a 16800 m³ volume hall in which stellarator torus is situated. Conditions in the hall were selected according to planned normal operation of W7-X device. OTL node of the vacuum vessel third module and torus hall node are separated by the simulated burst disk. The diameter of this burst disk is equal to 250 mm. It is possible in COCOSYS to simulate burst disk by defining an atmospheric junction, which is closed at the beginning and opens if pressure difference between the zones it connects reaches indicated value (direction considered). In the case of W7-X this value is equal to 10 kPa. Area of this junction was set equal to the area of the burst disk. The environment node was used to simulate hot environment of the outer side of the simulated vacuum vessel walls. This node has no connections with other nodes and is needed only for modeling purposes. The simulated heat transfer structures are presented in Figure 2.10 in different colors. Surface areas of the structures were calculated from the known mass and thickness of the structures, assuming steel density equal to 7900 kg/m³. Structures are assumed to be composed only of steel. WBOT wall is divided into two parts – vertical and horizontal. To simulate water flow along the vessel walls, three water flow junctions are defined in the first module (there is no water in other modules during the accident), connecting:

1. INJ node with the WTR wall,
2. OTR node with the WBR wall and
3. OBR node with the WBOT vertical wall.

2.1.5 Results of the COCOSYS simulation

The initial parameters, necessary for the COCOSYS simulation (mass flow of the coolant through the rupture and its specific enthalpy) was taken from RELAP5 calculations, presented in previous section. At the start of the accident coolant starts to flow out of the ruptured pipe into the containment (Figure 2.11). However, the flow is decreasing. Specific enthalpy of the flowing coolant is sharply increasing starting time moment $t = 60$ s, however, the mass flow rate at this time is small (<1 kg/s) and continuing to decrease (at time $t > 70$ s, the discharge of coolant into plasma vessel terminated), therefore this increase don't have influence on the results.

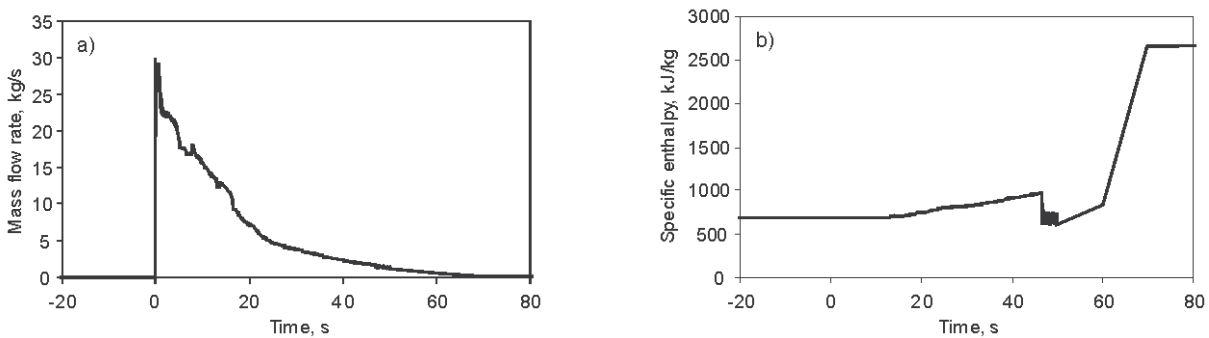


Figure 2.11
Evolutions of coolant mass flow rate through the rupture a) and its specific enthalpy b) used in the calculations

Calculations were performed using COCOSYS version V2.3v20 and the presented nodalisation scheme of the vacuum vessel (Figure 2.10). Results obtained from the calculations show that after pipe rupture takes place, pressure inside the vacuum vessel starts to rise and during 30 seconds reaches value of 110 kPa (Figure 2.12). Pressure differences inside the vacuum vessel are insignificant, because whole volume of the vacuum vessel is open for mass transfer and

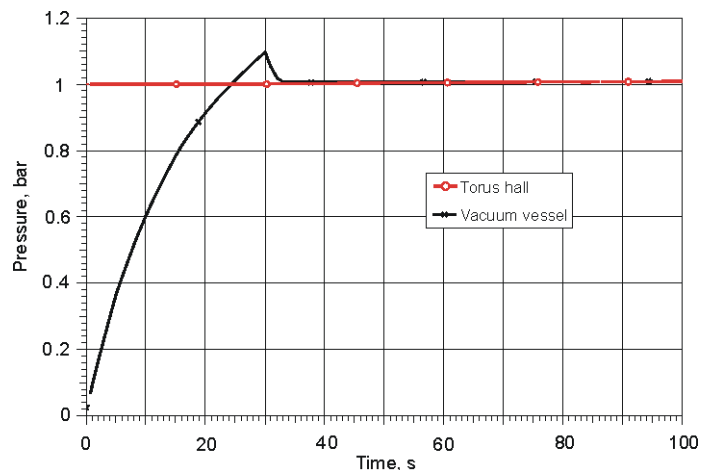


Figure 2.12
Obtained pressure evolutions inside the vacuum vessel and torus hall during the accident

coolant release from the ruptured pipe is small enough. When the pressure in plasma vessel reaches 110 kPa, burst disk opens. Opening of the burst disk is followed by the pressure decrease in the vessel. Pressure in plasma vessel is decreasing due to the steam flowing out of the vacuum vessel to the torus hall. Pressure inside the torus hall stays almost constant, because the volume of this room is large, and flow rate of the steam is low and decreasing (Figure 2.13). Burst disk opens while the release of coolant from the ruptured pipe is still taking place. Mass flow rate through the burst disk reaches its biggest value (almost 4 kg/s) just after it has opened. However this initial big flow rapidly decreases to the values below 1 kg/s, due to decreasing flow of the coolant into the vessel and small pressure difference between torus hall and torus.

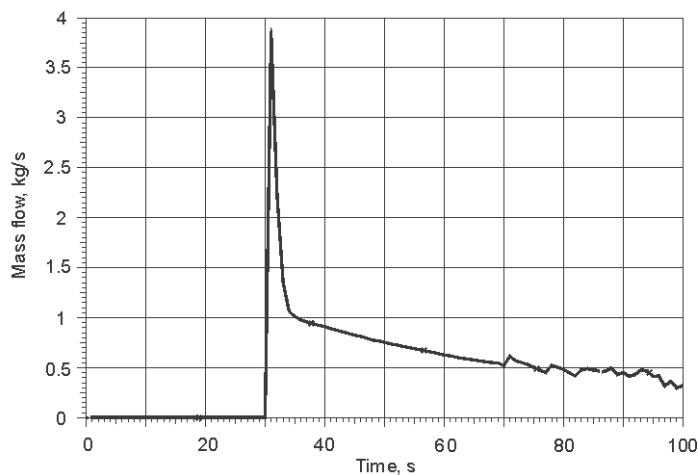


Figure 2.13
Obtained mass flow rate through the burst disk

Obtained results show that the area of the burst disk is sufficient to prevent pressure inside the vacuum vessel exceeding 110 kPa in the case of simulated accident. The behavior of pressure inside plasma vessel, calculated using COCOSYS code is very similar to calculations performed using RELAP5 code. This demonstrates the feasibility of “tandem” of two models: RELAP5 model for analysis of processes in targets cooling system and COCOSYS model for detailed analysis of processes in plasma vessel.

2.2 Integral analysis of LOCA using ASTEC code

2.2.1 Models of cooling system and plasma vessel for ASTEC code

For the modelling of selected accident (40 mm target pipe rupture) in “Baking” operation mode it is enough to develop detail model of “Baking” circuit. Thus, it was decided to develop detailed model of both connected circuits (see Figure 2.14 and Figure 2.15). The geometric characteristics (pipe lengths, elevations, pump parameters, heater power and valves parameters) and configuration of pipes (it is necessary for evaluation of form loss coefficients) were taken from W7-X facility design. The pump in the model was described by a pressure difference as a function of the flow rate. Pump model STRU PUMP available in the ASTEC code is used. For the modelling of the pressuriser a special type of node “swollen water level” was used. The valves from MCC and “Baking” circuit on inlet and outlet were modelled using ASTEC/CESAR module STRU SYSTEMS/VALVE. The non-return valves were modelled by a difference of the proportionality coefficients used in the calculation of the local pressure loss for reverse flows. The heater was modelled by the heat structure with defined initial temperature and the heat source of 180 kW.

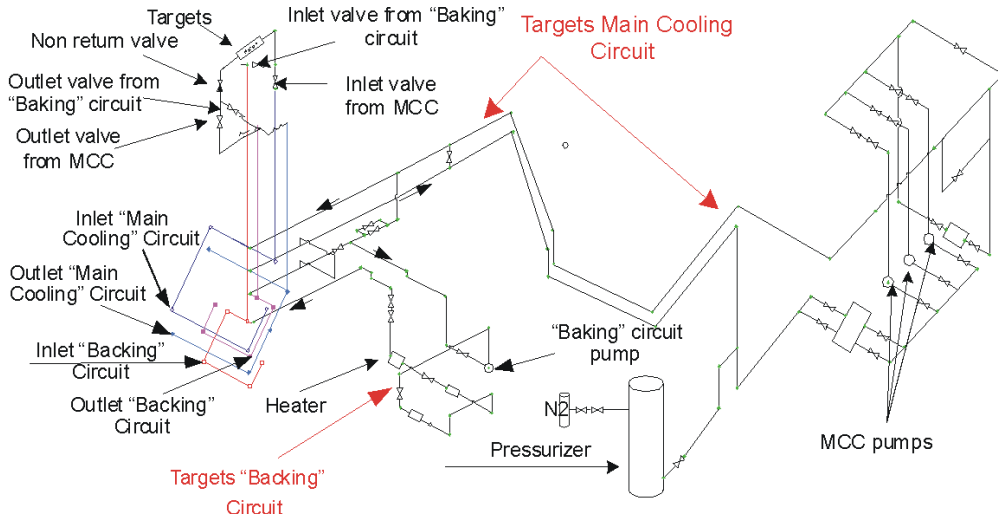


Figure 2.14
Nodalisation
scheme of W7-X
cooling system

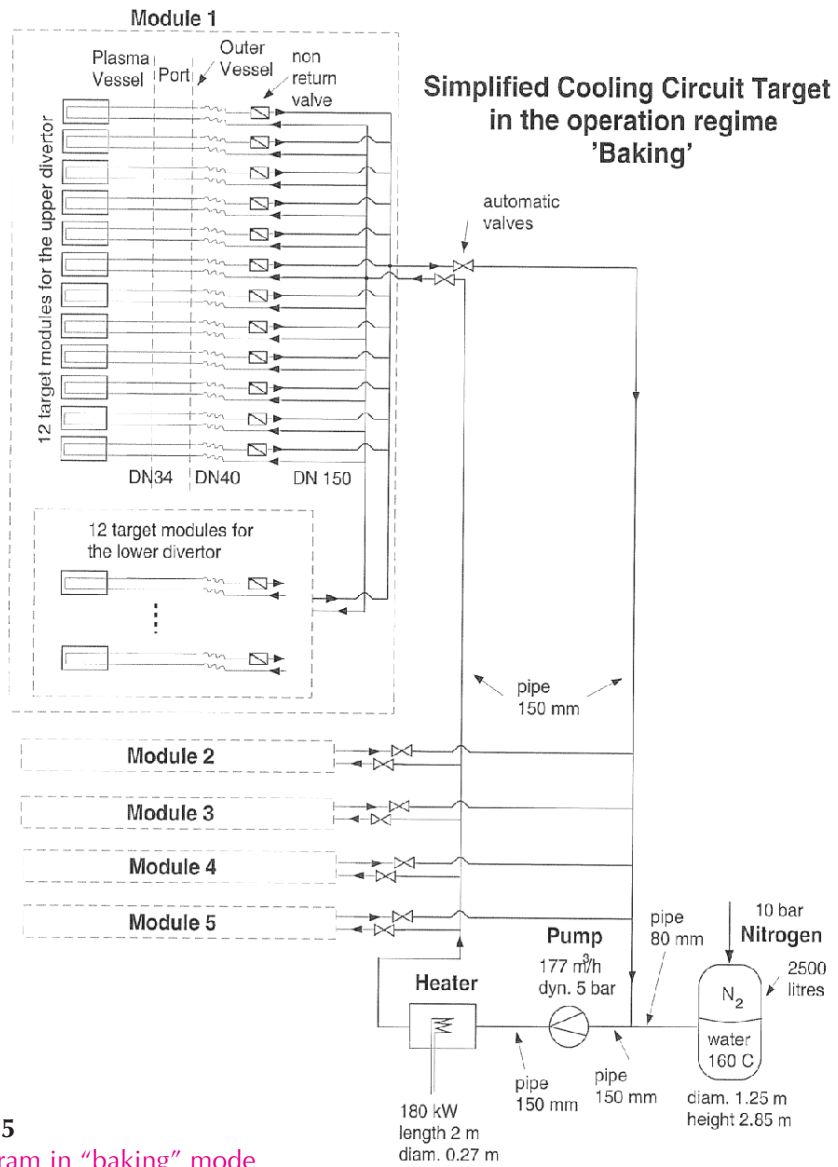


Figure 2.15
Flow diagram in "baking" mode

The simplified scheme for modelling of targets (nodalisation scheme) was developed (see Figure 2.16). As it is seen from presented scheme, four target modules are modelled as simplified one equivalent element: "F5-F5'", "G5-G5'", "H5-H5'", "J5-J5'".

One Target Module "E5-E5'" is modelled in more details (see Figure 2.17). There were modelled 8 Horizontal Targets in upper position (8THUP) and 8 Horizontal targets in lower position (8THD), 6 vertical targets (6TV) and was modelled two single vertical targets in lower and in upper position (1THD and 1THUP) these elements allows to model rupture of single target feeder pipe. For modelling of double ended guillotine break the ASTEC/CESAR connection module BREAK is used. Element "INJ" models the volume inside plasma vessel with pressure equal 1000 Pa.

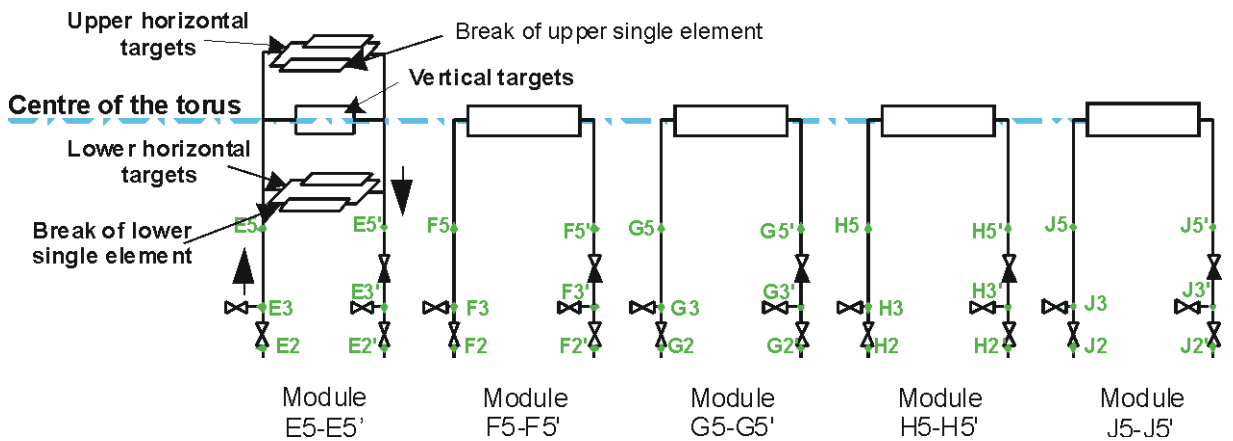


Figure 2.16
Modelling of targets (nodalisation scheme)

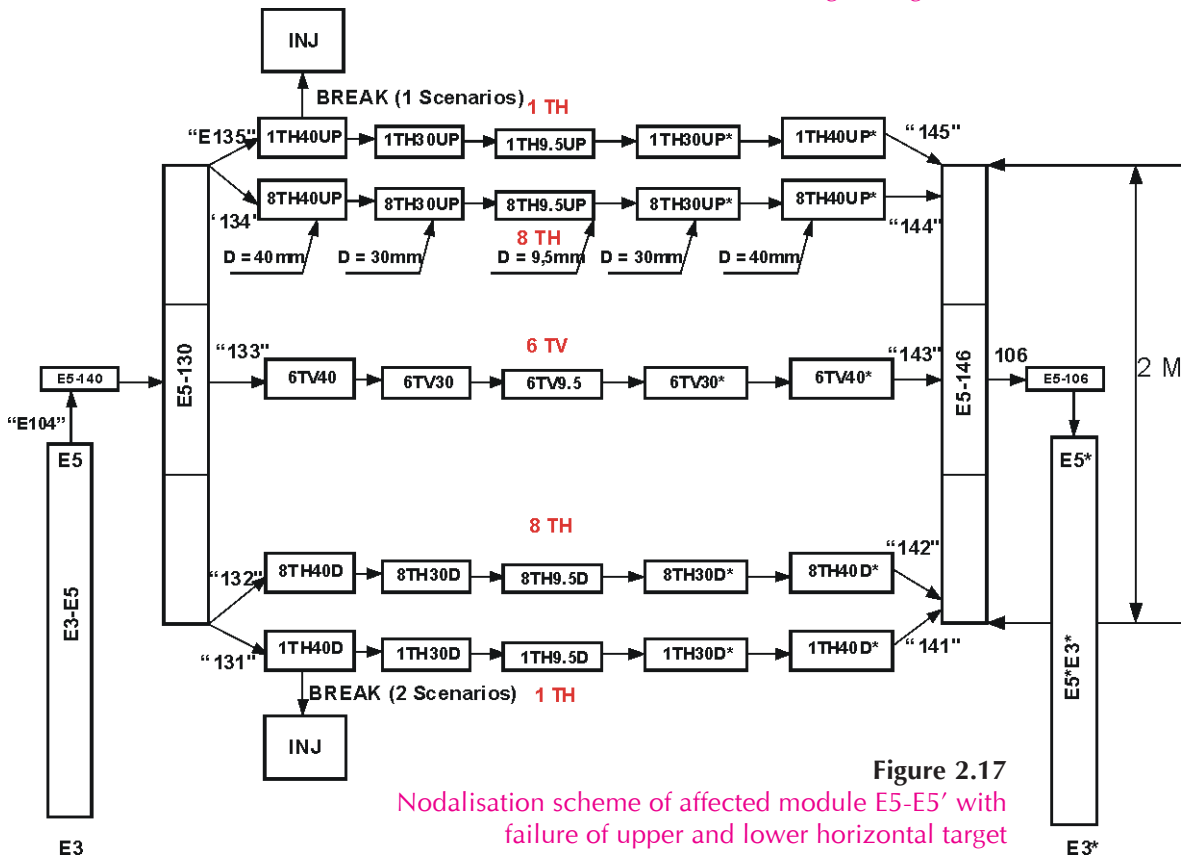


Figure 2.17
Nodalisation scheme of affected module E5-E5' with failure of upper and lower horizontal target

When the water is discharged from the cooling circuit into the plasma vessel there are two sources of steam production: 1) primary, when the water vaporises due to pressure drop, and 2) secondary, when the steam is generated due to water interaction with the hot structures of the plasma vessel. Both these steam sources lead to pressurisation of the plasma vessel. The plasma vessel is protected from overpressure by the burst disc. The simplified scheme of the plasma vessel pressurisation is presented in Figure 2.18.

Device is composed out of five parts with similar configurations, called modules. Each module of the vacuum vessel is subdivided into nine virtual control nodes (zones) in the scheme (Figure 2.18), four in the central part of the scheme cross-section (nodes C**), four in the outer part (nodes O**) and one in the bottom part (node BOT), in which released water is collected. Figure 2.18 shows cross-section of one module nodalisation scheme. All five modules are simulated in the analysis.

All adjacent zones of one module are connected by atmospheric junctions. Areas of these junctions and their lengths are calculated from the cylinder geometry. Corresponding zones of the adjacent modules (e.g., CBL zones of the first and second modules) except BOT zones also are connected by atmospheric junctions, properties of which are calculated from the geometry of cylinder.

INJ zone is the zone into which the water release from the ruptured pipe is simulated. It is defined for the aims of simulation – it helps to more realistically model the water flowing from the ruptured pipe to the wall of the vacuum vessel. INJ zone is present only in one module. Geometric parameters of this zone were selected according to port data and the initial thermodynamic parameters are the same as in the whole vacuum vessel. Two zones not presented in the Figure 2.18 were also simulated – torus hall and environment.

The former is a 16800 m³ volume hall in which stellarator torus is situated. Conditions in the hall were selected according to planned normal operation of W7-X device. OTL node of the vacuum vessel third module and torus hall node are separated by the simulated burst disc. Burst disc is simulated by defining an atmospheric junction, which is closed at the beginning and opens if pressure difference between the zones it connects reaches indicated value (direction considered). Area of this junction was set equal to the area of the burst disc.

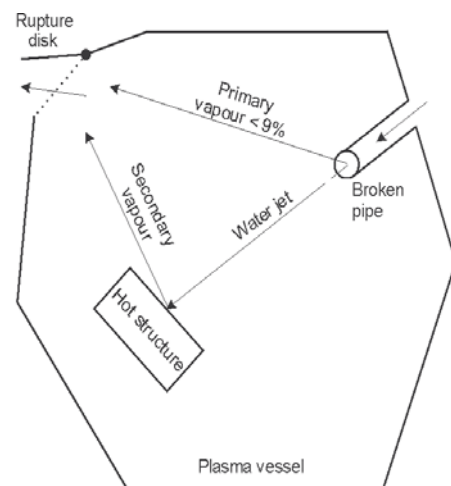


Figure 2.18
Scheme for plasma vessel pressurisation

2.2.2 Results of integral analysis

This section presents the results of analyses of 40 mm pipe rupture, connecting single upper or lower horizontal target. Double ended guillotine rupture of 40 mm pipe in “Baking” mode was modelled with the integral code ASTEC. Before accident the water temperature in the “Baking”

circuit is 433.16 K (160 C) and density – 907 kg/m³. The water flow rate through “Baking” circuit is 177 m³/h (44.6 kg/s). The pressure in plasma vessel is 1000 Pa. Valves from the main cooling circuit to targets are closed on inlet and outlet. Valves from the “Baking” circuit are open on inlet and outlet.

In this paper there are analysed two different scenarios:

1. Double ended guillotine rupture of DN40 pipe in the upper target.
2. Double ended guillotine rupture of DN40 pipe in lower target.

In the model it was assumed that the rupture occurs in the module E5-E5' (see Figure 2.19). The rupture occurs in DN40 feeder pipe, connecting single upper horizontal target (element “1TH40UP” in Figure 2.19) and another scenarios, the break occurs in lower DN40mm horizontal target (element “1TH40D” in Figure 2.19). The boundary conditions are the same in both cases (see Table 2.1)

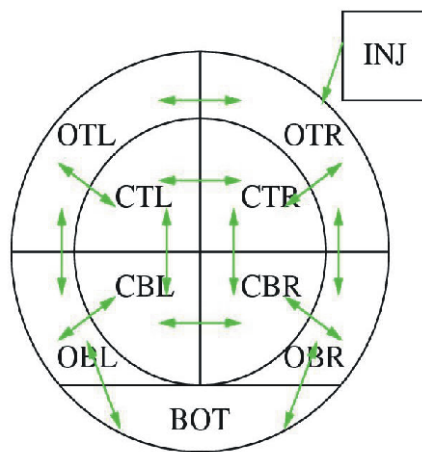


Figure 2.19

Cross-section of the developed nodalisation scheme of the vacuum vessel for one module (black – nodalisation nodes, green – atmospheric junctions)

Table 2.1. The following events were assumed to occur:

1.	T = 0.0 s	Double ended guillotine break of DN40 (inner diameter 0.0443 m) occurs.
2.	T = 1.14 s	Trip of pump on “Baking” circuit
3.	T = 1.64 s	Closure of valves on Target inlets begins.
4.	T = 6.64 s	Valves on Target inlets are fully closed.

The discharge of the coolant through the ruptured pipe and water flow rate into affected module are presented in Figure 2.20. From this figure we can see, that water flow into the affected target stops when the automatic valves are closed. After closure of the inlet automatic valves, the discharge of coolant slightly decreases, but the water from other targets in this module is discharged until pressure in the affected targets decreases down to the pressure in the plasma vessel. Since the inlet automatic valves are closed, the water is discharged only from the affected module.

The pump trip leads to pressure decrease in the pump outlet (see Figure 2.21). The pressure in other modules drops down to ~ 0.6 MPa and remains constant, because the automatic valves have isolated them. Pressure in affected target decreases down to pressure in plasma vessel 105 s after the break.

The process of emptying of the targets in affected target module can be understood from Figure 2.22 and Figure 2.23. This figure shows the behaviour of void fraction in the targets is presented 0 - means pure water, 1 – pure steam. The affected target “1TH – upper” will be empty after

approximately 105 s, 8 horizontal upper targets (8THUP) will be empty after approximately 40 s. 6 vertical targets will be empty after approximately 135 s. But in lower horizontal Targets remains some amount of water.

Figure 2.20
Water flow rate into affected module and discharge of coolant through the break

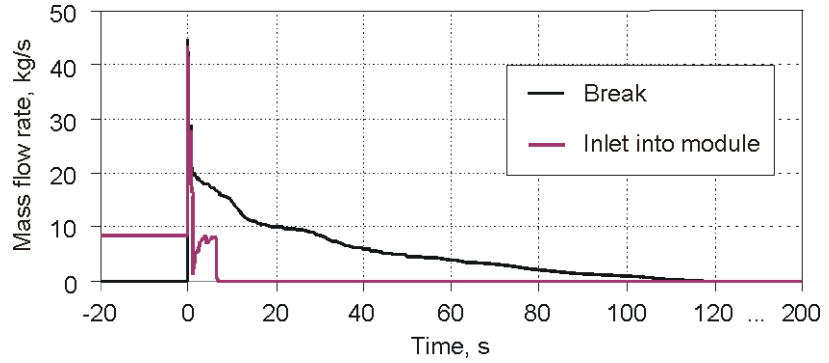


Figure 2.21
Pressure in "Baking" circuit

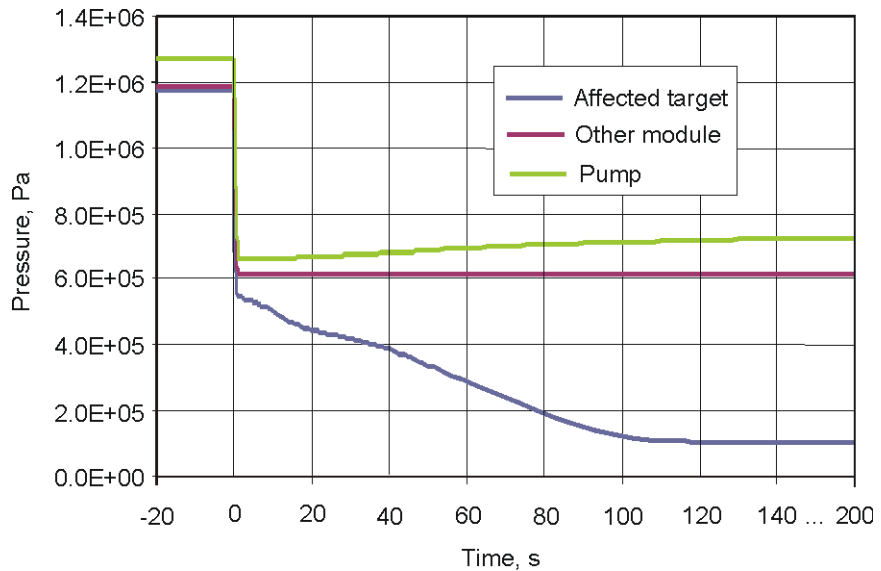
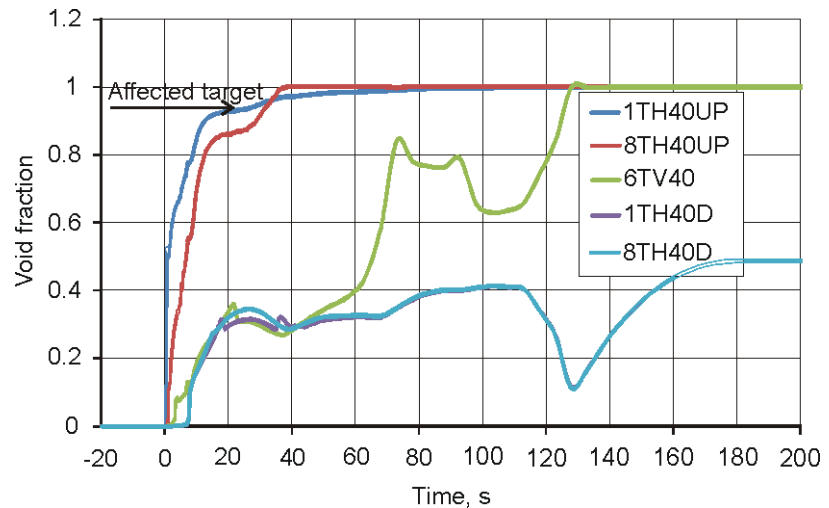


Figure 2.22
Void fraction in the affected Target Module



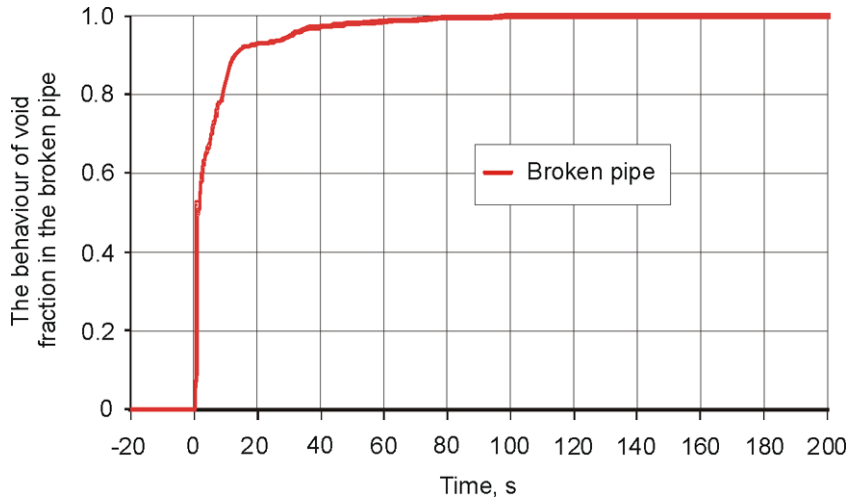


Figure 2.23
Void fraction in the broken pipe

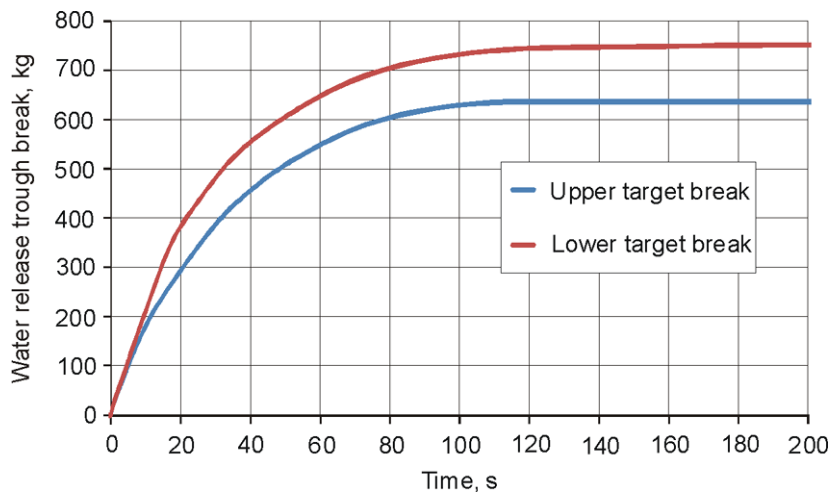


Figure 2.24
Comparison of upper and lower target break scenarios. Total water release through the breaks

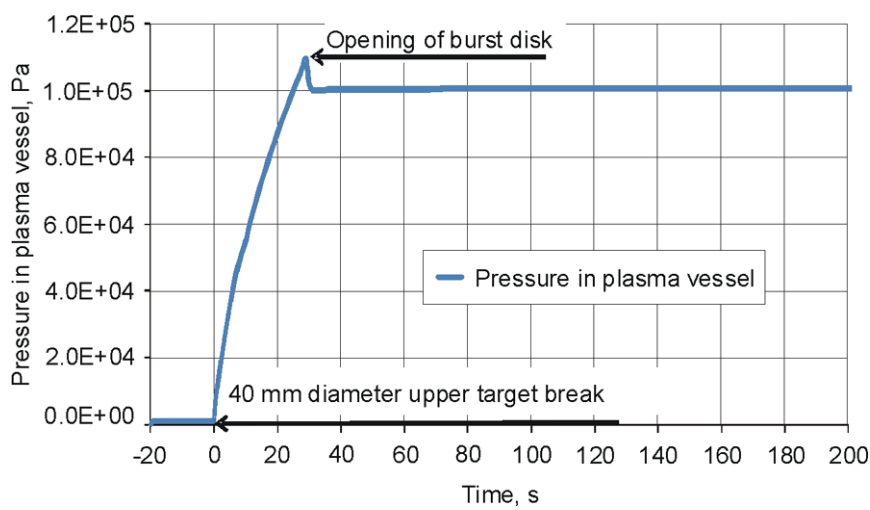


Figure 2.25
Behaviour of pressure in plasma vessel

Figure 2.24 shows the comparison of two scenarios of analyzes (Upper 1TH40UP break) and (Lower 1 TH40D break). The total water release from the break is approximately 100 kg lager in

case of lower 1 horizontal target break.

The Figure 2.25 shows that the pressure rapid increase in the plasma vessel and in 30 s the pressure increases to the set point of safety valve opening (burst disc), which prevents further rise of pressure. These results showed that the planned area of the burst disk should be sufficient to prevent pressure inside the vacuum vessel exceeding 1.1 bar in the case of simulated accident.

2.3 Structural analysis concerning Loss of Vacuum Accident. Assessment of critical port/plasma vessel connections

The W7-X cryostat mainly consists of the Outer Vessel (OV), the Plasma Vessel (PV), and the ports with bellows that connect the vessels. The PV is the innermost cryostat wall, with its shape generally following that of the plasma. The PV provides a physical separation between the plasma and the rest of the system.

Each port is basically a tube (sometimes called a “nozzle”) with a round, oval, rectangular or irregular cross section. In a place where the port is attached to the PV, the PV shell has an opening with a corresponding shape. The port is inserted into the opening in the PV shell until it reaches approximately one half of the shell thickness, and is welded to the PV shell from inside. During assembly the other side of the weld (i.e. the one facing the magnet system) is not accessible, because the layout inside the cryostat is designed so tight that the coils almost touch the thermal insulation of the ports and the vessels. (The space tolerances are normally within 30–50 mm range.) Therefore all these welds are performed from one side only.

Between the PV and the OV there are 254 ports, each of them is attached to the PV at one end, and to the OV, at the other end. One can distinguish two types of ports, the diagnostic ports (Type I) and the supply ports (Type II). A port of type I has two tubes, one of them is welded to the shell of the PV (let us call it “the port tube on the side of the PV”), and the other is welded to the dome plate of the OV (“the port tube on the side of the OV”).

The diagnostic port consists of two port tubes and the bellows between the tubes. The supply port has one long tube that is attached to an OV dome through the bellows. The bellows allow the tubes to undergo large relative movement without structural damage. There are 16 types of the bellows, which can have round, oval or rectangular cross-sections.

The port wall can have one of the following thicknesses (depending on the port type): 3 mm, 6 mm, 8 mm, 12 mm and 15 mm.

The structural integrity analysis of the welding connections was analyzed for the following ports / port combinations:

1. Welding connection between the port AEQ20 and the PV shell.
2. Welding connection between the port AEU30 and the PV shell.
3. Welding connection between the port AEK20 and the PV shell.

The structural integrity analysis of these port welds between PV and the ports in W7-X cryostat system was performed using finite element method. The models of port welds were prepared using software’s SolidWorks [5] and Brigade/Plus [6]. Software SolidWorks was used for preparing the geometrical models of these port welds. The finite element (FE) models of these port welds were prepared using software Brigade/Plus. The analysis of these FE models was carried out using BRIGADE/Plus software.

2.3.1 Geometrical and finite element models of the port welds

The modelling of the welding connection between the port AEQ20, AEU30, AEK20 and the PV shell was performed in two steps. In the first the geometrical 3D models of these port welds were

prepared using the software SolidWorks [5]. The prepared models are presented in the Figure 2.26 - Figure 2.28. These models were transferred to FE software BRIGADE/Plus [6]. The finite element models of the welding connection between the port AEQ20, AEU30, AEK20 and the PV shell was prepared using this software. The prepared models are presented in the Figure 2.29 - Figure 2.31.

Linear four node shell elements of ABAQUS, S4 [7], are used for modelling of the part of PV and ports. Central part, part of plasma vessel, weld and port (see Figure 2.29 b, Figure 2.30 b, Figure 2.31b) are modelled as solid, are meshed using a 20-node linear brick element C3D20 [7].

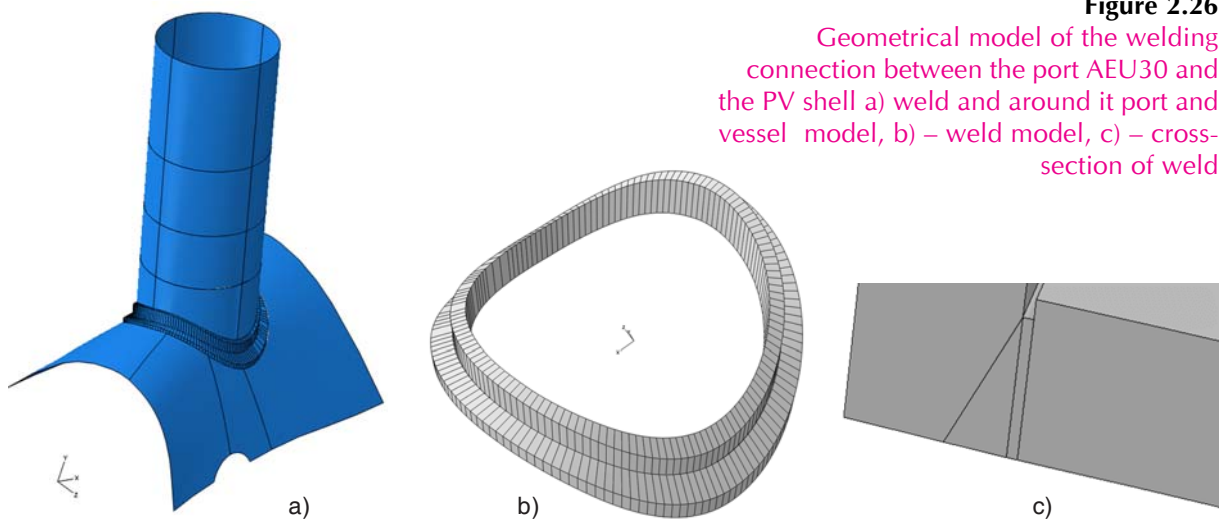


Figure 2.26
Geometrical model of the welding connection between the port AEU30 and the PV shell a) weld and around it port and vessel model, b) – weld model, c) – cross-section of weld

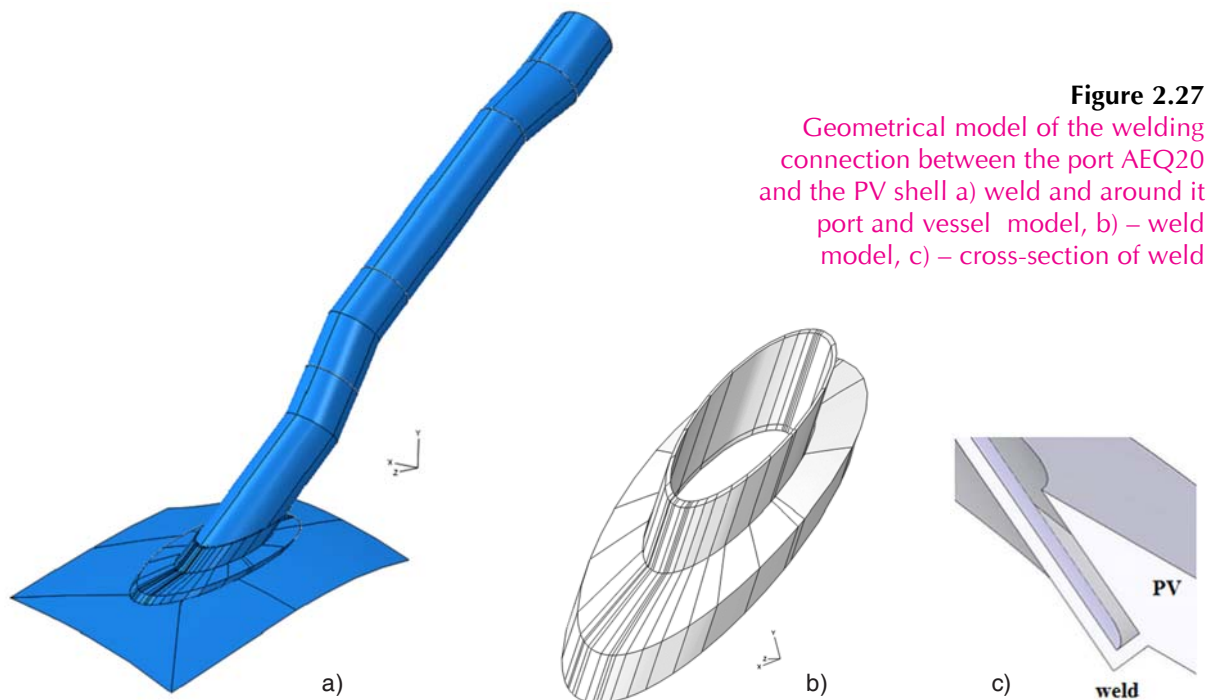
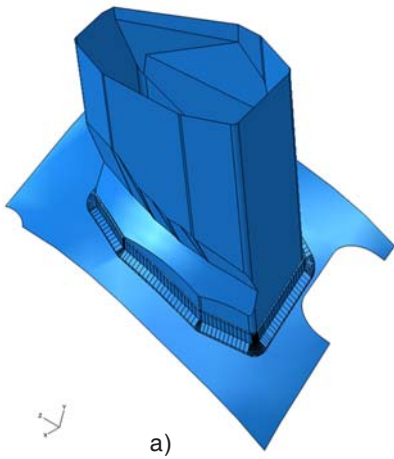
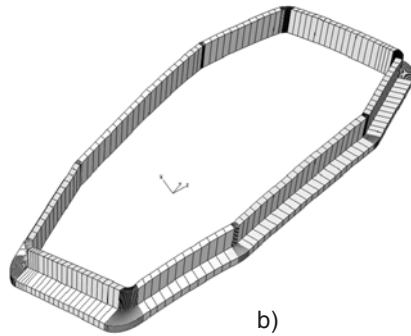


Figure 2.27
Geometrical model of the welding connection between the port AEQ20 and the PV shell a) weld and around it port and vessel model, b) – weld model, c) – cross-section of weld

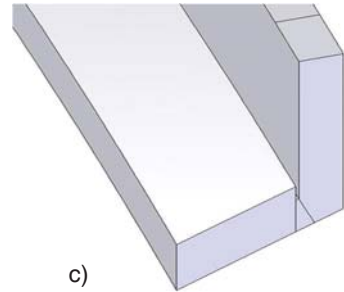


a)

Figure 2.28
Geometrical model of the welding connection between the port AEK20 and the PV shell a) weld and around it port and vessel model, b) – weld model, c) – cross-section of weld



b)

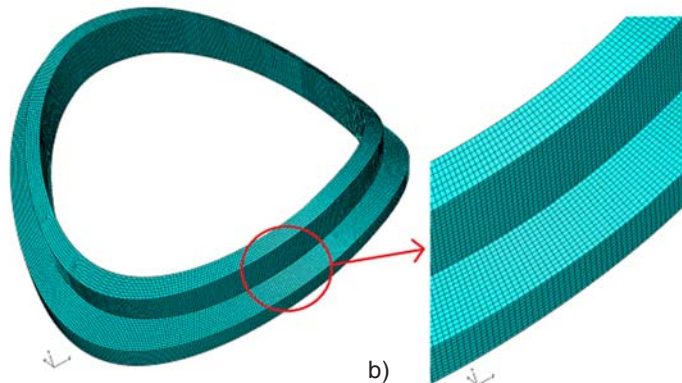


c)

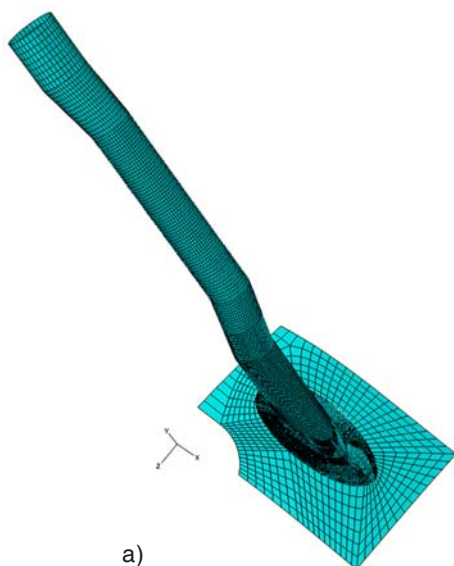


a)

Figure 2.29
FE model of the welding connection between the port AEU30 and the PV shell a) weld and around it port and vessel model, b) – weld model

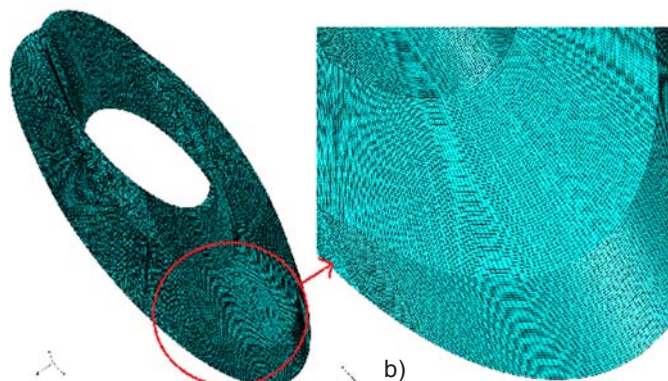


b)

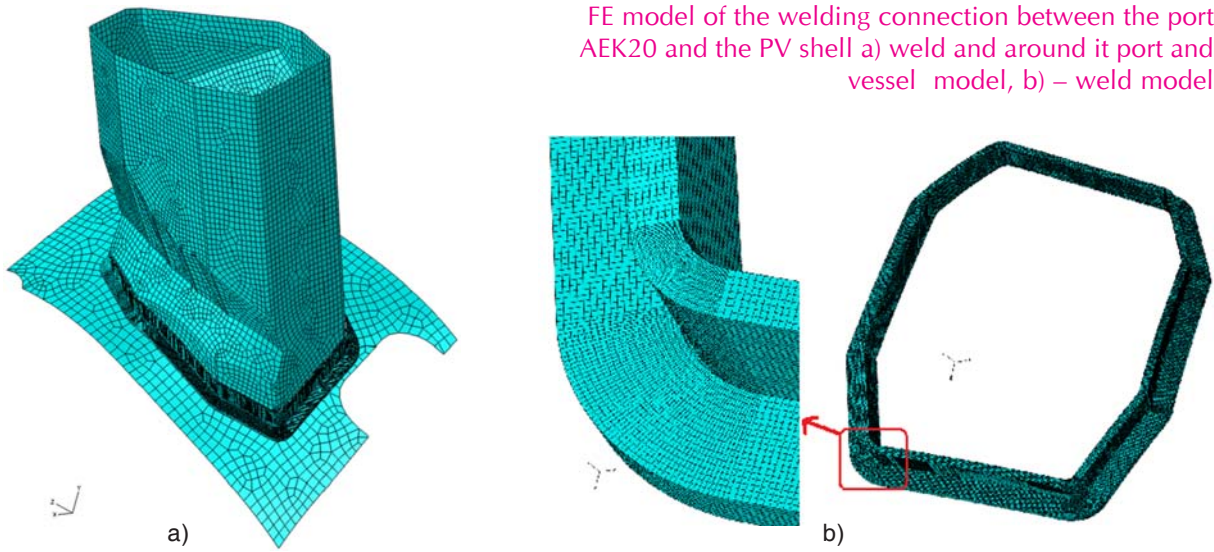


a)

Figure 2.30
FE model of the welding connection between the port AEQ20 and the PV shell a) weld and around it port and vessel model, b) – weld model



b)

**Figure 2.31**

FE model of the welding connection between the port AEK20 and the PV shell a) weld and around it port and vessel model, b) – weld model

2.3.2 Material properties

The geometrical and material data of the welding connection between the port AEU30, AEQ20, AEK20 and the PV shell are presented in Table 2.2. The names of the port welds parts used in Table 2.2 are presented in Figure 2.32 - Figure 2.34.

Table 2.2 Material properties

<i>Property</i>	<i>T, °C</i>	<i>Shell-AEQ-1, Shell-AEQ-2</i>	<i>Shell-AEU-2</i>	<i>Shell-AEK-2</i>	<i>Shell-AEK-3</i>
Thickness, mm	–	16.05	2.4	14.05	4.3
Density, kg/mm ³	0–100	2.0511×10^{-05}	2.6182×10^{-05}	1.1513×10^{-05}	1.3214×10^{-5}
Young modulus, MPa	0	1.98×10^5			
	20	1.96×10^5			
	100	1.90×10^5			
Poisson's ratio	0–100	0.3	0.3	0.3	0.3
Coefficient of thermal expansion, K ⁻¹	0	1.60×10^{-5}			
	20	1.61×10^{-5}			
	100	1.67×10^{-5}			

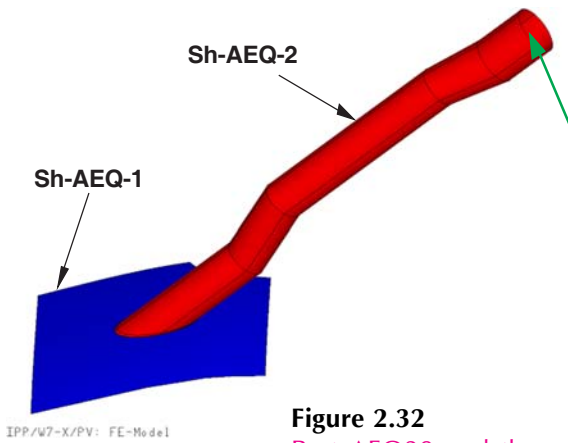


Figure 2.32
Port AEQ20 and the PV shell around it

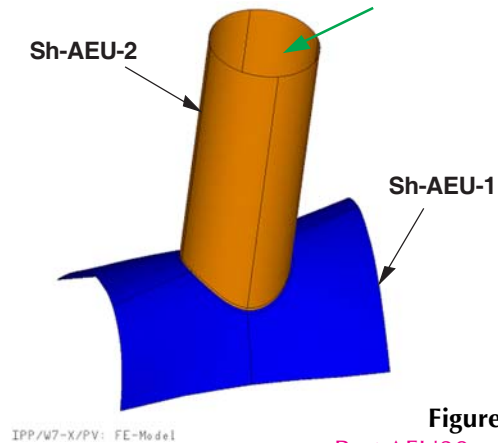


Figure 2.33
Port AEU30 and the PV shell around it

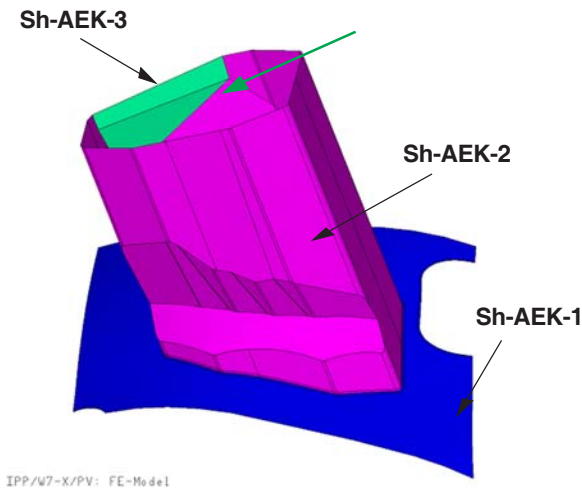


Figure 2.34
Port AEK20 and the PV shell around it

2.3.3 Boundary condition of the model

In order to simulate the load case 5 (LC5), the outer boundaries of the PV (marked with “Sh-AEQ-1”, “Sh-AEU-1” and “Sh-AEK-1” in Figure 2.32 – Figure 2.34) was constrained in the following way, the displacements of the edges should be restricted in all directions, but rotations are allowed. Boundary conditions were applied in such a way that only the global displacements of the shell at the edges were restricted, but not the local deflection of the shell.

2.3.4 Applied Loading for Structural Integrity Analysis

The loads that should be applied at the loading step that corresponds to the loading factor of 1.0 are listed in Table 2.3. “Outer pressure” means that the pressure is applied from the side where the port is attached to the PV shell. The loads are multiplied with the safety value of 1.2 in order to take possible imprecision of the modeling into account.

Table 2.3 Loads on the sub-model for the LC 5

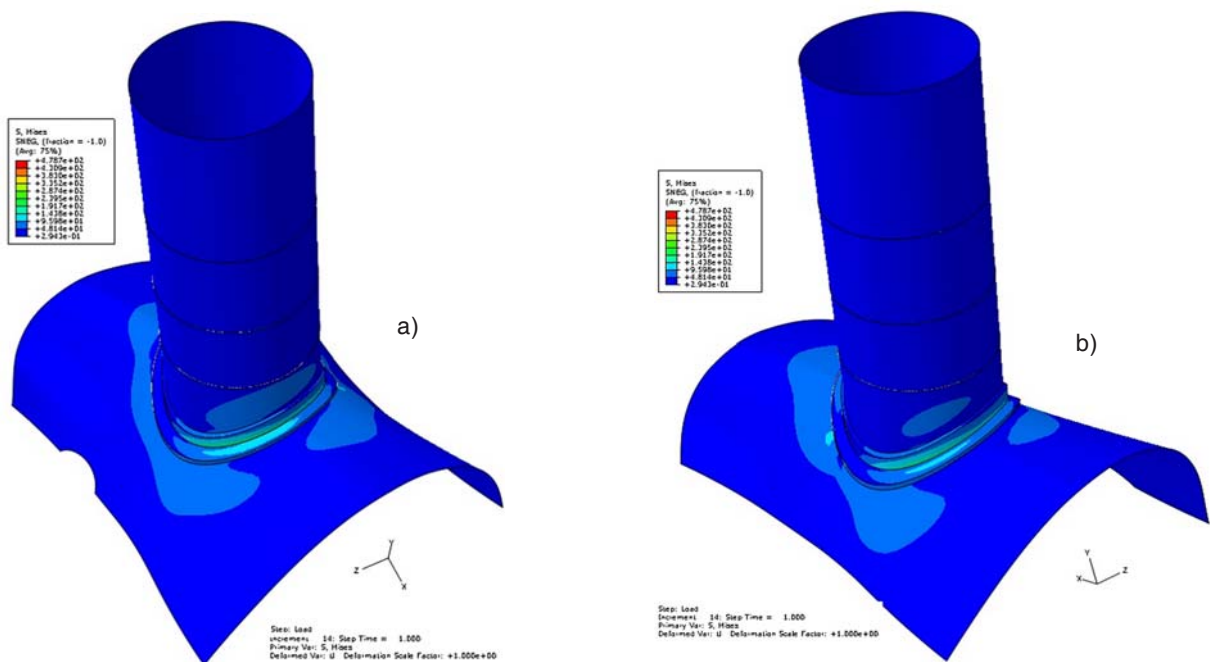
Load type	Direction	Port AEQ20	Port AEU30	Port AEK20
Temperature, °C	–	20		
Outer pressure, MPa	–	$0.1013 \times 1.2 = \mathbf{0.1216}$	$0.1013 \times 1.2 = \mathbf{0.1216}$	$0.1013 \times 1.2 = \mathbf{0.1216}$
Forces applied the end of the port (marked with thick green arrows in Fig. 11–12)	F_x , kN	$-1.004 \times 1.2 = \mathbf{-1.205}$	$26.034 \times 1.2 = \mathbf{31.241}$	$-3.706 \times 1.2 = \mathbf{-4.447}$
	F_y , kN	$1.421 \times 1.2 = \mathbf{1.706}$	$-16.458 \times 1.2 = \mathbf{-19.749}$	$-2.728 \times 1.2 = \mathbf{-3.274}$
	F_z , kN	$0.223 \times 1.2 = \mathbf{0.268}$	$3.515 \times 1.2 = \mathbf{4.218}$	$2.745 \times 1.2 = \mathbf{3.294}$
Moments applied the end of the port (marked with thick green arrows in Fig. 11–12)	M_x , kN*mm	$32.700 \times 1.2 = \mathbf{39.240}$	$214.009 \times 1.2 = \mathbf{256.811}$	$15039 \times 1.2 = \mathbf{18047}$
	M_y , kN*mm	$-40.799 \times 1.2 = \mathbf{-48.959}$	$4163.394 \times 1.2 = \mathbf{4996.073}$	$-13759 \times 1.2 = \mathbf{-16511}$
	M_z , kN*mm	$17.441 \times 1.2 = \mathbf{20.929}$	$-26504 \times 1.2 = \mathbf{-31804}$	$14640 \times 1.2 = \mathbf{17568}$

2.3.5 Analysis of stress in the welding between Plasma Vessel and ports with gap 1 mm

A validated finite element (FE) code BRIGADE/Plus, that includes integrated ABAQUS [7] solver technology [6], is used for numerical simulation of the welding between PV and ports. The results of the analysis of the port welds are presented in this section.

2.3.5.1 Analysis of stress in the welding between Plasma Vessel and ports AEU30 with gap 1 mm

Stress distributions in model in the welding between Plasma Vessel and ports AEU30 with gap 1mm are presented in Figure 2.35.

**Figure 2.35**

Stress distribution in full model, a) – left view, b) – right view

Maximal stress level obtained in model is 479 MPa. These stresses are obtained on the boundary of shell to solid coupling in the solid body of plasma vessel (Figure 2.42, Figure 2.43). The stresses in nodes of element with value of stress 479 MPa are presented in Table 2.5. The average value of stress in this element is 170.9 MPa (in centroid).

In the shell part of plasma vessel maximal Von Misses stresses are 144 MPa (Figure 2.36). In the shell part of port maximal Von Misses stresses are 60 MPa (Figure 2.37).

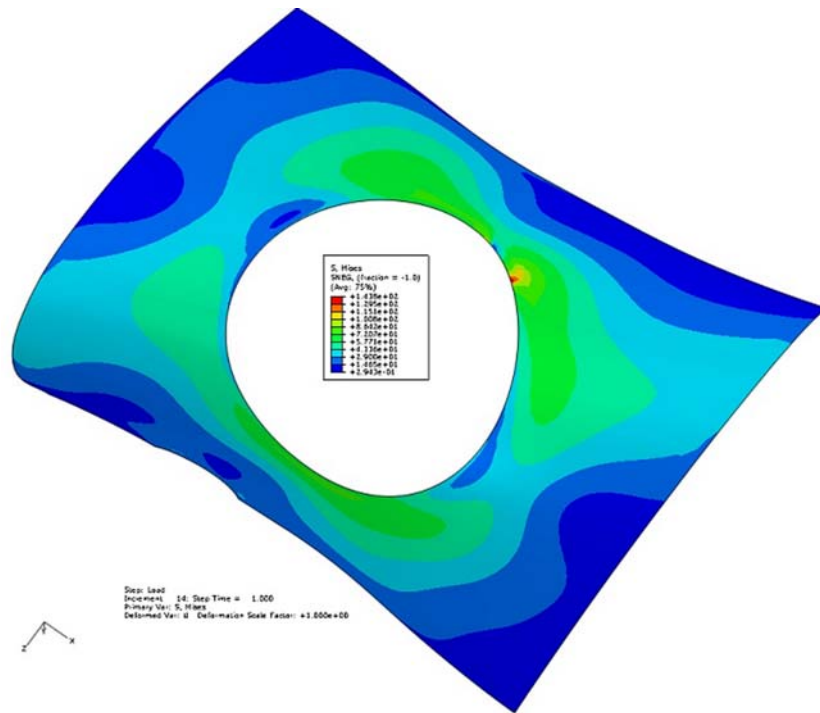


Figure 2.36
Stress distribution in shell part of plasma vessel

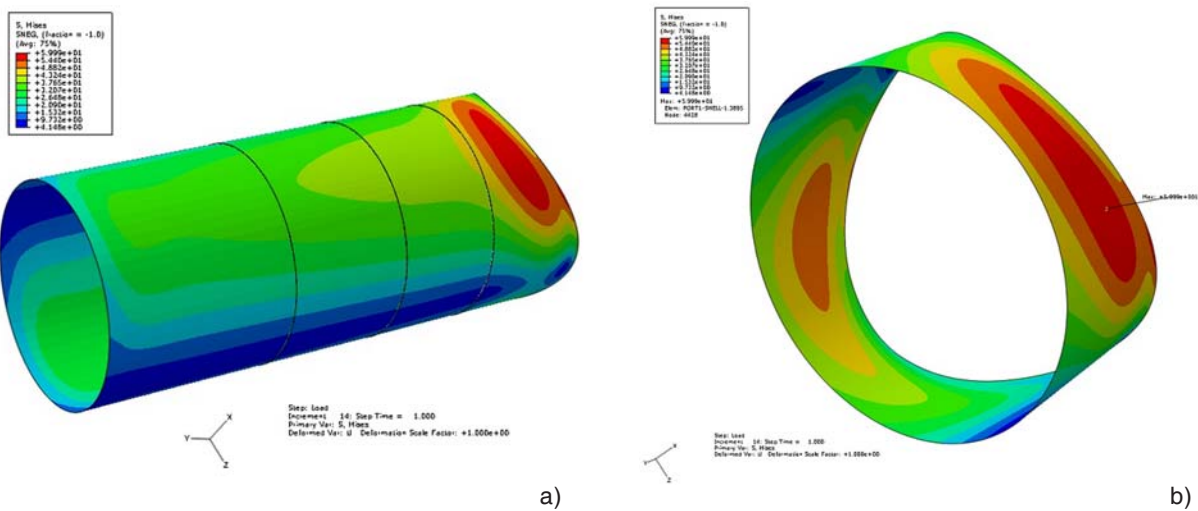


Figure 2.37
Stress distribution in port, a) – full view, b) – close view of maximal stresses distribution (60 MPa)

Main interest is welded zone of the port and PV, modelled as 3D solid. Maximal obtained stress level is 417 MPa, on the wall of port, close to the edge of weld tip. In weld maximal stress level is 396 MPa (Figure 2.38 - Figure 2.41). The stresses in nodes of element with value of stress 417 MPa are presented in Table 2.4. The average value of stress in this element is 203.7 MPa (in centroid).

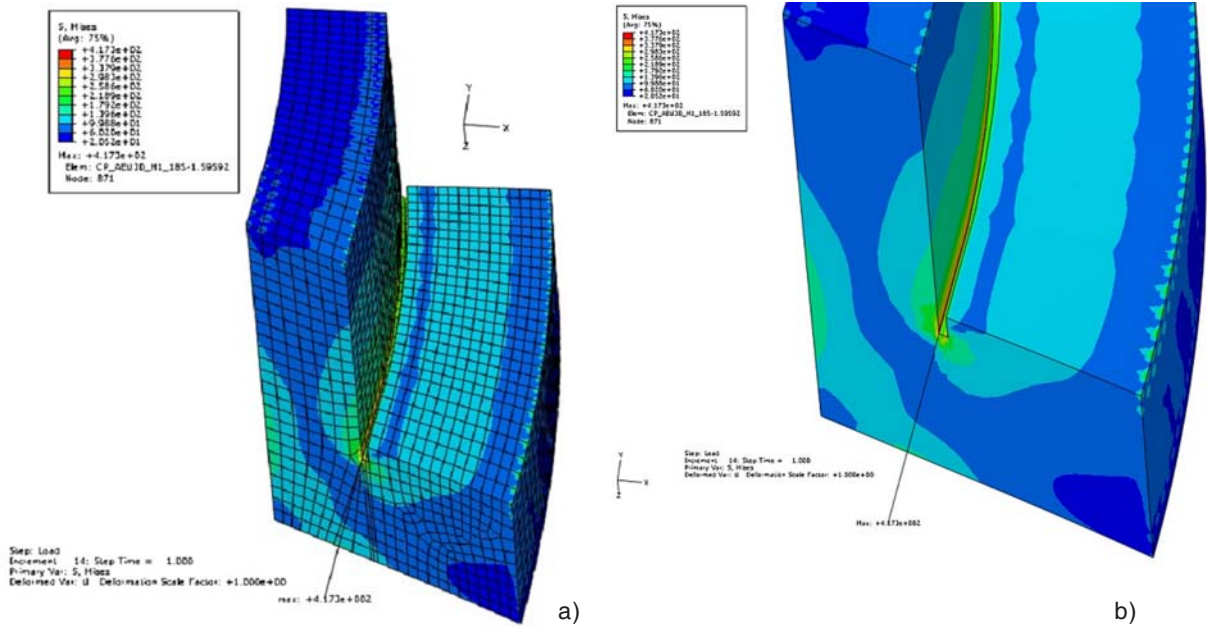


Figure 2.38

Stress distribution in solid part, a) – weld-PV area, b) – close view of stress distribution in modelled solid port-weld-PV area

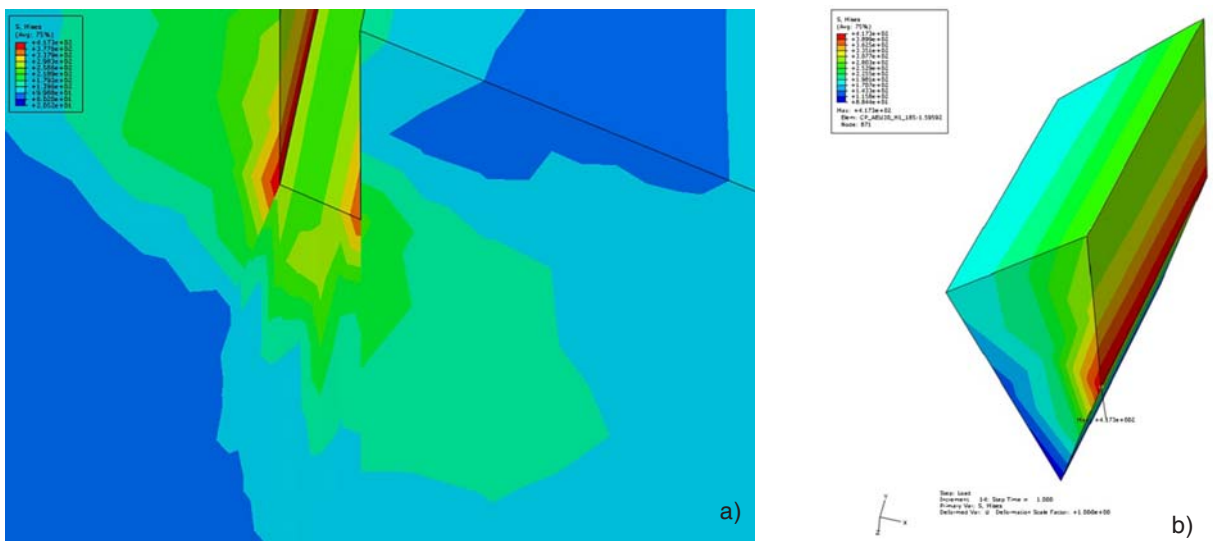


Figure 2.39

Stress distribution in solid part, a) – close view of cross section of port, weld, PV through maximal 417 MPa stresses, b) – Stress distribution in selected element of maximal stress 417 MPa

Table 2.4 Stresses in nodes of element with value of stress 417 MPa

Node	S, Mises, MPa (Not averaged)	Node	S, Mises, MPa (Not averaged)
56585	235.245	456544	147.698
11616	104.916	456539	233.466
56743	101.124	456547	316.496
146832	231.71	456548	411.23
11597	309.602	456549	309.41
871	416.289	456542	308.927
11604	406.325	456543	209.108
56534	308.42	456550	227.59
456546	152.144	456551	219.513
456545	102.991	456538	205.001

Figure 2.40
Stress distribution with removed elements of maximal stress 479 MPa spot, maximal stresses are 417 MPa

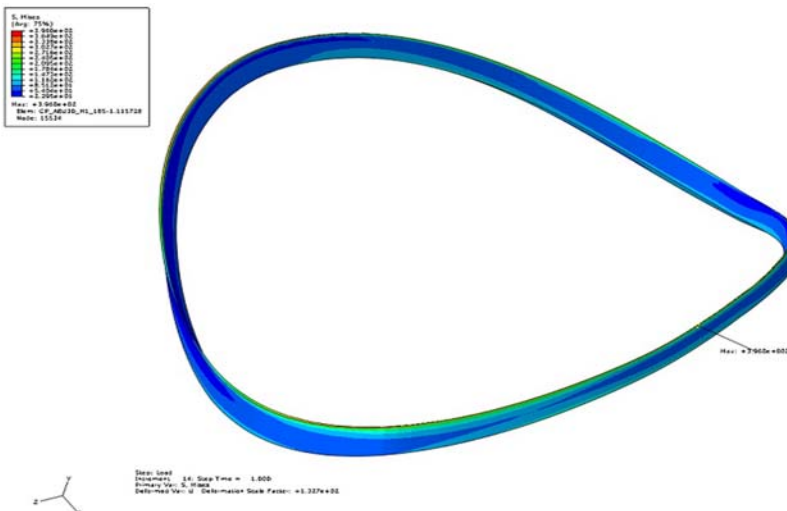
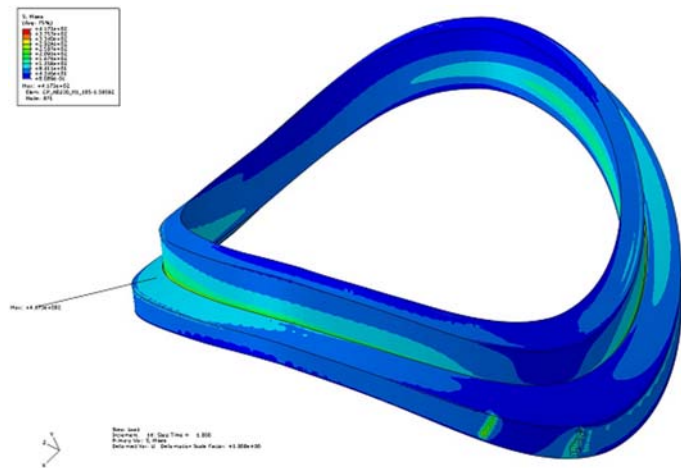


Figure 2.41
Stress distribution in modelled solid weld, maximal stresses 396 MPa

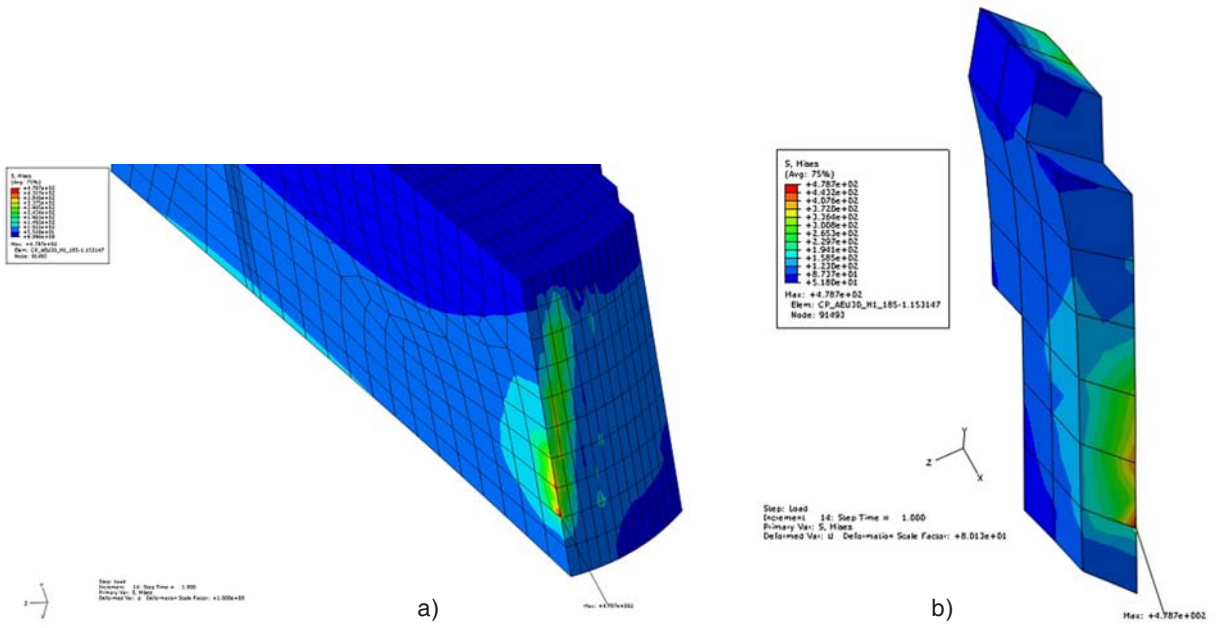


Figure 2.42
 Stress distribution in solid part, a) – the cross section of port, weld, PV through maximal 479 MPa stresses, b) – stress distribution in removed elements of maximal stress 479 MPa spot

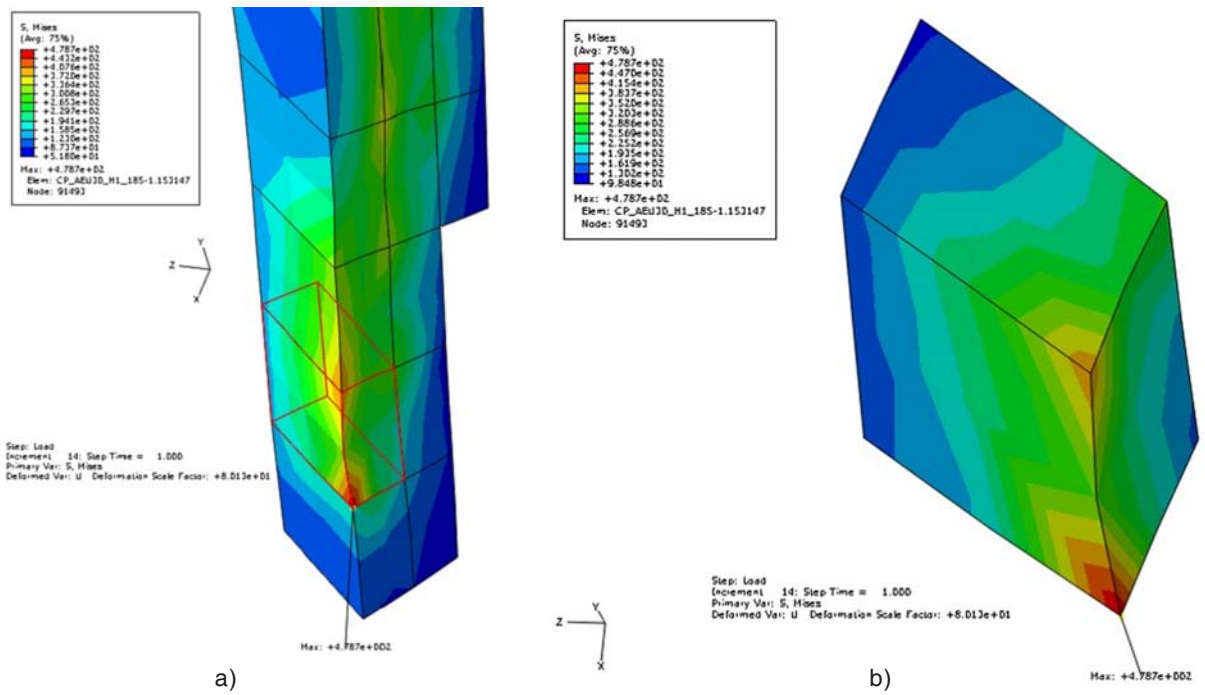


Figure 2.43
 Stress distribution in solid part, a) – stress distribution in removed elements of maximal stress 479 MPa spot, element selected, b) – stress distribution in selected element of maximal stress 479 MPa

Table 2.5 Stresses in nodes of element with value of stress 479 MPa

<i>Node</i>	<i>S, Mises, MPa (Not averaged)</i>	<i>Node</i>	<i>S, Mises, MPa (Not averaged)</i>
18402	112.789	745972	122.088
18401	303.823	745973	93.7496
91315	136.203	746484	311.022
91316	116.875	746480	260.957
91493	478.729	746485	158.74
91492	378.81	746486	265.979
202435	189.717	746487	289.424
202436	143.197	746483	238.115
745971	194.608	746482	156.415
745967	171.408	746488	122.77

According analysis results it was received that the stresses in port and vessel is below yield strength which is 320 MPa. The stresses in welded zone of port and PV in surface of some distorted element exceed the yield strength (for weld material 272 MPa), but average value of stresses are below the yield strength. The distorted element was received due to complexity of geometry of analysed structure. The influence of these distorted elements to stress condition of all structure is minor.

Therefore the stability of the welding between Plasma Vessel and ports AEU30 with gap 1mm will be sustained at used loading for analysis.

2.3.5.2 Analysis of stress in the welding between Plasma Vessel and ports AEQ20 with gap 1 mm

Stress distributions in model of the the welding between Plasma Vessel and ports AEQ20 with gap 1mm are presented in Figure 2.44.

In the shell part of plasma vessel maximal Von Misses stresses are 24 MPa (Figure 2.45). In the shell part of port maximal Von Misses stresses are 89 MPa (Figure 2.46).

Main interest is welded zone of port and PV, modelled as 3D solid (Figure 2.47 - Figure 2.50). Maximal obtained stress level is 252 MPa (Figure 2.49, Figure 2.50), on the wall of port, close to the edge of weld tip. These stresses are obtained on the boundary of port to weld are in the solid body of port. In weld maximal stress level is 154 MPa (Figure 2.48).

According analysis results it was received that the stresses in port, PV and weld are below yield strength (for main material 320 MPa, for weld material 272 MPa).

Therefore the stability of the welding between Plasma Vessel and ports AEQ20 with gap 1 mm will be sustained at used loading for analysis.

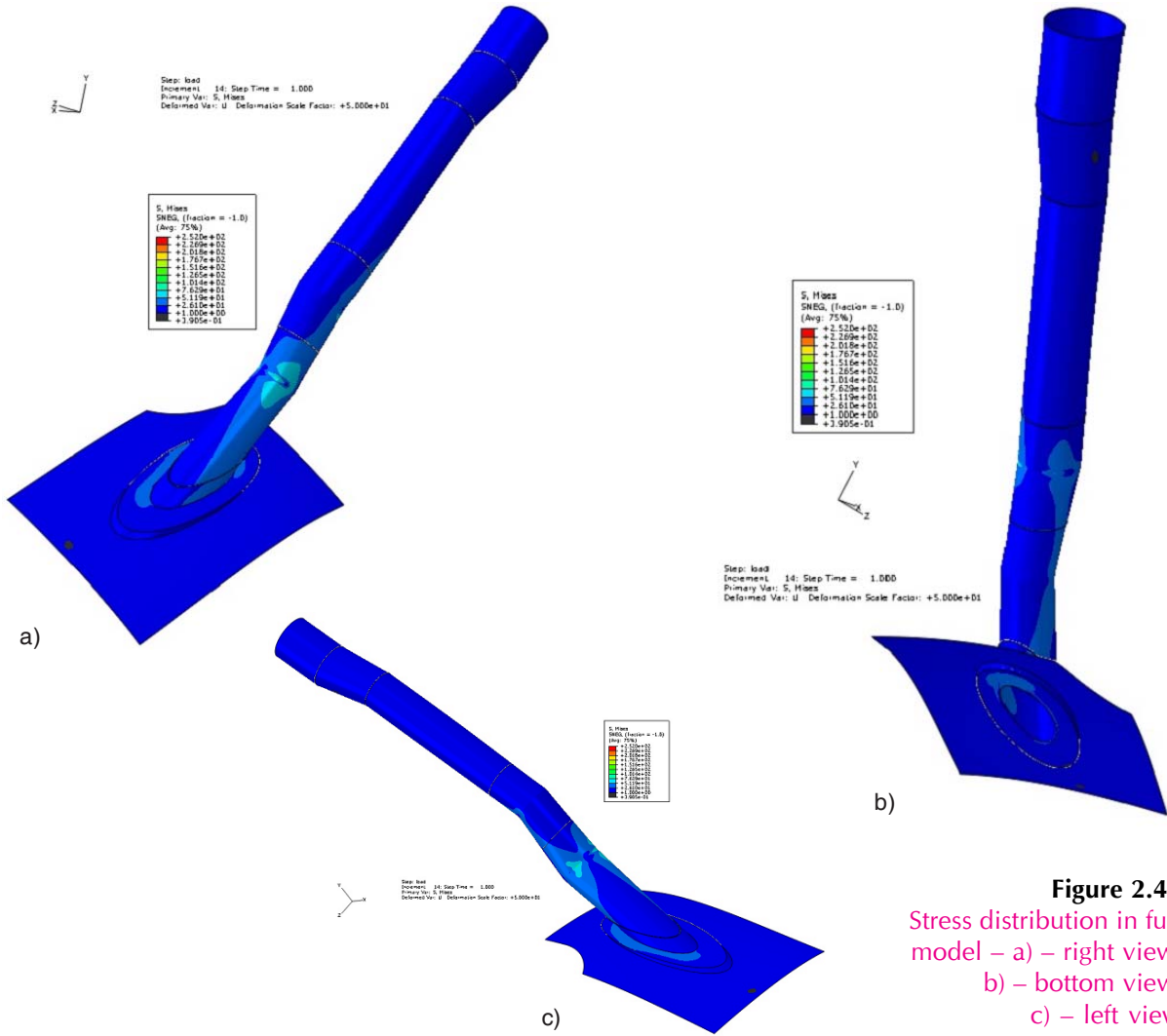


Figure 2.44
 Stress distribution in full model – a) – right view,
 b) – bottom view,
 c) – left view

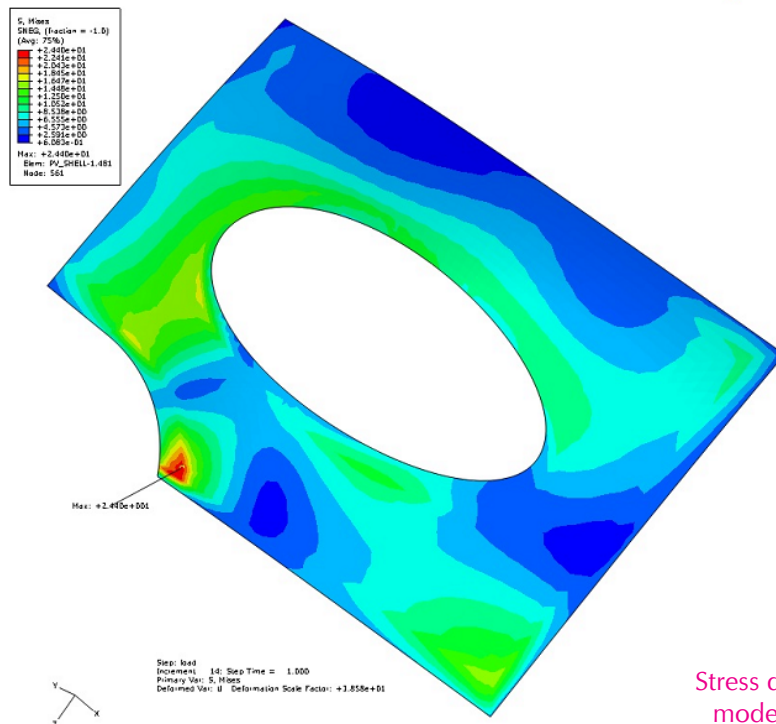


Figure 2.45
 Stress distribution in shell
 modelled plasma vessel

Figure 2.46

Stress distribution in shell modelled port, a) – full view, b) – close view of stress distribution in shell modelled port, maximal stresses 89 MPa

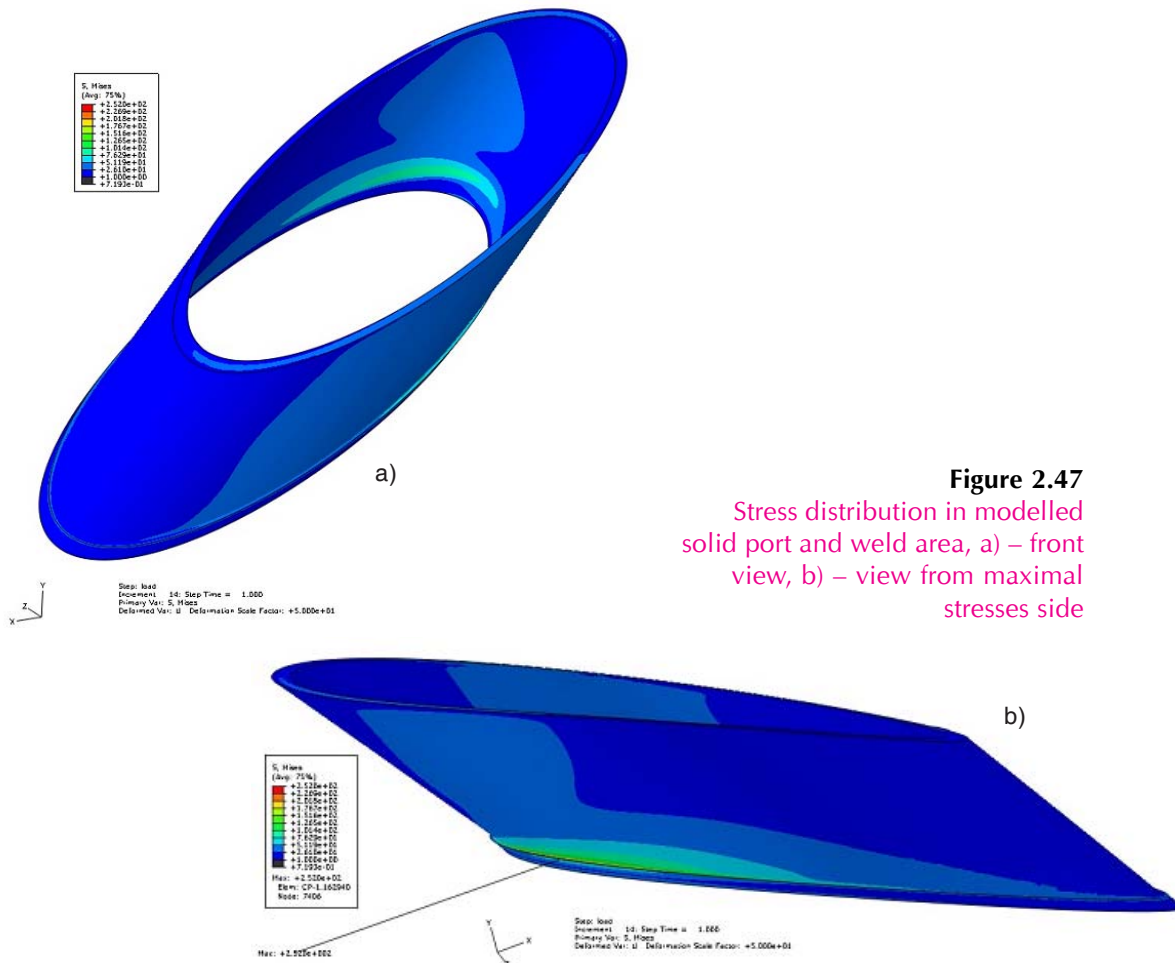
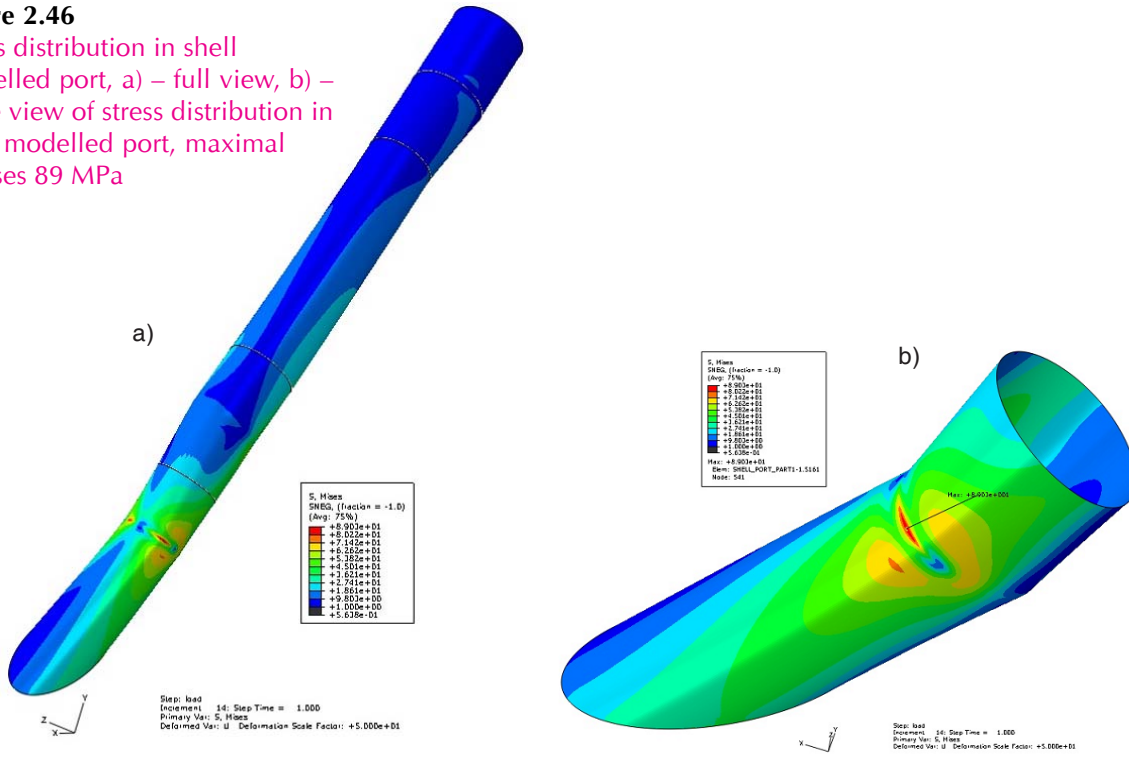


Figure 2.47
Stress distribution in modelled solid port and weld area, a) – front view, b) – view from maximal stresses side

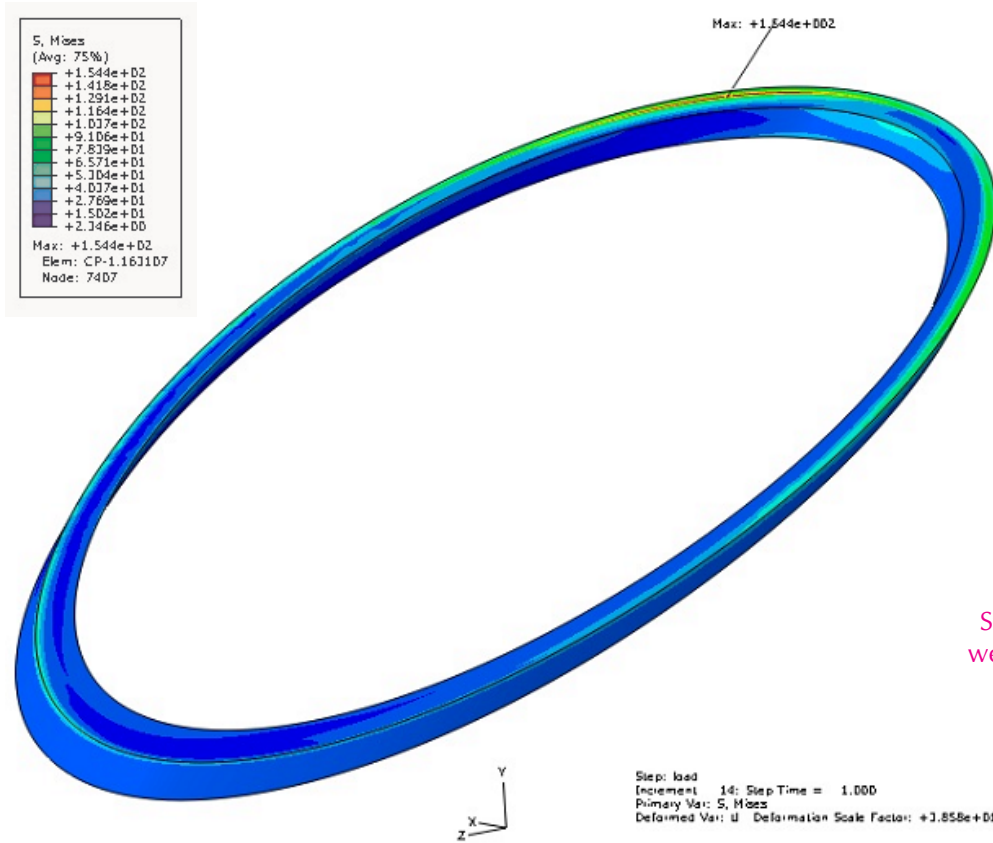


Figure 2.48
Stress distribution in weld, maximal stress 154 MPa

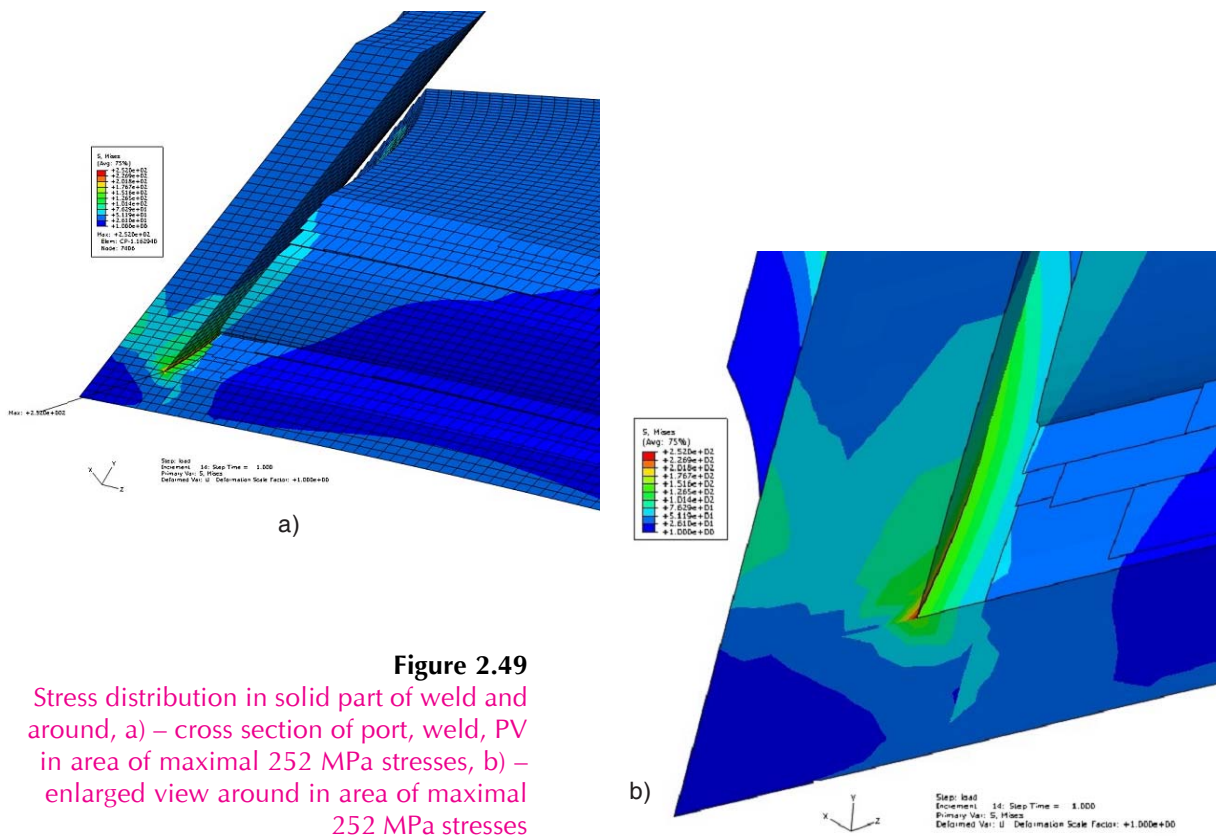


Figure 2.49
Stress distribution in solid part of weld and around, a) – cross section of port, weld, PV in area of maximal 252 MPa stresses, b) – enlarged view around in area of maximal 252 MPa stresses

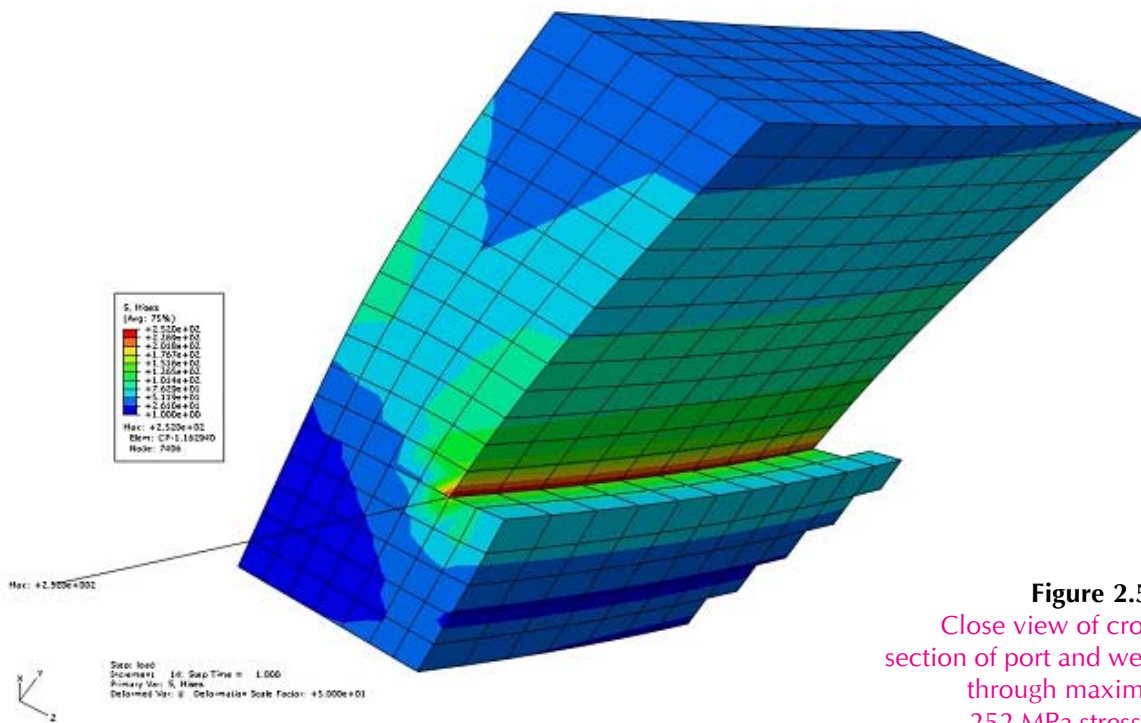


Figure 2.50
Close view of cross section of port and weld through maximal 252 MPa stresses

2.3.5.3 Analysis of stress in the welding between Plasma Vessel and ports AEK20 with gap 1 mm

Stress distributions in model of the welding between Plasma Vessel and ports AEK20 with gap 1mm are presented in Figure 2.51.

In the shell part of plasma vessel maximal Von Mises stresses are 65 MPa (Figure 2.52). In the shell part of port maximal Von Mises stresses are 112 MPa (Figure 2.53).

Main interest is welded zone of port and PV, modelled as 3D solid (Figure 2.54 - Figure 2.59). Maximal obtained stress level is 507 MPa (Figure 2.58, Figure 2.59), on the wall of port, close to the edge of weld tip (Figure 2.56). In bend of weld maximal stress level is 325 MPa (Figure 2.57).

According analysis results it was received that the stresses in port and vessel is below yield strength which is 320 MPa. The stresses in welded zone of port and PV in surface of some distorted element exceed the yield strength (for weld material 272 MPa), but average value of stresses are below the yield strength. The distorted element was received due to complexity of geometry of analysed structure. The influence of these distorted elements to stress condition of all structure is minor.

Therefore the stability of the welding between Plasma Vessel and ports AEK20 with gap 1mm will be sustained at used loading for analysis.

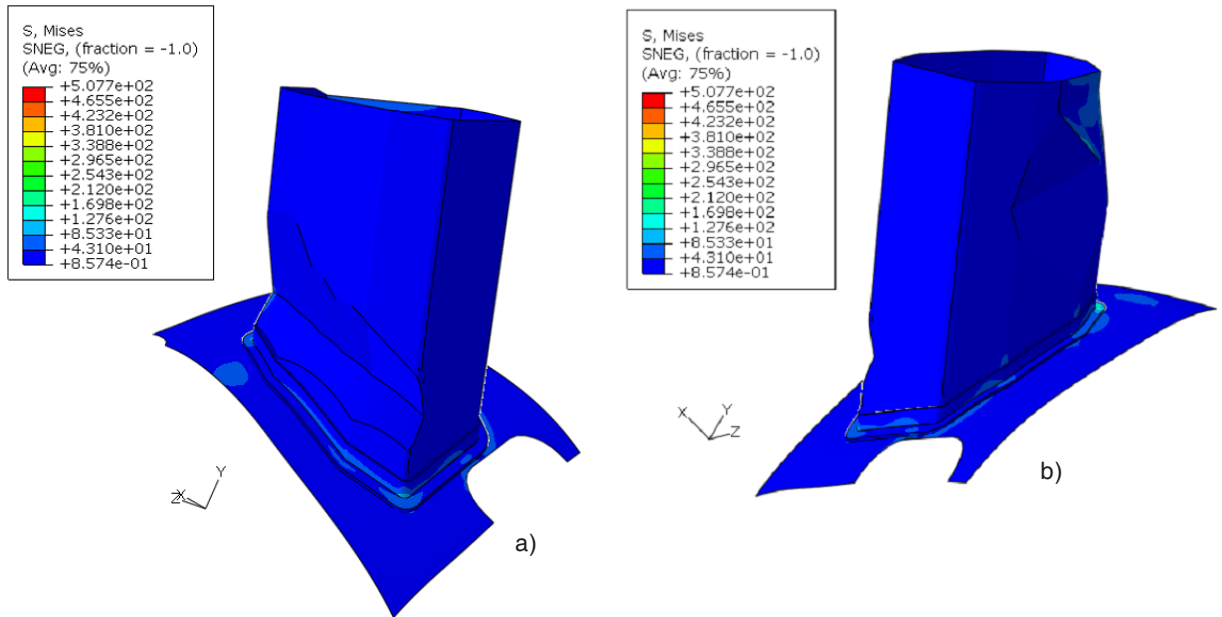


Figure 2.51
Stress distribution in full model, a) – right view, b) – front view, c) – left view

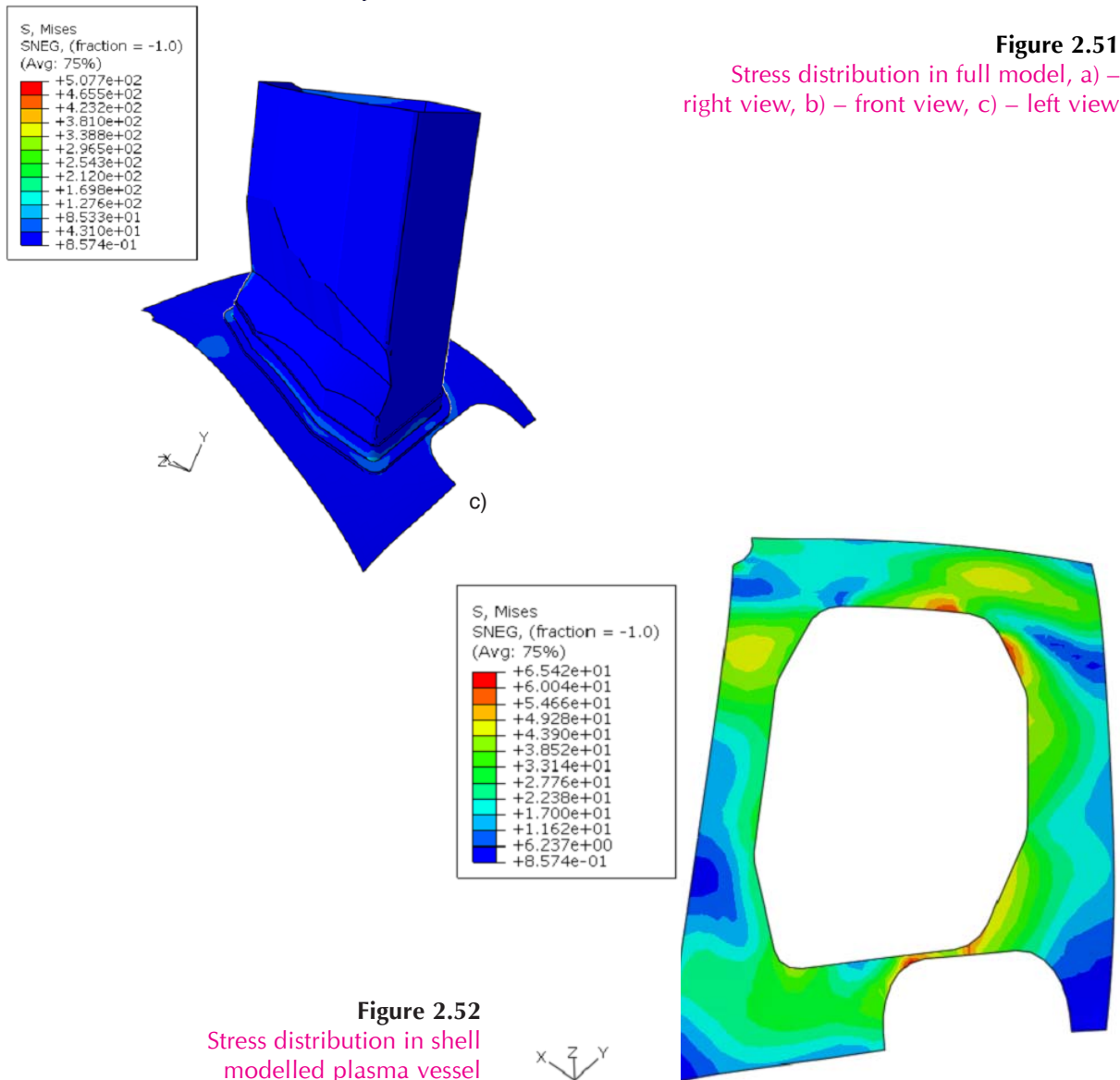


Figure 2.52
Stress distribution in shell modelled plasma vessel

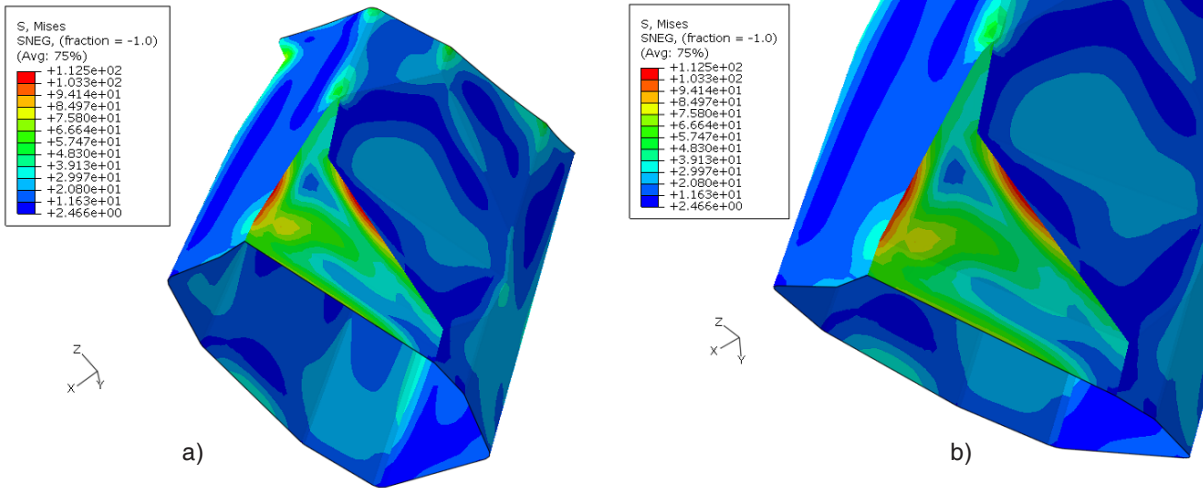


Figure 2.53
Stress distribution in shell modelled port, a) – full view, b) – enlarged view around maximal stresses 112 MPa

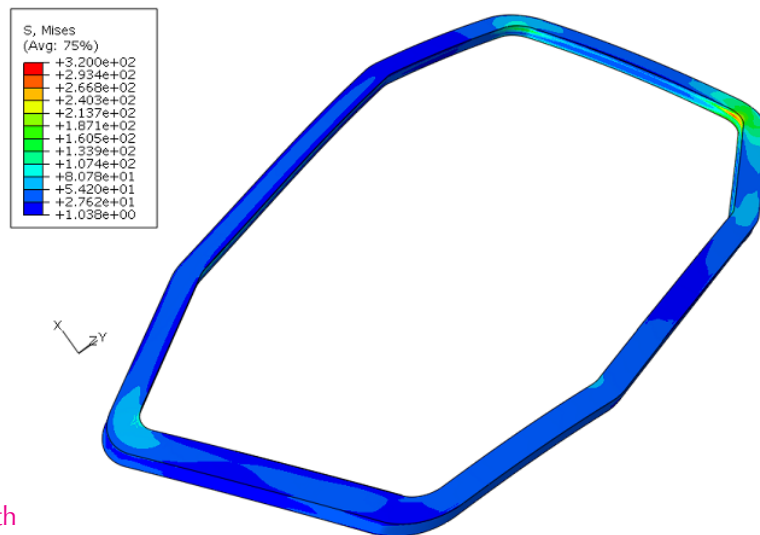


Figure 2.54
Stress distribution in modelled solid Plasma Vessel, upper stress limit set to 320 MPa yield strength

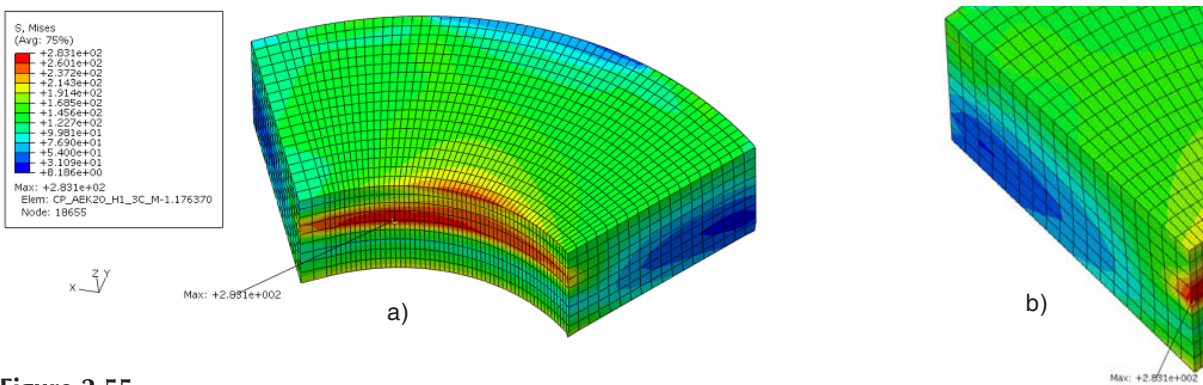


Figure 2.55
Stress distribution in modelled solid Plasma Vessel area, a) – view from maximal stresses side, b) – in area of maximal 283 MPa stresses

Figure 2.56
Stress distribution in weld, maximal stress 507 MPa

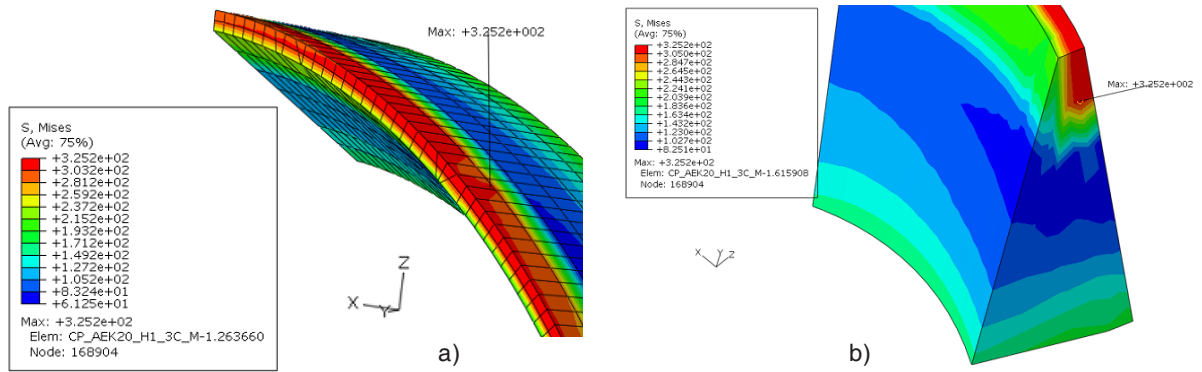
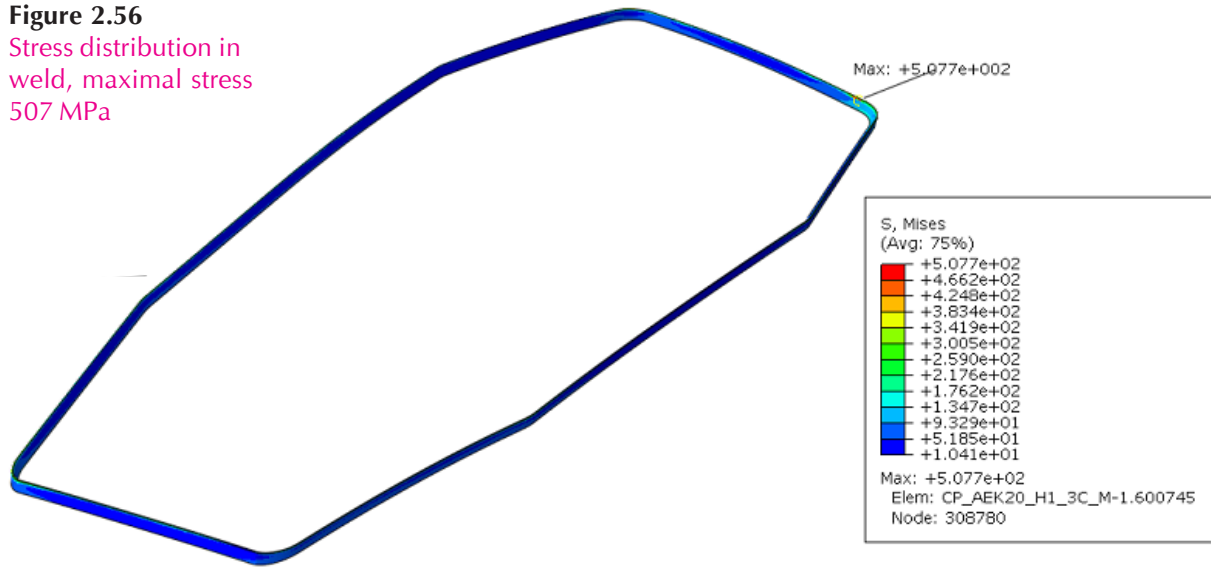


Figure 2.57
Stress distribution in part of weld, a) – close view of weld, in area of maximal 325 MPa stresses, b) – enlarged view around a maximal 325 MPa stresses

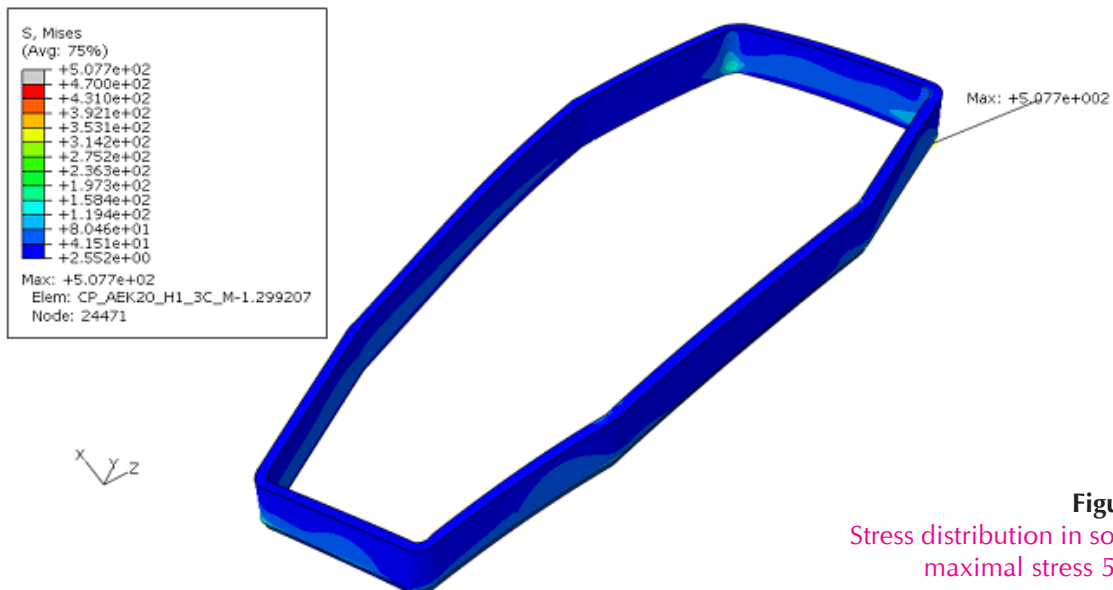


Figure 2.58
Stress distribution in solid port, maximal stress 507 MPa

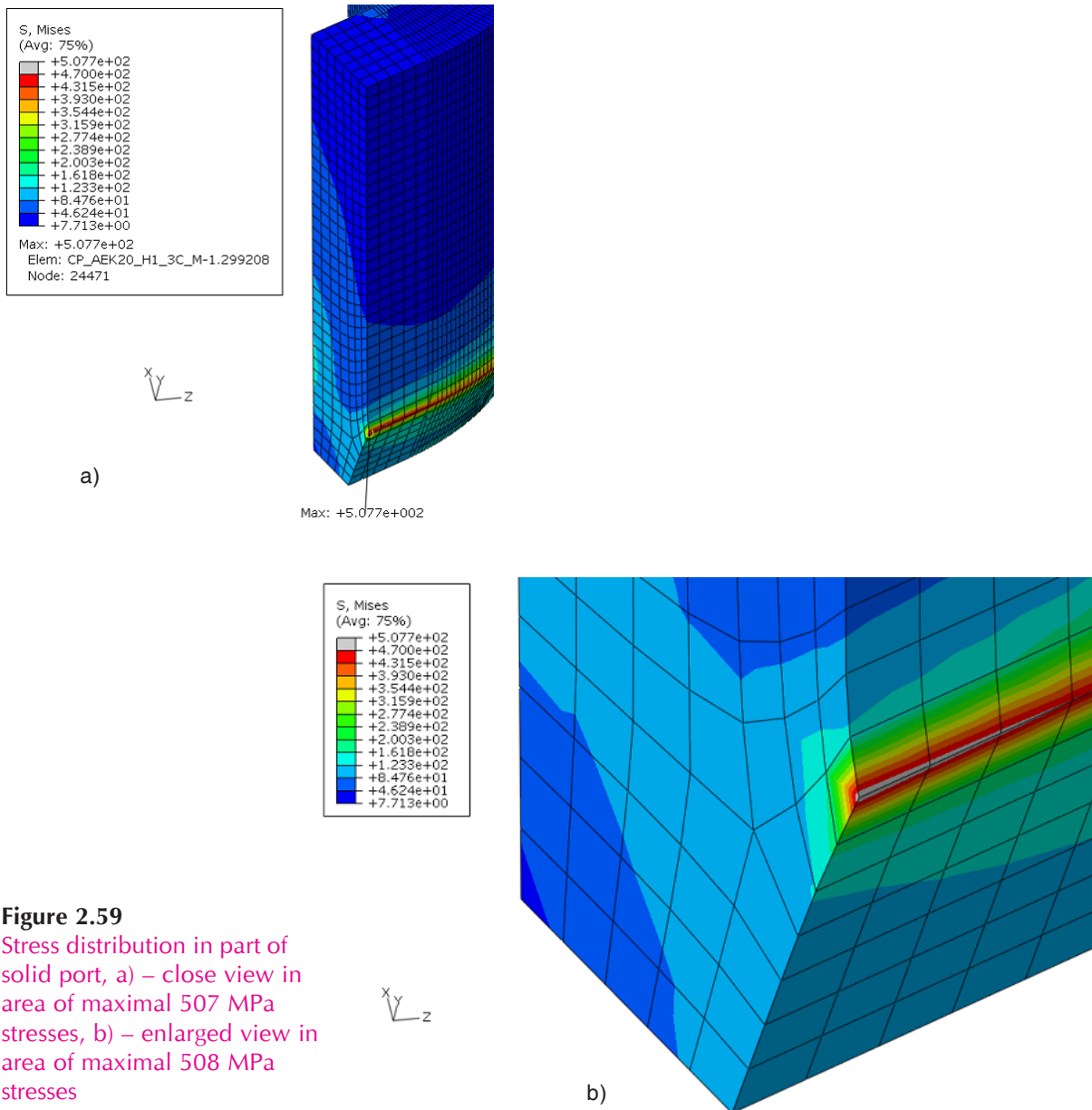


Figure 2.59
Stress distribution in part of solid port, a) – close view in area of maximal 507 MPa stresses, b) – enlarged view in area of maximal 508 MPa stresses

3 INVESTIGATION OF SPECTROSCOPIC CHARACTERISTICS OF HIGHLY CHARGED IONS OF TUNGSTEN

Tungsten as a heat-resistant material is planned to use while building a new fusion reactor within ITER project. Using tungsten in some parts of the tokamak may solve the tritium retention problem. On the other hand, tungsten atoms can detach from the inner walls of the fusion reactor, penetrate into the plasma and be ionised to very high degrees. Various tungsten ions will irradiate strongly thus cooling the plasma. Seeking to take into account an influence of the tungsten ions on the properties of the thermonuclear plasma it is necessary to accumulate a large amount of information on spectral characteristics of tungsten ions in databases. Owing to all mentioned the theoretical investigations play an important role.

3.1 Quasirelativistic treatment of spectral characteristics of W^{37+} , W^{36+} and W^{35+}

The possibility to employ the quasirelativistic approach [8-11] for calculations of energy spectra, characteristics of electric transitions and radiative lifetimes of W^{37+} , W^{36+} and W^{35+} ions is investigated. The ground configurations of these ions contain an open $4d^N$ -shell ($N=1, 2$ and 3), and two first excited configurations $4p^54d^{N+1}$ and $4p^64d^{N-1}4f$ are strongly mixed.

The calculations of energy spectra of tungsten ions have been performed employing the quasirelativistic approach described in [8-11]. In order to obtain reliable data the calculations of the energy spectra of W^{37+} were performed many times taking into account the correlation effects increasingly. In Table 3.1 the results of the calculations are presented for those levels with existing experimental data. The notations of levels, their total momenta, and the experimental energy values from [12] are put in the first three columns. Further in the table the theoretical energy values calculated within different approximations are presented. In the last column we put the notations of the levels obtained within LS-coupling employed in theoretical calculations. For simplicity of comparison the mean square deviations (MSD) of the theoretical data from the experimental ones for the whole energy spectrum presented are shown in the last row of the table.

The simplest approximation used, denoted 0 in Table 3.1, is the single-configuration approximations when the spectra of the ground $4p^64d$ and excited configurations $4p^54d^2$ and $4p^64f$ are calculated independently from one another. Naturally this approximation is the roughest one.

It is known [12] that the excited configurations $4p^54d^2$ and $4p^64f$ are close energetically and mixed strongly. Therefore the following approximation applied within the research (denoted A) is the one where the interaction of the mentioned two configurations is taken into account. The same approximation has been used in the research [13] for calculations of the energy spectra of highly charged tungsten ions of configurations $4p^64d^N$, $4p^54d^{N+1}$ and $4p^64d^{N-1}4f$ (with N from 1 to 9). In the paper it has been shown that the quasirelativistic approach allows one to take into account the relativistic effects well enough. Thus it is necessary to take into account the correlation effects in order to improve the accuracy of the spectra. Naturally, the mentioned approximation influences mainly the position of the levels of terms with the total momenta same as of 2F since the $4p^64f$ configuration has only one this term. It can be clearly seen from the changes of the energy values of the levels of mentioned configuration. At the same time the

energy values of levels with the total momenta 0.5 and 1.5 (i.e. the total momenta absent in 2F) do not change at all. As a result MSD examined decreases by 15% approximately.

Table 3.1 Energy spectra of W^{37+} (a.u.) See the text for explanation

<i>Term [12]</i>	<i>J</i>	<i>Exp. [12]</i>	<i>O</i>	<i>A</i>	<i>B</i>	<i>C</i>	<i>D</i>	<i>E</i>	<i>F</i>	<i>Theor. term</i>
$4p^64d\ {}^2D$	3/2	0	0	0	0	0	0	0	0	$4p^64d\ {}^2D$
$4p^64d\ {}^2D$	5/2	154640	153600	153600	154100	154000	153800	153800	153800	$4p^64d\ {}^2D$
$4p^54d^2\ (3F)\ (3/2,2)$	1/2	1227640	1224000	1224000	1238300	1230700	1231200	1230600	1231200	$4p^54d^2\ ({}^3F)\ {}^4D$
$4p^54d^2\ (3F)\ (3/2,2)$	3/2	1227640	1224200	1224200	1238400	1230800	1231100	1230500	1231100	$4p^54d^2\ ({}^3F)\ {}^4D$
$4p^54d^2\ (1G)\ (3/2,4)$	5/2	1508470	1558900	1519800	1529800	1525000	1522000	1522000	1522000	$4p^54d^2\ ({}^1G)\ {}^2F$
$4p^54d^2\ (3F)\ (3/2,3)$	3/2	1542600	1569200	1569200	1571900	1563800	1561800	1561800	1561800	$4p^54d^2\ ({}^3F)\ {}^4F$
$4p^54d^2\ (3F)\ (3/2,4)$	5/2	1731460	1769700	1766600	1763300	1756900	1753500	1753800	1753500	$4p^54d^2\ ({}^3F)\ {}^2D$
$4p^64f\ {}^2F$	5/2	1758100	1710500	1783400	1784000	1780300	1775200	1775900	1775200	$4p^64f\ {}^2F$
$4p^64f\ {}^2F$	7/2	1769600	1751200	1794700	1796900	1794300	1788900	1789700	1788900	$4p^64f\ {}^2F$
$4p^54d^2\ (3F)\ (1/2,2)$	5/2	2014500	2020600	2042600	2041300	2035800	2031900	2032800	2031900	$4p^54d^2\ ({}^3F)\ {}^4G$
$4p^54d^2\ (1D)\ (1/2,2)$	3/2	2184310	2231600	2231600	2219900	2211700	2206900	2207900	2206900	$4p^54d^2\ ({}^3F)\ {}^2D$
$4p^54d^2\ (1G)\ (1/2,4)$	7/2	2325500	2323600	2346600	2341700	2333100	2327400	2328700	2327400	$4p^54d^2\ ({}^1G)\ {}^2F$
		MSD	28600	24100	23200	18300	18200	15300	14900	

While taking into account the correlation effects in highly charged ions the quasidegenerate configurations play a significant role, i.e. the ones obtained from the configurations under research by virtual excitations not changing the principal quantum number of an electron. Here usual single-configuration radial orbitals, the quasirelativistic ones in this case, are suitable enough to describe the virtually excited electrons. Within the approximation denoted B a set of three quasidegenerate configurations $4p^44d^3$, $4p^54d4f$ and $4p^44d4f^2$ was taken into account for the adjusted configuration $4p^64d$ and a set of four admixed configurations $4p^44d^24f$, $4p^34d^4$, $4p^54f^2$ and $4p^34d^24f^2$ was used for the configurations $4p^54d^2$ and $4p^64f$. As seen from the table this approximation influences the energy values of all levels of the investigated configurations. However MSD decreases not as essentially as one may hope.

Further improvement of the accuracy is related to the polarisation of 4s-shell. For this purpose the set of the quasidegenerate configurations used before was supplemented with the quasidegenerate configurations obtained by excitations of 4s-electrons. Owing to that the number of the admixed configurations for the ground one increased to 8, and for the excited ones – to 12. The results of these calculations denoted C. The obtained results reveal that it is extremely important to take into account the polarisation of 4s-shell that allows to improve significantly an accuracy of the theoretical data. At the same time the trial calculations showed that the polarisation of 3d-shell does not noticeably influence the spectra of the explored configurations. Thus this kind of the correlation effects was not taken into account.

Next step in getting more accurate data is attributed to the excitations of the electrons to the virtual states with the principal quantum number $n > 4$. The transformed radial orbitals were employed to describe these electrons [11, 14]. The transformed radial orbitals were obtained for the principal quantum numbers 5, 6, and 7 and all possible values of the orbital quantum number l . Thus the number of the radial orbitals was increased by 18. New admixed configurations were obtained from the adjusted ones by one- and two-electron virtual excitations of the electrons with $n = 4$. In this basis the total number of the admixed configurations equals to 363 for the

4p⁶4d configuration, 488 – for the 4p⁵4d² configuration, and 379 – for the 4p⁶4f one. However only a small part of the last two sets of odd admixed configurations coincide and the total number of terms within is about 900000. Though the total number of terms can be reduced to 670000 approximately using the methods described in [15], this number is still very large. Thus it is necessary to select the most important admixed configurations as described earlier.

Several calculations have been performed decreasing gradually the selection parameter of the admixed configurations S from 10^{-4} till 10^{-7} . Within the approximation **D** ($S = 10^{-4}$) 5 most important even admixed configurations and 6 odd ones were added. However it had almost no influence on the accuracy of the results obtained. The total number of the mixing even configurations K_{even} reached 35 and of the odd ones $K_{\text{odd}} = 65$ when the selection parameter is decreased to 10^{-5} (approximation **E**). Within the approximation the energy values of the investigated levels were obtained more precisely and the MSD decreased. Further reduction of the selection parameter (approximation **F** – $S = 10^{-6}$, $K_{\text{even}} = 104$, $K_{\text{odd}} = 217$) ceased to influence essentially the energy of the investigated terms.

The calculations performed enable one to check the reliability and effectiveness of the applied method of evaluation of the influence of admixed configurations. For this purpose the mean weights of the admixed configurations K within the wavefunctions of the adjusted configuration K_0 were evaluated using the eigenfunctions obtained while diagonalizing the energy matrix

$$\overline{W}(K_0, K) = \sum_{L_0 S_0 J_0} \sum_{LSJ} (2J+1) a^2(K_0 L_0 S_0 J_0, KLSJ) / Q(K_0).$$

Here $a(K_0 L_0 S_0 J_0, KLSJ)$ are eigenfunction expansion coefficients, and $Q(K_0)$ – statistic weight of the adjusted configuration. In Table 3.2 these weights are compared with the weights of the admixed configurations $W_{\text{PT}}(K_0 K)$ obtained within the second order perturbation theory:

$$W_{\text{PT}}(K_0, K) = \frac{\sum_{T_0 L_0 S_0 T} (2L+1)(2S+1) \langle K_0 T_0 L_0 S_0 || H || K T L S \rangle^2}{g(K_0) (\overline{E}(K) - \overline{E}(K_0))^2}.$$

The even configuration within **E** approximation was chosen as an example. The admixed configurations are presented in the second column, and their way of obtaining is put in the third column (one-electron excitations – 1el, excitations of the pair of equivalent electrons into two equivalent electrons – 2eq, other two-electron excitations – 2el). The configurations in the table are sorted as their weights $\overline{W}(K_0, K)$ decrease. These weights are presented in the fourth column of the table. In the next column the values of the weights obtained within the second order perturbation theory are shown. The last column contains the ordinal numbers of the configurations in accordance with decrease of their weight $W_{\text{PT}}(K_0 K)$.

As seen from the table the first six most important admixed configurations are the quasidegenerate ones in relation to the adjusted configuration. Thus these configurations must be taken into account in the first place as stated in the beginning of the section. Three of six configurations mentioned are related with excitations from 4s-shell. There are 15 configurations of last type totally in the case under investigation, i.e. they make almost a half of all admixed configurations. This fact confirms an importance of taking into account this shell polarization while calculating the correlation effects. The comparison of the values $\overline{W}(K_0, K)$ and $W_{\text{PT}}(K_0 K)$ show that they are in good agreement with one another. The deviations for majority of coefficients do not exceed 10%. Naturally, the disagreement increases toward the end of the table, i.e. for the configurations making smaller contributions to the correlation effects. It is due to the fact that the interactions between the admixed configurations are not taken into account in the second order perturbation theory.

Table 3.2. Mean weights of the admixed configurations K within the wavefunctions of the adjusted configuration K_0 of W^{37+} within E approximation

No	Configuration	Exit.	$\overline{W}(K_0, K)$	$W_{PT}(K_0, K)$	No_{PT}
1	4s ² 4p ⁶ 4d		9.84E-01	1.00E+00	1
2	4s ² 4p ⁴ 4d ³	2eq	9.40E-03	1.03E-02	2
3	4s ² 4p ⁵ 4d 4f	1el	3.60E-03	4.02E-03	3
4	4s 4p ⁵ 4d ² 4f	2el	1.05E-03	9.57E-04	4
5	4s ² 4p ⁴ 4d 4f ²	2eq	7.14E-04	7.99E-04	5
6	4s 4p ⁶ 4d ²	1el	3.19E-04	3.37E-04	6
7	4p ⁶ 4d ³	2eq	1.97E-04	2.31E-04	7
8	4s ² 4p ⁴ 4d ² 5g	2el	1.64E-04	1.41E-04	8
9	4s ² 4p ⁴ 4d 5p ²	2eq	1.20E-04	1.29E-04	9
10	4s ² 4p ⁵ 4f 5g	2el	1.03E-04	1.02E-04	10
11	4s 4p ⁵ 4d 4f 5g	2el	8.72E-05	1.02E-04	11
12	4s 4p ⁵ 4d 5s 5p	2el	7.52E-05	7.83E-05	12
13	4s ² 4p ⁵ 5p 6d	2el	6.08E-05	6.57E-05	13
14	4s 4p ⁶ 4d 5g	1el	6.06E-05	5.68E-05	17
15	4s ² 4p ⁵ 4d 5f	1el	5.41E-05	5.90E-05	15
16	4s ² 4p ⁵ 4d 5p	1el	5.22E-05	6.14E-05	14
17	4s 4p ⁵ 4d ² 5f	2el	5.16E-05	4.80E-05	19
18	4s ² 4p ⁴ 4d 4f 5f	2el	5.04E-05	5.59E-05	18
19	4s ² 4p ⁴ 4d 5g ²	2eq	4.79E-05	5.70E-05	16
20	4s 4p ⁶ 4f ²	2el	4.75E-05	2.73E-05	23
21	4s ² 4p ⁴ 4d 4f 6h	2el	3.05E-05	3.04E-05	22
22	4p ⁶ 4d 4f ²	2eq	2.95E-05	4.61E-05	20
23	4s ² 4p ⁴ 4d ² 5d	2el	2.55E-05	3.07E-05	21
24	4s ² 4p ⁵ 4d 6h	1el	2.09E-05	1.89E-05	25
25	4s 4p ⁵ 4d 5g 6h	2el	2.06E-05	2.27E-05	24
26	4s 4p ⁶ 5s 6d	2el	1.68E-05	1.80E-05	26
27	4s 4p ⁶ 4d 5s	1el	1.50E-05	1.46E-05	29
28	4s 4p ⁵ 4d 5p 6d	2el	1.29E-05	1.35E-05	31
29	4s ² 4p ⁵ 5g 6h	2el	1.24E-05	1.49E-05	28
30	4s ² 4p ⁴ 4d 6d ²	2eq	1.20E-05	1.52E-05	27
31	4s 4p ⁵ 4d 5f 5g	2el	1.15E-05	1.24E-05	32
32	4s ² 4p ⁴ 4d 6h ²	2eq	1.14E-05	1.38E-05	30
33	4s ² 4p ⁴ 4d 5s 6d	2el	1.02E-05	1.09E-05	33
34	4s 4p ⁵ 4d ² 6p	2el	8.78E-06	1.02E-05	35
35	4s ² 4p ⁴ 4d 5p 6p	2el	2.57E-07	1.06E-05	34

The analysis of the admixed configurations selected reveals that the excitations into the state with large values of the orbital quantum number l prevail as one may expect. Here the most important configurations are the ones containing virtual excitations with the principal quantum number $n=5$. The configurations with virtual excitations containing states $n = 6$ appear after

them. Although the basis of the radial orbitals used contains the functions with $n = 7$, they do not appear in the set investigated as the theoretical weights of the corresponding admixed configurations are $<10^{-5}$. These properties of the admixed configurations are induced by the fact that the transformed radial orbitals are generated in ascending order of the principal quantum number. Thus, the transformed radial orbitals employed to describe the virtual excitations allow one to take into account the correlation effects rather effectively already for the small values of the principal quantum number. The application of these radial orbitals does not require a creation of the large basis sets.

Table 3.3. Radiative lifetimes of W^{37+} obtained using the electric dipole transitions (ns)

<i>Level [12]</i>	<i>J</i>	<i>O</i>	<i>A</i>	<i>B</i>	<i>C</i>	<i>D</i>	<i>E</i>	<i>F</i>
4p⁵4d² (³F) ⁴D	1/2	2.55E-01	2.55E-01	2.55E-01	2.51E-01	2.46E-01	2.54E-01	2.48E-01
4p⁵4d² (³F) ⁴D	3/2	8.15E-01	8.15E-01	8.65E-01	8.30E-01	8.17E-01	8.41E-01	8.24E-01
4p⁵4d² (¹G) ²F	5/2	7.59E-01	6.69E-03	6.64E-03	6.44E-03	6.63E-03	6.65E-03	6.59E-03
4p⁵4d² (³F) ⁴F	3/2	1.91E-03	1.91E-03	2.16E-03	2.22E-03	2.20E-03	2.17E-03	2.21E-03
4p⁵4d² (³F) ²D	5/2	1.09E-03	8.86E-04	9.98E-04	1.06E-03	1.03E-03	1.03E-03	1.04E-03
4p⁶4f ²F	5/2	1.70E-03	1.03E-03	1.21E-03	1.21E-03	1.22E-03	1.20E-03	1.21E-03
4p⁶4f ²F	7/2	2.05E-03	1.48E-03	1.71E-03	1.76E-03	1.73E-03	1.72E-03	1.74E-03
4p⁵4d² (³F) ⁴G	5/2	1.26E-03	6.62E-04	8.87E-04	8.61E-04	8.68E-04	8.69E-04	8.74E-04
4p⁵4d² (³F) ²D	3/2	2.39E-04	2.39E-04	2.98E-04	3.00E-04	2.99E-04	3.03E-04	3.00E-04
4p⁵4d² (¹G) ²F	7/2	6.08E-04	3.85E-04	5.17E-04	5.05E-04	5.09E-04	5.17E-04	5.09E-04

Not only the energy spectra but also the characteristics of the electric transitions can be improved by taking the correlation effects into account. Table 3.3 contains the radiative lifetimes obtained using the electric dipole transitions for the levels of the excited configurations presented in the Table 3.1. As seen from the table the transfer from the approximation 0 to the approximation A has a significant influence on the radiative lifetimes of the levels of 4p⁶4f configuration. It is due to the mentioned strong interaction of this configuration with the configuration 4p⁵4d². Within the approximation A an averaged weight of the configuration 4p⁵4d² into the eigenfunctions of the configuration 4p⁶4f equals $\overline{W}(K_0, K) = 0.447$, i.e. it makes almost one half. The opposite effect is significantly smaller, as the configuration 4p⁵4d² contains much larger number of terms. At the same time an influence of the configuration 4p⁶4f on some levels of the configuration 4p⁵4d² is very strong. It is clearly seen in the case of the lifetime of the level 4p⁵4d² (³F) ⁴G_{5/2} which decreases approximately two times when transiting to the approximation A. The transition to the approximation B changes the lifetimes of the levels as well. Further improvement of the eigenfunctions has little influence on the lifetimes as the lifetimes are mainly determined by the strong allowed transitions. At the same time it may influence significantly the values of the intercombination transitions.

The performed explicit investigation of W^{37+} spectra and analysis of the results enabled us to decide immediately on the optimal approximation for the investigations of the spectral characteristics of W^{36+} and W^{35+} . In Table 3.4 there are the experimental (from paper [12]) and theoretical (within the approximation D) energy spectra of the ground configuration 4d² of W^{36+} .

The same data for the ground configuration 4d³ of W^{35+} is presented in the Table 3.5. The energy values obtained in [12] using the semiempirical fitting of the parameters are shown in square brackets. As seen from the Table 3.4 the theoretical data are in rather good agreement with the experimental results for the configuration 4d² and the relative errors do not exceed 2%.

Unfortunately, there are no reliable experimental data for energy spectra of the excited configurations. The theoretical data for the configuration $4d^3$ obtained within the approximation D are of the same accuracy. Herewith the correct order of all levels is obtained in both cases contrary to what it is within the approximation A. As seen from the data obtained for W^{37+} increasing of the basis used can improve the accuracy of the results. However the present accuracy allows one to use the obtained data for calculations of transition characteristics and other physical values.

Table 3.4. Energy spectra of $4d^2$ configuration of W^{36+} (a.u.)

<i>Level [12]</i>	<i>Exp. [12]</i>	<i>D</i>
3F_2	0	0
3P_0	67780	66600
3F_3	141310	140400
3P_2	174130	170700
3P_1	184610	181800
1G_4	182760	1823000
3F_4	308530	3077800
1D_2	331480	327900
1S_0	[407000]	405100

Table 3.5. Energy spectra of $4d^3$ configuration of W^{35+} (a.u.)

<i>Level [12]</i>	<i>Exp. [12]</i>	<i>D</i>
$^4F_{3/2}$	0	0
$^4F_{5/2}$	121554	120623
$^2P_{3/2}$	140750	141003
$^2G_{7/2}$	156410	154576
$^4P_{1/2}$	160690	157388
$^2H_{9/2}$	[159500]	158194
$^4P_{5/2}$	[225900]	222413
$^4F_{7/2}$	273250	272804
$^4F_{9/2}$	288570	286019
$^4P_{3/2}$	299520	299063
$^2P_{1/2}$	312200	308020
$^2F_{5/2}$	318120	315784
$^2H_{11/2}$	322010	318778
$^2D_{5/2}$	[344000]	338537
$^2F_{7/2}$	[350000]	346448
$^2D_{3/2}$	402410	397953
$^2G_{9/2}$	[438000]	435517
$^2D_{3/2}$	[485000]	476714
$^2D_{1/2}$	[516000]	509960

Presented calculations revealed that the developed quasirelativistic approach can be successfully applied for theoretical investigation of highly charged ions of heavy atoms. The obtained results (energy spectra, characteristics of electric transitions, radiative lifetimes) for W^{37+} , W^{36+} , and W^{35+} can be used for modelling of the high temperature thermonuclear plasma.

3.2 Calculation of fluorescence yields, Auger transition probabilities and natural level widths for the states of multiple ions of tungsten with vacancies in the $4l$ ($l = 0-3$) shells

Radiative and nonradiative decay of excited states are tightly related competitive processes. At the production of vacancies in the outer shells namely nonradiative Auger transitions (when they are possible energetically) determine the total deexcitation rate and natural width of levels. The fluorescence yield equal to the ratio of the radiative rate and the total decay rate presents the general characteristic of radiative decay. The Auger widths of levels are necessary for the calculation of line intensities in the emission spectrum.

At the conditions in the plasma of tokamak devices the vacancies in several outer shells of tungsten ions can be effectively produced [16]. We considered the Auger transitions in the low and middle charged tungsten ions from the initial states with vacancies in the $4s$, $4p_{1/2}$, $4p_{3/2}$, $4d_{3/2}$, $4d_{5/2}$ subshells and $4f$ shell. The calculations have been performed in the quasirelativistic approximation [17], which is widely used for the investigation of spectral characteristics of tungsten ions [18, 19].

The most probable Auger transitions are the Coster-Kronig (CK) and super-Coster-Kronig (sCK) transitions, when two or three subshells with the same principle quantum number are involved. Such transitions proceed between neighbouring and even overlapping configurations. Thus it is necessary to take into account in calculations the dependence of probabilities of such transitions on the energy of escaping electron as well as the energetic impossibility of some transitions between two overlapping configurations.

Experimental N shell fluorescence yields for ions of tungsten are not available owing to the complexity of their registration. The natural widths of such states are measured only for single ions [20]. Our values of natural width for W^+ correspond better to the experimental values than the ones given in [21] calculated by Dirac-Fock-Slater method.

The decay of vacancy states in $4l$ subshells is dominated by nonradiative transitions, and the fluorescence yield ω is of order $10^{-5} - 10^{-2}$. Its values changes slowly in the intervals of ionization stages, when all CK and sCK transitions remain energetically possible. At partial overlap of initial and final configurations such behaviour of ω is changed by its rapid increase and even by sudden jump at the end of possible ionization stages when all main Auger transitions become partially forbidden.

We have determined the intervals of ionization degrees in which the CK and sCK transitions for the states with $4l^{-1}$ vacancy are possible or partially possible. At small ionization degrees various CK and sCK transitions are permitted and the Auger width as well as equal to it natural width obtains a rather large value; for $4s^{-1}$, $4p^{-1}$ and $4d^{-1}$ states it amounts several eV and even more than 10 eV (Figure 3.1). At ionization stages $q = 8-12$ the sudden decrease of Auger width takes place due to energetic interdiction of the most such transitions.

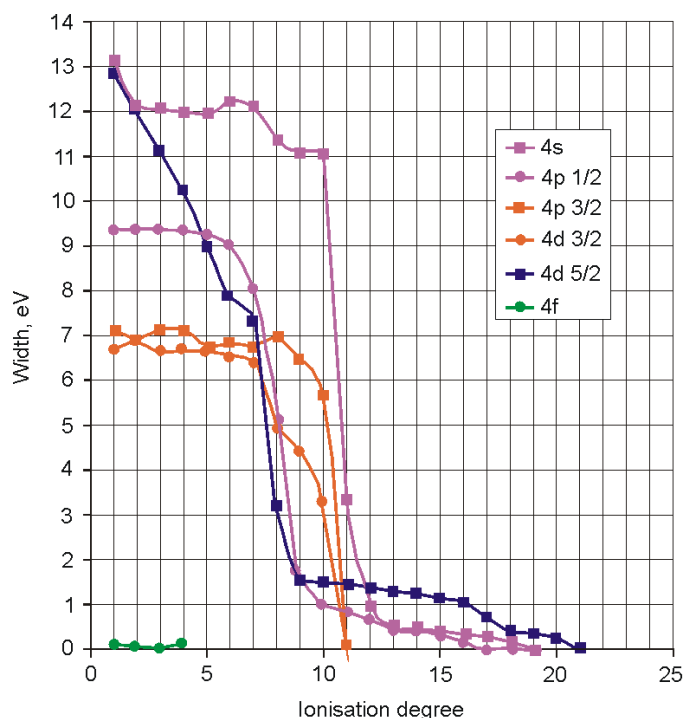


Figure 3.1
Auger widths for ions of tungsten with vacancies in the 4s, 4p, 4d or 4f shells

3.3 Calculations of radiative transition spectra in the regions of 4–7 nm and 12–14 nm for W^{40+} – W^{45+}

In tokamak plasma tungsten ions radiate very strongly between 4 and 7 nm. Structured quasicontinuum band is formed by lines from different ionization states. It is impossible to assess the contribution from separate ionization stages to the whole spectrum because the emission that is observed from the tokamak plasma is integrated along the line of sight of the spectrometer. EBIT measurements showed that some part of radiation comes from configurations with valence 4d electrons. Resonance transitions of the type $4d^{N'} \rightarrow 4d^{N-1}4f$ and $4d^{N'} \rightarrow 4p^5 4d^{N+1}$ ($N=1, \dots, 9$) have been previously investigated by many groups [22–24]. Additionally, extensive theoretical study [25, 26] showed that emission spectra calculated by taking into account radiative decay after excitation from ground level agree quite well with the EBIT data. It can serve as the first tool for assessing main configurations and transitions in the plasma. The advantage of the approach is that the rough population of excited levels can be obtained having only radiative transition probabilities. However discrepancies between experimental data and theoretical calculations for wavelengths of $4d^{N'} \rightarrow 4d^{N-1}4f + 4p^5 4d^{N+1}$ transitions were beyond the error bars. The deviations equal to about 0.1–0.2 nm. Further theoretical investigation using extended configuration interaction (CI) basis obtained from configuration interaction strength allowed to reach agreement with experimental wavelengths within error bars for W^{30+} ion [27]. Therefore it can be concluded that the main reason for the observed discrepancies between theoretical and experimental wavelengths is due to correlation effects omitted in the previous works which used only two excited configuration of odd parity.

The aim of the current work is to study $4d^{N'} \rightarrow 4d^{N-1}4f$ and $4d^{N'} \rightarrow 4p^5 4d^{N+1}$ transitions in W^{29+} – W^{37+} ions performing large scale calculations with extended CI bases. Admixed configurations having the largest weights to the ground $4d^N$ configurations are used from previous our work [28] where magnetic dipole transitions have been analyzed among levels of $4d^N$ configuration. In addition, admixed configurations have been found for $4d^{N-1}4f$ and $4p^5 4d^{N+1}$ configurations using the same relativistic radial wavefunctions. For this two lists of configurations which correspond to one- and two-electron excitations have been generated for both configurations and configuration

interaction strengths obtained. Calculations have been performed with different CI basis to estimate convergence of theoretical data. Figure 3.2 demonstrates convergence for some wavelengths of magnetic dipole transitions in W^{32+} when CI basis augmented in a systematic way. It can be seen that increasing CI basis from 10 to 40 configurations ensures that variation for energy level splitting is less than 0.5 \AA .

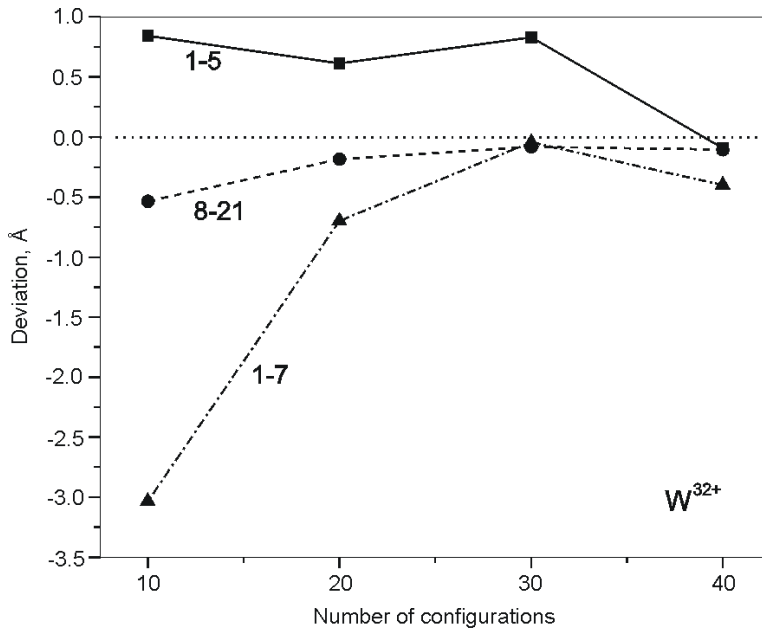


Figure 3.2
Convergence for some wavelengths of magnetic dipole transitions in W^{32+} when CI basis augmented in a systematic way

Figure 3.3 shows how changes emission spectrum obtained with 25 configurations in CI basis compared with when only 3 configurations are taken into account [25]. Emission spectra have been calculated making an assumption that the ground level is mainly populated in EBIT plasma and emission happens only after excitation from it. Larger CI basis shifts line in the spectrum from 5.17 to 5.21 nm but still discrepancy from experimental value of about 0.14 nm remains. It shows that even larger CI basis for the transitions have to be employed to obtain better agreement with experimental data.

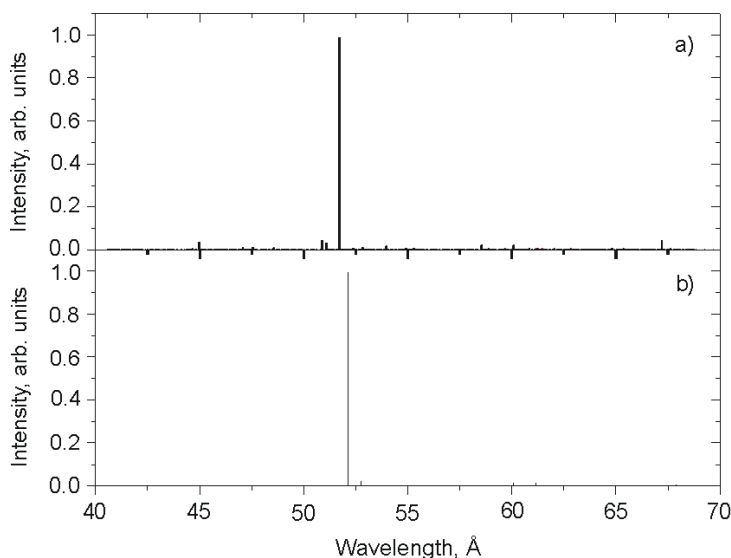


Figure 3.3
The changes of emission spectrum obtained with 25 configurations in CI basis compared with when only 3 configurations are taken into account [25]

Theoretical study of electric and magnetic dipole transitions in $W^{29+} - W^{37+}$ ions [28, 29] revealed that good agreement with experimental values for wavelengths and line intensities can be obtained only when correlation effects are properly treated.

The aim of the current work is to analyze magnetic and dipole transitions at 12–4 nm in $W^{40+} - W^{45+}$ ions using extended configuration interaction (CI) bases. The study included transitions in the levels of the ground and/or the excited configurations, namely: W^{40+} : $4s^2 4p^4$; W^{41+} : $4s^2 4p^3$; W^{42+} : $4s^2 4p^2$, $4s 4p^3$; W^{43+} : $4s^2 4p$, $4s 4p^2$; W^{44+} : $4s^2$, $4s 4p$; W^{45+} : $4s$, $4p$. The spectra of those ions were measured in EBIT plasma in the 12–14 nm range [30]. As well, spectra of the highly ionized tungsten in the region were observed in the ASDEX Upgrade tokamak in Garching, Germany [23].

The CI strength [24, 25]:

$$T(K, K') = \frac{\sum_{\gamma\gamma'} \langle K\gamma | H | K'\gamma' \rangle^2}{\bar{E}(K, K')^2} \quad (1)$$

introduced previously has been employed to find a set of the most strongly interacting configurations. The quantity in the numerator of Eq. (1) is the interconfiguration matrix element of the Hamiltonian H and $\bar{E}(K, K')^2$ is the energy distance between the interacting levels of configurations K and K' :

$$\bar{E}(K, K') = \frac{\sum_{\gamma\gamma'} (\langle K\gamma | H | K\gamma \rangle - \langle K'\gamma' | H | K'\gamma' \rangle) \langle K\gamma | H | K'\gamma' \rangle^2}{\sum_{\gamma\gamma'} \langle K\gamma | H | K'\gamma' \rangle^2} \quad (2)$$

The summation in (1) and (2) is performed over all states γ and γ' of both configurations.

The one- and two-electron excitations from the $n = 3$ complex have been included to obtain the set of configurations for which CI strengths with the above-mentioned configurations are calculated. The one electron excitations are taken up to the shells of $n = 7$ complex whereas two electron excitations include only shells up to $n = 5$ complex. About thousand of configurations are generated for every set in each ionization stage. Relativistic radial wave functions have been found for every ionization stage.

Table 3.6 presents data for wavelengths for transitions in $W^{40+} - W^{45+}$ ions. Experimental values are taken from tokamak plasma [33]. Theoretical data correspond to calculations in Dirac-Fock (GRASP code) and Dirac-Fock-Slater (FAC code) approximations. The wavelengths from FAC are presented in single-configuration approach and using extended CI bases. Values of CI strength demonstrate that correlation effects for those configurations are small and only very large CI bases would give improvement for atomic data. The extended CI basis consist of 26834 configuration state functions for W^{40+} , 18753 for W^{41+} , 53057 for W^{42+} , 66505 for W^{43+} , 28732 for W^{44+} and 30797 for W^{45+} . The extended CI bases show the best agreements with experimental values are obtained for the forbidden transitions. In this case the difference is $<0.1\%$. On the other hand, the largest discrepancies correspond to electric dipole transitions. Mainly the difference from experimental wavelengths is $>1\%$. It suggests that those experimental lines from tokamak spectra can be wrongly identified. Further theoretical studies employing other approximations than Dirac-Fock-Slater have to be carried on to clear the situation. It should be noted that our wavelengths are shorter than experimental values for all presented electric dipole transition when extended CI bases employed. The data for the single-configuration approximation from FAC have larger wavelengths than experimental ones except transition in W^{45+} .

Table 3.6. Comparison of theoretical wavelengths with experimental values. Theoretical wavelengths obtained with GRASP or FAC codes. FAC I corresponds to calculations in single-configuration approximation; FAC II – values from extended CI bases

<i>Ion</i>	<i>Type</i>	λ_{exp} [33]	GRASP [23]	FAC I	FAC II
W ⁴⁰⁺	M1	12.864	12.786	12.741	12.848
	M1	13.487	13.455	13.418	13.489
W ⁴¹⁺	M1	13.121	13.106	13.044	13.020
	M1	13.896	13.968	13.920	13.863
W ⁴²⁺	E2	12.945	12.940	12.887	12.944
	E1	12.912	13.029	12.914	12.717
	E1	13.475	13.690	13.582	13.313
	M1	13.545	13.574	13.552	13.562
W ⁴³⁺	M1	12.639	12.587	12.559	12.626
	E1	12.824	12.899	12.992	12.615
	E1	13.534	13.682	13.592	13.270
W ⁴⁴⁺	E1	13.287	13.230	13.512	13.145
W ⁴⁵⁺	E1	12.720	12.609	12.703	12.644

3.4 Calculation of the electron-impact excitation rates among the levels of 4d^N configurations for tungsten ions

Theoretical line-emission spectra of ions in plasma help to determine various plasma parameters such as its temperature T_e or density n_e . The intensity of radiation line is defined as a product of a radiative transition rate and a population of initial level. The level populations of ions in the various ionization stages are determined by solving the balance equation. Therefore reliable plasma diagnostics is in great need of accurate atomic data such as energies, radiative transition probabilities, Auger rates, electron- impact excitation rates.

Electron-impact excitation rates are obtained by averaging the total collision strengths over a distribution of electron energies. The EBIT electron beam has a very narrow energy distribution, whereas the Maxwell-distribution function is usually applied used to describe electron velocities in the tokamak plasma. The excitation rate coefficients with Maxwellian distribution for a transition from a state i to a state f at an electron temperature T_e is given by:

$$C(i \rightarrow j) = \frac{8.63 \times 10^{-6}}{g_i T_e^{1/2}} \gamma(i \rightarrow j) \exp\left(\frac{-\Delta E_{ij}}{T_e}\right) \text{cm}^3 \text{s}^{-1},$$

where $g_i = (2j_i + 1)$ is the statistical weight of the initial level i , $\Delta E_{if} = E_f - E_i$ is the excitation energy, and $\gamma(i \rightarrow j)_j$ is the effective collision strength given by

$$\gamma(i \rightarrow j) = \int_0^{\infty} \Omega(i \rightarrow j) \exp\left(\frac{-\epsilon_f}{kT_e}\right) d\epsilon_f.$$

Here $\Omega(i \rightarrow f)$ is the total collision strength for transitions between levels i and f , ϵ_f is the energy of the incident electron with respect to upper level f , T_e is the electron temperature, and k is the Boltzmann constant.

Present theoretical study includes excitation data for the energy levels of $4d^N$ ($N=1, \dots, 9$) configurations for tungsten ions ($W^{29+} - W^{37+}$). Since the accuracy of atomic data depends on the relativistic and correlation effects taken into account, our calculations have been performed in relativistic Dirac-Fock-Slater approximation with extended CI basis. The extended CI basis consists of configurations established from the previously introduced configuration interaction strength. In addition the excitation rates are obtained for energy levels of $4p^5 4d^N$ and $4d^{N-1} 4f$ configurations which couple to the ground configurations through electric-dipole transitions. Those configurations are known as strongly mixing and are the first excited configurations for the considered ions. Table 3.7 lists configurations employed in the calculations of excitation rates. Sample of electron-impact excitation rates for the W^{30+} ion at various electron temperatures are presented in Table 3.8.

Table 3.7. Configuration interaction bases used to obtain electron-impact excitation rates for levels of ground configurations

<i>Ion</i>	<i>Configurations</i>
W^{29+}	$4d^9, 4d^7 4f^2, 4p^5 4d^9 4f^1, 4d^8 5d^1, 4p^4 4d^9 4f^2, 3d^9 4d^8 4f^2, 4p^5 4d^8 4f^1 5g^1, 4p^5 4d^8 5p^1 5d^1, 4p^5 4d^8 4f^1 6g^1, 4s^1 4d^8 4f^2, 4d^7 5d^2, 4p^5 4d^8 4f^1 7g^1, 3d^8 4d^9 4f^2, 4d^7 5d^1 6d^1, 4p^5 4d^8 4f^1 5d^1, 3d^9 4d^8 4f^1 5f^1, 4s^1 4p^5 4d^{10} 4f^1, 4p^5 4d^9 5p^1, 4s^1 4d^9 5s^1, 4d^8 6d^1, 4p^5 4d^9 6p^1, 4d^8 7d^1, 4d^8 5g^1, 3d^8 4d^9 4f^1 5f^1, 4p^5 4d^8 5p^1 6d^1, 4s^1 4d^8 5s^1 5d^1, 3d^9 4p^5 4d^{10} 4f^1, 4d^7 4f^1 5p^1, 4p^5 4d^8 5d^1 6p^1, 4s^1 4d^8 4f^1 5p^1, 4p^4 4d^9 5p^2, 4d^7 5d^1 7d^1, 4d^9 4f^2, 3d^9 4d^8 4f^1 6f^1, 4s^1 4p^5 4d^9 4f^1 5g^1$
W^{30+}	$4d^8, 4d^6 4f^2, 4p^5 4d^8 4f^1, 4d^7 5d^1, 4p^4 4d^8 4f^2, 3d^9 4d^7 4f^2, 4p^5 4d^7 4f^1 5g^1, 4p^4 4d^{10}, 4p^5 4d^7 5p^1 5d^1, 4p^5 4d^8 5p^1, 4s^1 4d^8 5s^1, 4s^1 4p^5 4d^9 4f^1, 4s^1 4d^7 4f^2, 4p^5 4d^7 4f^1 6g^1, 4d^6 5d^2, 4d^7 5g^1, 3d^8 4d^8 4f^2$
W^{31+}	$4d^7, 4d^5 4f^2, 4p^5 4d^7 4f^1, 4d^6 5d^1, 4p^4 4d^9, 4p^4 4d^7 4f^2, 3d^9 4d^6 4f^2, 4p^5 4d^6 4f^1 5g^1, 4s^1 4p^5 4d^8 4f^1, 3d^9 4p^5 4d^8 4f^1, 4p^5 4d^6 5p^1 5d^1, 4d^6 5g^1, 4s^1 4d^8, 4s^1 4d^6 4f^2, 4p^5 4d^7 5p^1, 4s^1 4d^7 5s^1$
W^{32+}	$4d^6, 4p^5 4d^6 4f^1, 4d^4 4f^2, 4d^5 5d^1, 4p^4 4d^8, 4p^4 4d^6 4f^2, 4s^1 4p^5 4d^7 4f^1, 4p^5 4d^5 4f^1 5g^1, 4s^1 4d^7, 4p^5 4d^6 5p^1, 4s^1 4d^6 5s^1$
W^{33+}	$4d^5, 4p^5 4d^5 4f^1, 4d^3 4f^2, 4p^4 4d^7, 4d^4 5d^1, 4p^4 4d^5 4f^2, 4s^1 4p^5 4d^6 4f^1, 4s^1 4d^6, 3d^9 4p^5 4d^6 4f^1, 4p^5 4d^4 4f^1 5g^1, 4p^5 4d^5 5p^1, 4s^1 4d^5 5s^1$
W^{34+}	$4d^4, 4p^5 4d^4 4f^1, 4p^4 4d^6, 4d^2 4f^2, 4d^3 5d^1, 4p^4 4d^4 4f^2, 4s^1 4p^5 4d^5 4f^1, 4s^1 4d^5, 3d^9 4p^5 4d^5 4f^1, 4p^5 4d^3 4f^1 5g^1, 3d^9 4d^3 4f^2, 4p^5 4d^4 5p^1, 4s^1 4d^4 5s^1$
W^{35+}	$4d^3, 4p^5 4d^3 4f^1, 4p^4 4d^5, 4d^1 4f^2, 4p^4 4d^3 4f^2, 4s^1 4p^5 4d^4 4f^1, 4d^2 5d^1, 4s^1 4d^4, 3d^9 4p^5 4d^4 4f^1, 4p^5 4d^2 4f^1 5g^1, 3d^9 4d^2 4f^2, 3d^8 4d^3 4f^2, 4d^5, 4p^5 4d^3 5p^1, 4s^1 4d^3 5s^1$
W^{36+}	$4p^6 4d^2, 4p^4 4d^4, 4p^5 4d^2 4f^1, 4s^1 4p^5 4d^3 4f^1, 4p^4 4d^2 4f^2, 4p^6 4f^2, 3d^9 4p^5 4d^3 4f^1, 4s^1 4p^6 4d^3, 4p^6 4d^4, 3d^8 4p^6 4d^2 4f^2, 4p^5 4d^1 4f^1 5g^1, 3d^9 4p^6 4d^1 4f^2, 3d^9 4p^5 4d^3 5f^1, 4p^6 4d^1 5d^1, 4p^5 4d^2 5p^1, 4s^1 4p^6 4d^2 5s^1, 3d^9 4p^6 4d^3, 3d^8 4p^6 4d^2 4f^1 5f^1, 3d^8 4p^6 4d^4, 4p^4 4d^3 5g^1, 4s^1 4p^6 4d^2 5g^1, 4s^1 4p^5 4d^2 4f^1 5g^1, 4p^5 4d^1 5p^1 5d^1, 4s^1 4p^6 4d^1 4f^2, 4p^6 4d^1, 4p^5 4d^1 4f^1, 4p^4 4d^3$
W^{37+}	$4p^6 5d^1, 4p^6 5s^1$

Table 3.8 Electron-impact excitation rates from ground level to the first ten excited levels for the $4d^5$ configuration of W^{33+} . Electron temperatures are in eV and excitation rates are in $10^3 \text{ cm}^3\text{s}^{-1}$

i	f	1000	1500	2000	2500	3000	3500	4000	4500	5000
1	2	1.71E+0	1.23E+0	1.03E+0	8.33E-1	6.59E-1	5.07E-1	3.72E-1	2.49E-1	1.36E-1
1	3	1.85E-1	1.44E-1	1.21E-1	1.04E-1	9.40E-2	8.62E-2	7.99E-2	7.45E-2	6.97E-2
1	4	3.52E-2	2.49E-2	1.93E-2	1.58E-2	1.35E-2	1.17E-2	1.04E-2	9.35E-3	8.50E-3
1	5	7.67E-2	6.10E-2	5.20E-2	4.61E-2	4.19E-2	3.87E-2	3.61E-2	3.39E-2	3.22E-2
1	6	1.04E-1	8.19E-2	6.89E-2	5.99E-2	5.42E-2	4.97E-2	4.62E-2	4.32E-2	4.05E-2
1	7	2.59E-1	2.01E-1	1.70E-1	1.46E-1	1.29E-1	1.16E-1	1.05E-1	9.55E-2	8.68E-2
1	8	3.92E-2	3.06E-2	2.56E-2	2.20E-2	1.98E-2	1.82E-2	1.68E-2	1.57E-2	1.46E-2
1	9	2.85E-2	2.12E-2	1.72E-2	1.47E-2	1.29E-2	1.16E-2	1.06E-2	9.80E-3	9.13E-3
1	10	5.35E-2	4.22E-2	3.56E-2	3.09E-2	2.80E-2	2.57E-2	2.39E-2	2.24E-2	2.10E-2

3.5 Theoretical studies of highly charged tungsten atoms having open f -shells taking into account relativistic and correlation effects

Tungsten (W) is planned to be used as a plasma wall material in the future tokamaks, such as ITER and DEMO. Therefore, for the detail analysis of the thermonuclear plasma spectra, impurities in it, knowledge of the large number of its free-ion spectroscopic parameters is needed. For this purpose it is important to perform a comprehensive theoretical modelling of the atomic structure of various tungsten ions. Such ions, having simple electronic configurations of open shells (a few times and highly ionized atoms), are studied both experimentally and theoretically fairly completely, but this is not the case for ions, having open f -shell. It has been extremely difficult or even impossible to perform such calculations for the tungsten ions with open f -shell due to the large number of atomic states. Indeed, the accurate experimental or theoretical spectroscopic data for such ions are sparse [18, 34].

In this work we present the results of the first large-scale multiconfiguration calculations of the energetically lowest W^{24+} configurations, demonstrating the feasibility of such studies.

For the calculations, we used different ab initio methods, namely the multiconfiguration Hartree-Fock (MCHF) and multiconfiguration Dirac-Fock (MCDF) approaches taking into account relativistic and QED corrections [35].

The relativistic configuration interaction (RCI) method was used to include the transverse Breit interaction at the low-frequency limit (describing the transversely polarized photon contributions to the electron-electron interactions in Coulomb gauge), and the QED corrections (including self-energy and vacuum polarization) [36, 37]. MCDF calculations were performed with the GRASP2K relativistic atomic structure package [36, 38] in which for calculations of spin-angular parts of matrix elements the second quantization method in coupled tensorial form and quasispin technique [35] were adopted. This allowed to achieve the breakthrough in the field, to essentially increase the efficacy and the speed of the calculations, opening the possibilities to consider extremely complex electronic configurations.

In case of the MCDF expansions of the even and odd ASFs for the energy spectrum calculations we used a multireference (MR) set of CSFs based on the $[Kr]4d^{10}4f^4$ and $[Kr]4d^{10}4f^35p$ even as well as $[Kr]4d^{10}4f^35s$ and $[Kr]4d^94f^5$ odd configurations. The even and odd ASFs were calculated independently. The state functions of these four configurations form the basis for the zero-order wave function (MR set). The energy functional on which the orbitals were optimized was defined

according to an extended optimal level (EOL) scheme [36], where a linear combination of atomic states, corresponding to the lowest two $J = 0, \dots, 8$ states, were used (the same scheme was used for the even and odd states). An admixed CSFs were obtained from single substitutions from all open-shell orbitals to an increasing active set (AS) of orbitals. The AS is labelled by an integer n and includes s , p and d orbitals with principal quantum numbers up to n and f orbitals up to $n - 1$. For example, the active set $AS_n = 6$ contains s , p and d orbitals with principal quantum number up to 6 and f orbitals up to $n = 5$. The active sets were successively extended to $n = 7$. Only new orbitals were optimized in all steps.

Figure 3.4 displays the computed energies of 977 lowest levels of W^{24+} belonging to $[Kr]4d^{10}4f^4$ (107 levels), $[Kr]4d^{10}4f^35s$ (82 levels), $[Kr]4d^{10}4f^35p$ (242 levels) and $[Kr]4d^94f^5$ (incomplete, 546 levels) configurations. The results presented are obtained in the both non-relativistic and relativistic approaches. In the non-relativistic case the largest scale MCHF and CI approximation as well as the ATSP-package [39] were used. Figure 3.4 indicates that the both (non-relativistic and relativistic) approximations lead to the similar general picture of the energy spectra of the $[Kr]4d^{10}4f^4$ and $[Kr]4d^{10}4f^35s$ configurations. However, the detailed analysis of the numerical data reveals the essential differences in the structure of their energy spectra. Thus, for the studies of the energy spectra, fine structure, the electron transition probabilities, the lifetimes, etc. of such ions, one must use already at the very beginning the relativistic approach.

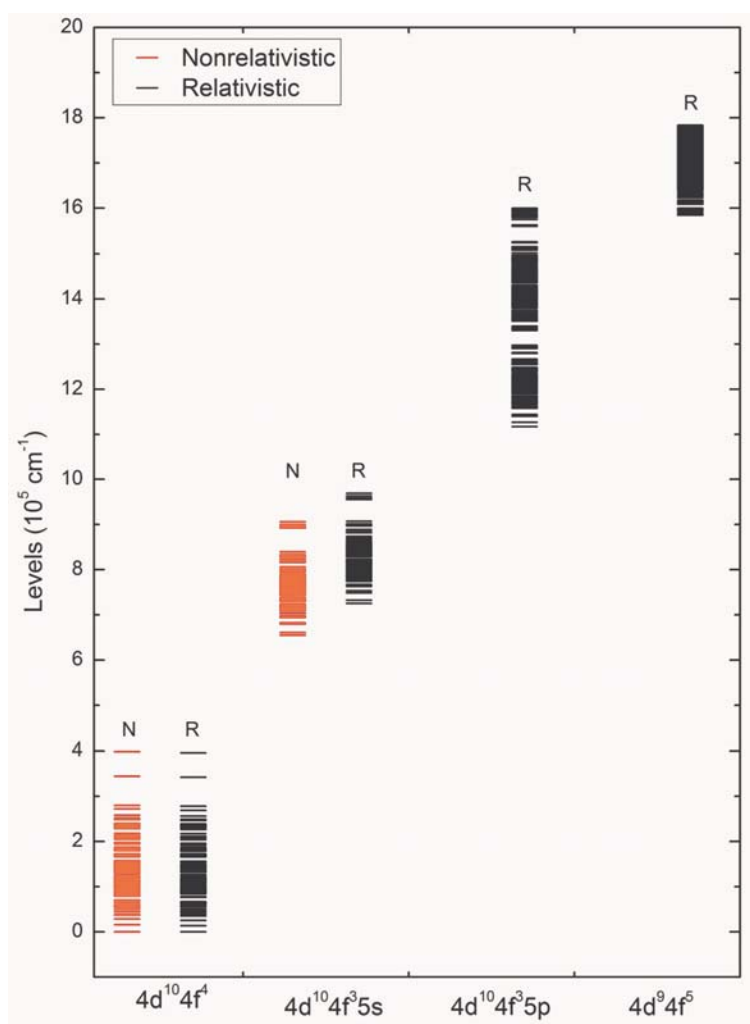


Figure 3.4

Configurations of W^{24+} in different approaches (MCHF+BP in red (N) and MCDF+B+QED in black (R)) with AS_7 atomic state function expansion (single excitation)

Table 3.9. A square of the largest coefficient averaged over the states (P_s) in the MCHF+BP(LS -coupling) and in the MCDF+B+QED (jj -coupling) approaches

<i>Configuration</i>	P_s	
	<i>LS-coupling</i>	<i>jj-coupling</i>
[Kr] $4d^{10}4f^4$	0.53	0.56
[Kr] $4d^{10}4f^35s$	0.54	0.52
[Kr] $4d^{10}4f^35p$		0.46

The main peculiarity of the W^{24+} ion consists in the uniqueness of its ground configuration, containing the only open f -shell, namely, $4f^4$. As we see from the calculations, the lowest excited state of this ion is $4f^35s$. Normally electric dipole electronic transitions are allowed between the first excited and ground configuration. As the rule they are the strongest. In our case, however, such transitions are of octopole character. Quite unique are also the electronic transitions from the higher excited configuration to the ground configuration (quadrupole for $4f^35p - 4f^4$) or between the excited configurations (e.g., two-electron transitions).

The evaluation of the suitability of the LS - and jj -couplings for the classification of energy spectra is performed using the methodic described in [40, 41]. Table 3.9 presents the square of the largest coefficient averaged over the states (P_s) in the MCHF+BP and in the MCDF+B+QED approaches. In the first case the energy levels are characterized by the quantum numbers of the LS -coupling whereas in the second one – by jj -coupling. The larger P_s value, the better is the coupling scheme. In ideal case P_s may reach 1. We were unable to find P_s value for [Kr] $4d^{10}4f^35p$. It follows from the Table 3.9 that both coupling schemes are almost equally unsuitable and for the atomic states of these configurations it is important to use the intermediate coupling approximation. However, configuration mixing between investigated non-relativistic configurations is relatively weak. Therefore, in case of the electric dipole (E1) electronic transitions, except of the exact selection rules

$$\Delta J = 0, \pm 1 (J = J' \neq 0),$$

$$\Delta l = \pm 1,$$

the selection rules for the other quantum numbers are approximate.

The electric dipole (E1) transitions have the largest probabilities. That is why one of the goals of the present work is to study their peculiarities in W^{24+} . We can see from Figure 3.4 that the E1 transitions are allowed only between the levels of the excited configurations [Kr] $4d^{10}4f^35p$ and [Kr] $4d^{10}4f^35s$. For the calculations of the E1 transitions between initial even [Kr] $4d^{10}4f^35p$ and final odd [Kr] $4d^{10}4f^35s$ configurations we used single reference (SR) set. The even and odd ASFs were calculated independently. The E1 transition data (wavelengths, transition probabilities and line strengths) were calculated using the biorthogonal orbital transformations [42].

Table 3.10 presents the most probable transition probabilities for spontaneous emission and line strengths of E1 transitions in both Babushkin and Coulomb gauges. Figure 3.5 presents the distribution of the transition probabilities for spontaneous emission A in s^{-1} of electric dipole transitions among the levels of [Kr] $4d^{10}4f^35p$ and [Kr] $4d^{10}4f^35s$ configurations in the Babushkin gauge with respect to their wavelengths. As seen from it, there are some transitions with probabilities significantly higher than others. The transition probabilities considered are in the time interval of $10^2 s^{-1} - 10^{10} s^{-1}$. The largest A are localized in two wavelengths, intervals. The most probable transitions are localized in the $170 \text{ \AA} - 198 \text{ \AA}$ domain. Transition probabilities, localized in the second domain ($285 \text{ \AA} - 310 \text{ \AA}$), are generally lower. These domains are of interest for thermonuclear plasma diagnostics.

Table 3.10. Calculated wavelengths (in 10^2 \AA), transition probabilities A (in 10^{10} s^{-1}) and line strengths S for the most probable (exceeding $6 \times 10^{10} \text{ s}^{-1}$) electric dipole transitions among the levels of $[\text{Kr}]4d^{10}4f^35p$ and $[\text{Kr}]4d^{10}4f^35s$ configurations

<i>Upper*</i>				<i>Lower</i>			$\lambda (10^2 \text{ \AA})$	$A \text{ (in } 10^{10} \text{ s}^{-1}\text{)}$		S	
J	P	ω	<i>Configuration</i>	J	P	ω		A_C	A_B	S_C	S_B
0	+	9	$4f_{-}^3(J=3/2)5s$	1	-	1	1.872645	6.722	6.942	0.218	0.225
0	+	10	$4f_{-}^2(J=2)4f(J_{12}=3/2)5s$	1	-	2	1.885351	6.135	6.300	0.203	0.208
1	+	29	$4f^3(J=5/2)5s$	2	-	12	1.816095	6.849	7.018	0.607	0.622
1	+	30	$4f_{-}4f^2(J=0)5s$	2	-	13	1.790459	7.660	7.874	0.651	0.669
2	+	50	$4f_{-}^2(J=0)4f(J_{12}=7/2)5s$	3	-	12	1.814150	6.525	6.723	0.962	0.991
2	+	52	$4f^3(J=7/2)5s$	3	-	13	1.785163	6.296	6.493	0.884	0.912
4	+	59	$4f_{-}4f^2(J=0)5s$	3	-	14	1.823401	6.468	6.621	1.742	1.783
3	+	26	$4f_{-}^3(J=9/2)5s$	4	-	1	1.844713	6.896	7.155	1.496	1.552
5	+	48	$4f^3(J_{12}=7/2)5s$	4	-	14	1.830873	7.085	7.259	2.361	2.419
6	+	22	$4f_{-}^3(J_{12}=9/2)5s$	5	-	1	1.861758	6.084	6.233	2.519	2.581
6	+	39	$4f_{-}4f^2(J=2)(J_{12}=9/2)5s$	5	-	12	1.836273	6.780	6.946	2.693	2.760
7	+	14	$4f_{-}^2(J=4)4f(J_{12}=11/2)5s$	6	-	1	1.865237	6.235	6.358	2.996	3.054
8	+	12	$4f_{-}4f^2(J=6)(J_{12}=13/2)5s$	7	-	1	1.867704	6.589	6.698	3.602	3.662
9	+	4	$4f_{-}4f^2(J=6)(J_{12}=15/2)5s$	8	-	1	1.867316	7.108	7.202	4.340	4.397
9	+	5	$4f_{-}^2(J=4)4f(J_{12}=15/2)5s$	8	-	2	1.848967	7.075	7.194	4.194	4.264
10	+	3	$4f_{-}4f^2(J=6)(J_{12}=17/2)5s$	9	-	1	1.838271	7.329	7.458	4.718	4.802

* The notation ω means position of level among the levels with the same total angular momentum quantum number J and P stands for the total angular momentum quantum number J and parity P (classification of the levels in jj-coupling)

Table 3.11. Calculated lifetimes τ (in 10^{-11} s) of the 10 lowest excited levels belonging to the configuration $[\text{Kr}]4d^{10}4f^35p$

<i>Levels**</i>	τ (10^{-11} s)				
	<i>Configuration and coupling scheme</i>	<i>J</i>	<i>P</i>	ω	τ_c
$4d^4_+ 4d^6_- 4f^3_-(J = 9/2)5p_-$	5	+	15	5.843	5.851
$4d^4_+ 4d^6_- 4f^3_-(J = 9/2)5p_-$	4	+	20	5.634	5.533
$4d^4_+ 4d^6_- 4f^2_-(J = 4)4f(J_{12} = 11/2)5p_-$	6	+	14	5.755	5.727
$4d^4_+ 4d^6_- 4f^2_-(J = 4)4f(J_{12} = 11/2)5p_-$	5	+	16	5.698	5.582
$4d^4_+ 4d^6_- 4f^3_-(J = 3/2)5p_-$	2	+	18	5.788	5.756
$4d^4_+ 4d^6_- 4f_- 4f^2_-(J = 6)(J = 13/2)5p_-$	7	+	8	5.730	5.679
$4d^4_+ 4d^6_- 4f^3_-(J = 9/2)5p_-$	1	+	8	5.747	5.670
$4d^4_+ 4d^6_- 4f_- 4f^2_-(J = 6)(J_{12} = 13/2)5p_-$	6	+	15	5.654	5.512
$4d^4_+ 4d^6_- 4f^2_-(J = 4)4f(J_{12} = 9/2)5p_-$	5	+	17	5.761	5.718
$4d^4_+ 4d^6_- 4f^2_-(J = 4)4f(J_{12} = 9/2)5p_-$	4	+	21	5.725	5.631

** The notations w mean positions of a level among levels with the same total angular momentum quantum number J and $J P$ stands for the total angular momentum quantum number J and parity P (classification of the levels in jj -coupling)

In Table 3.11 the lifetimes τ of the 10 lowest excited levels belonging to the configuration $[\text{Kr}]4d^{10}4f^35p$ are presented in both Babushkin and Coulomb gauges [35, 43]. The good agreement between the two gauges is seen. The lifetimes of the rest (higher) energy levels τ are similar to those presented in Table 3.11 and are of the order of 10^{-11} s.

Final remarks. Because of the absence of the relevant experimental results it is impossible to present the accurate error estimates for each entry. However indirect hints, like the high accuracy of such calculations for simpler configurations or the convergency of the accounting for correlations effects or comparison of non-relativistic (but accounting for relativistic corrections) and relativistic calculations or calculation of complex systems like Cm^{4+} [44], Am^{3+} [44], eka-thorium [45] and Ra [46] in the same approach with the same programs, speaks for fairly high precision of the approach and results obtained.

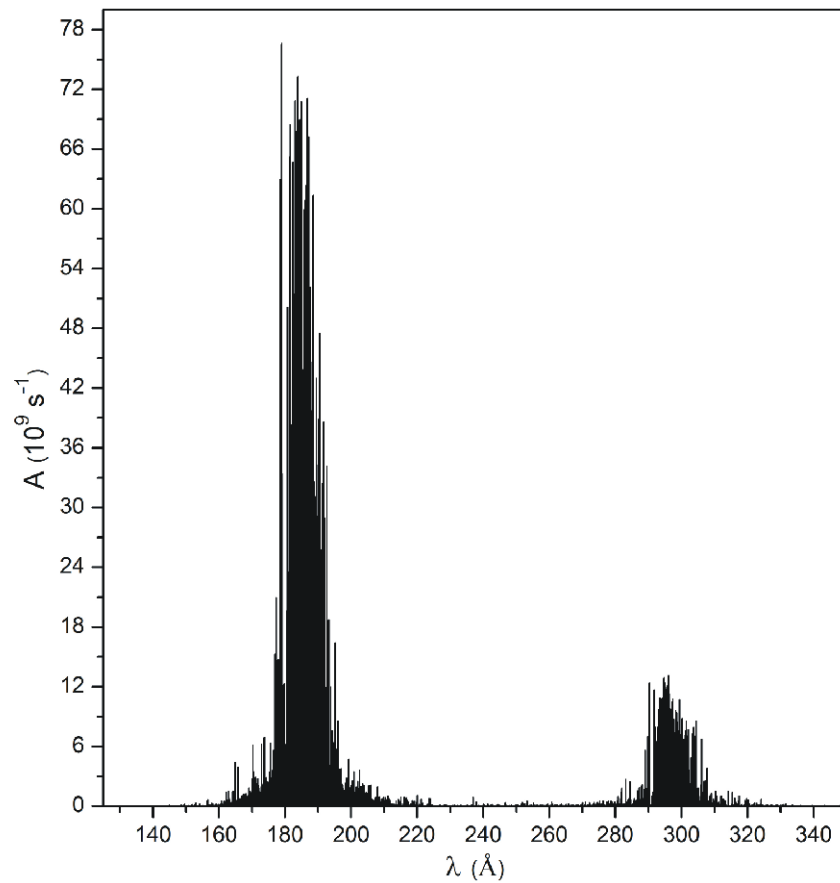


Figure 3.5
Theoretical E1 transition probabilities of W^{24+} in the MCDF+B+QED approach with AS_7 atomic state function expansion (single excitation) in Babushkin (length) gauge

4 MOBILITY PROGRAM 2010

During 2010 the following visits were implemented under the mobility plan:

4.7 Fusion safety issues

It was planned to participate in one mission to IPP-Griefswald, Germany. This mission was implemented by visit of Tadas Kaliatka, Mantas Povilaitis, Gintautas Dundulis, Renatas Karalevičius, Egidijus Urbonavičius, and Robertas Alzbutas to IPP-Griefswald on November 28 – December 4, 2010.

A visit to W7-X facility was performed to see the current status of the facility. The as-built facility was checked against the available drawings in order to clarify and update RELAP5, ASTEC and COCOSYS models used for analysis of W7-X facility. In particular, the almost finished assembly work of the cooling system in the second basement has been shown together with their control systems. Plasma vessel of W7-X is also important and has significant impact in the modelling of cooling system, so modules of plasma vessel has been shown and described. During this visit discussions were held with specialists of W7-X facility. Needs for additional design data and possible model improvements were discussed and agreed.

Results of analysis of thermal-hydraulic processes in W7-X facility was presented at the meeting. Double-ended break of DN40 pipe in the targets, water hammer effect in the case of fast closure of automatic valves, analysis of small leakage in upper target feeding pipe, model of plasma vessel and others. At this meeting the teleconference with the colleagues from IPP-Garching was organized. They made comments and discussed on the performed analysis and received results. During this teleconference future work was discussed as well.

The technical meeting with IPP experts (F. Schauer, A. Tereshchenko, J. Fullinger) was arranged. G. Dundulis presented developed 3D models of the ports AEU30 and AEQ20. He explained the problems which arose in preparation of the models. The finite element models of these ports were tested and a preliminary limit analysis of these ports weld between the plasma vessel and the ports can be performed. The geometrical model of the port AEK20 was developed. The finite element model of this port will be developed during several weeks.

The data on material properties and results of the performed analysis by IPP specialists of the components of facility W7-X were selected from base data of IPP. This material will be used in future analysis of components of facility W7-X.

Further co-operation activities possible in the year 2011 were discussed with Mr. Naujoks. It was agreed that LEI will improve models of the W7-X facility developed for the LOCA analysis using new design data obtained from the IPP. IPP has provided additional data for the model during the visit.

A number of presentations on the experience of LEI regarding performance of probabilistic safety analysis and analysis of systems and components reliability were provided to IPP. It was agreed to investigate possibilities regarding initiation of mobility program actions regarding long-term stay of representative from LEI at IPP in 2011 to perform the probabilistic safety analysis. As well the PostDoc possibilities at IPP will be investigated.

Together with Mr. Naujoks (IPP) the co-operation in 2010 and plans for 2011 and beyond were discussed. Detailed discussions were held on the topics of probabilistic system analysis, models

of W7-X cooling circuit and plasma vessel for RELAP5, ASTEC and COCOSYS codes. As well the future plans for structural and fracture analyses were discussed. The achievements in 2010 and agreed co-operation activities in 2011 and beyond are documented in the minutes of the meeting. The videoconference with IPP-Garching was held during the stay at IPP-Greifswald to discuss received results and possible new actions for W7-X.

Meetings under EFDA:

Rolandas Urbonas participated in the EFDA Public Information Group Annual Meeting, which was held in Riso, Roskilde (Denmark) on May 5-7, 2010. This meeting was not originally included in the mobility plan, but added after the 4th SC meeting.

As well, in the updated mobility plan there was included participation in the Remote Participation Users Group Meeting, but this meeting was not announced later on in the year and invitation to this meeting was not received.

5 PUBLIC INFORMATION

The information related with FUSION energy perspectives, last achievements in ITER development and other Fusion research fields is continuously distributed among universities, R&D institutions, schools:

- March 17, 2010. "Career days 2010" at Kaunas Technology University, Kaunas Lithuania. Distribution of information and discussions on FUSION to students.
- April 29, 2010. Open days of Lithuanian Energy Institute. Distribution of information and discussions on FUSION to students.
- May 27-28, 2010. 7th Conference of young scientists on energy issues CYSENI 2010 (www.cyseni.com). Conference is with regional (Belarus, Estonia, Germany, Italy, Latvia, Lithuania, Norway) attention. In the conference "Fusion energy" topic was included (1 of 11). Two papers were presented at the conference.
- September 24, 2010. FP7 project "Researchers night 2010". Distribution of information and discussions on FUSION to students.
- Through our partner Vytautas Magnus University, which is located in Kaunas, Lithuania, the information is spread to schools when university looks for students to physics studies.

6 PUBLICATIONS

- 6.1. P. Bogdanovich, V. Jonauskas, R. Karpuškienė, O. Rancova. Theoretical investigation of x-ray radiation of 4-4 transitions in highly charged tungsten ions, *Nucl. Instr. and Meth. A*, 619, 15-17 (2010).
- 6.2. V. Jonauskas, G. Gaigalas, S. Kučas. Theoretical study of $4p^5 4d^{N+1} + 4p^6 4d^{N-1} 4f - 4p^6 4d^N$ transitions in tungsten ions, 10th European Conference on Atoms, Molecules and Photons, Abstracts, Salamanka, Spain, 2010, p. P-661.
- 6.3. V. Jonauskas, R. Kisielius, A. Kynienė, S. Kučas, P.H. Norrington. Magnetic dipole transitions in $4d^N$ configurations of tungsten ions. *Phys. Rev. A*, 81, 012506 (2010).
- 6.4. T. Kačegavičius. The analysis of 40 mm diameter pipe rupture in fusion facility W7-X with ASTEC code // 7th annual conference of young scientists on energy issues CYSENI 2010, Kaunas, Lithuania, May 27-28, 2010. Kaunas: LEI, 2010. ISSN 1822-7554, p. 515-525.
- 6.5. T. Kačegavičius. Avarijų su šilumnešio praradimu skirtinguose termobranduolinės sintezės įrenginio W7-X elementuose analizė // Šilumos energetika ir technologijos-2010: konferencijos pranešimų medžiaga, Kauno technologijos universitetas, 2010 vasario 4,5. Kaunas: Technologija, 2010. ISBN 978-9955-25-881-0, p. 163-168.
- 6.6. T. Kaliatka, A. Kaliatka, T. Kačegavičius, D. Naujoks. Analysis of the processes in the target cooling system of the W7-X fusion experiment // *Kerntechnik*. ISSN 0932-3902. 2010. Vol. 75, No. 5, p. 255-262.
- 6.7. A. Kaliatka, M. Povilaitis, E. Urbonavičius, T. Kaliatka. Analysis of the consequences of targets feeding pipe rupture in Wendelstein 7-X experimental nuclear fusion device // 8th international topical meeting on nuclear thermal-hydraulics, operation and safety (NUTHOS-8), Shanghai Jiao Tong University, China, October 10-14, 2010. Shanghai, 2010, p. 1-12.
- 6.8. R. Karpuškienė, O. Rancova, P. Bodanovich. An *ab initio* study of the spectral properties of W II, *J. Phys. B: At. Mol. Opt. Phys*, 43, 085002(6pp) (2010).
- 6.9. R. Kisielius, V. Jonauskas, Ç. Masys. Collision data calculation for highly-charged open $n=4$ shell tungsten ions using analogues of relativistic integrals. 7th International Conference on Atomic and Molecular Data and Their Applications, Book of Abstracts, Vilnius, Lithuania, 2010, p. 104.

7 IMPLEMENTATION OF QA SYSTEM

The quality assurance system according to standard LST EN ISO 9001:1995 requirements in Lithuanian Energy Institute has been developed in 1999.

In 2001 the updating of quality assurance system of institute on the basis of requirements of standard LST EN ISO 9001:2001 was initiated. According to these requirements the quality package of quality assurance documents in LEI was developed.

On February 17, 2004 the quality system of institute is certified by the Lithuanian Standards Board under the Ministry of Environment of the Republic of Lithuania and the certificate of quality management system conformity to standard LST EN ISO 9001:2001 is received. On February 15, 2007 duration of certificate was extended for next three years.

On February 15, 2010 the quality system of institute was certified by the Lithuanian Standards Board under the Ministry of Environment of the Republic of Lithuania and the certificate of quality management system conformity to standard LST EN ISO 9001:2008 was received.

On 15 February 2010 the environmental management system of institute was certified by the Lithuanian Standards Board under the Ministry of Environment of the Republic of Lithuania and the certificate of environmental management system conformity to standard LST EN ISO 14001:2005 was received.

The safety analysis of FUSION facilities is included in the procedure "PA/17-02, Control of nuclear installation safety research process", which is prepared in accordance with LST EN ISO 9001:2001 standards and operating together with other LEI quality management system procedures.

8 REFERENCES

1. D. Naujoks, Initial and Boundary Conditions, 1-NBF-T0008.0, Max-Planck-Institut für Plasma Physik, 2006.
2. E. Urbonavičius, D. Naujoks, Minutes of Meeting between IPP and LEI, Max-Planck-Institut für Plasmaphysik, LEI-IPP Co-operation, 1-NBF-C0010.0, IPP Greifswald, September 3–14, 2007.
3. C.D. Fletcher, *et al.*, 1992. RELAP5/MOD3 code manual user's guidelines. Idaho National Engineering Lab., NUREG/CR-5535.
4. W. Klein-Hessling, *et al.*, COCOSYS V1.2 Program Reference Manual, GRS-P-3/2, Gesellschaft für anlagen- und Reaktorsicherheit (GRS) mbH, 2000.
5. <http://www.solidworks.com>
6. BRIGADE/Plus Version 1.3., 2003. User's Manual, Scanscot Technology AB.
7. Abaqus/Standard, 2003. User's Manual Volume IV, Version 6.4.
8. P. Bogdanovich and O. Rancova, Phys. Rev. A 74, 052501 (2006).
9. P. Bogdanovich and O. Rancova, Phys. Rev. A 76, 012507 (2007).
10. P. Bogdanovich and O. Rancova, Lithuanian J. Phys. 42, 257 (2002); P. Bogdanovich, V. Jonauskas and O. Rancova, Nucl. Instr. and Meth. B 235, 145 (2005).
11. P. Bogdanovich and O. Rancova, Phys. Scr. 78, 045301 (2008).
12. A. E. Kramida, T. Shirai, At. Data Nucl. Data Tables 95, 305 (2009).
13. P. Bogdanovich, V. Jonauskas, R. Karpuškienė and O. Rancova, Nucl. Instr. and Meth. A 619, 15 (2010).
14. P. Bogdanovich and R. Karpuškienė, Lithuanian J. Phys. 39, 193 (1999).
15. P. Bogdanovich, R. Karpuškienė and A. Momkauskaitė, Comput. Phys. Commun. 143, 174 (2002) and P. Bogdanovich and A. Momkauskaitė, Comput. Phys. Commun. 157, 217 (2004).
16. S.D. Loch *et al.* Phys. Rev. A 72, 052716 (2005).
17. R.D. Cowan. The Theory of Atomic Structure and Spectra (Barceley, CA: University of California Press) 1981.
18. T. Pütterich *et al.* Plasma Phys. Control. Fusion, 50, 085016 (2008).
19. P. Summers. The ADAS-Manual (<http://www.adas.ac.uk/manual.php>).
20. J.L. Campbell and T.Papp. At. Data Nucl. Data Tables, 77, 1 (2001).
21. S.T. Perkins *et al.* Tables and Graphs of Atomic Subshell Relaxation Data derived from the LLNL Evaluated Atomic Data Library, Lawrence Livermore National Laboratory report UCRL-504000, Vol. 30 (1991).
22. R. Radtke *et al.* Phys. Rev. A 64 012720 (2001).
23. T. Putterich *et al.* Plasma Phys. Control. Fusion 50 085016 (2008).

24. C.S. Harte *et al.* *J. Phys. B: At. Mol. Opt. Phys.* 43 0953 (2010).
25. V. Jonauskas *et al.* *J. Phys. B: At. Mol. Opt. Phys.* 40 2179 (2007).
26. S. Kučas *et al.* *J. Phys. B: At. Mol. Opt. Phys.* 42 205001 (2009).
27. S. Kučas *et al.* *Lith. J. of Phys.* 47 249 (2007).
28. V. Jonauskas *et al.* *Phys. Rev. A* 81, 012506 (2010).
29. S. Kučas *et al.* *Lith. J. Phys.* 47 249 (2007).
30. Yu. Ralchenko *et al.* *J. Phys. B* 40 3861 (2007).
31. S. Kučas *et al.* *Phys. Scr.* 55 667 (1997).
32. R. Karazija. *Introduction to the Theory of X-ray and Electron Spectra of Free Atoms* (London: Plenum) 1996.
33. T. Pütterich *et al.* *J. Phys. B* 38 3071 (2005).
34. A. E. Kramida, T. Shirai. *Atom. Data Nucl. Data Table*, 95, 305 (2009).
35. Z.R. Rudzikas. *Theoretical Atomic Spectroscopy*. (Cambridge university press, second edition 2007.)
36. P. Jönsson, X. He, C. Froese Fischer, I.P. Grant. *Comput. Phys. Commun.*, 177, 597 (2007).
37. B. J. McKenzie, I. P. Grant, P. H. Norrington. *Comput. Phys. Commun.*, 21, 233 (1980).
38. C. Froese Fischer, G. Gaigalas, Y. Ralchenko. *Comput. Phys. Commun.*, 175, 738 (2006).
39. C. Froese Fischer, G. Tachiev, G. Gaigalas, M.R. Godefroid. *Comput. Phys. Commun.*, 176, 559 (2007).
40. Z. B. Rudzikas, J. V. Čiplies. *Physica Scripta*, T26, 21 (1989).
41. T. Žalandauskas, G. Gaigalas, Z. Rudzikas. *Nuclear Instr. and Meth. in Physics Res. B*, 235, 149 (2005).
42. J. Olsen, M. R. Godefroid, P. Jönsson, P. A. Malmqvist, C. Froese Fischer. *Phys. Rev. E*, 52, 4499 (1995).
43. K.G. Dyall, I.P. Grant, C.T. Johnson, F.A. Parpia, E.P. Plummer. *Comput. Phys. Commun.*, 55:425, 1989.
44. G. Gaigalas, E. Gaidamauskas, Z. Rudzikas, N. Magnani, R. Caciuffo. *Phys. Rev. A*, 79:022511, 2009.
45. G. Gaigalas, E. Gaidamauskas, Z. Rudzikas, N. Magnani, R. Caciuffo. *Phys. Rev. A*, 81:022508, 2010.
46. J. Bieroń, G. Gaigalas, E. Gaidamauskas and S. Fritzsche, P. Indelicato, P. Jönsson. *Phys. Rev. A*, 80:012513, 2009.



ISSN 2029-1612



9 772029 161000